Doctoral theses at NTNU, 2021:269

Halima Zahra Bukhari

Modeling and Control of the Czochralski Crystal Growth Process

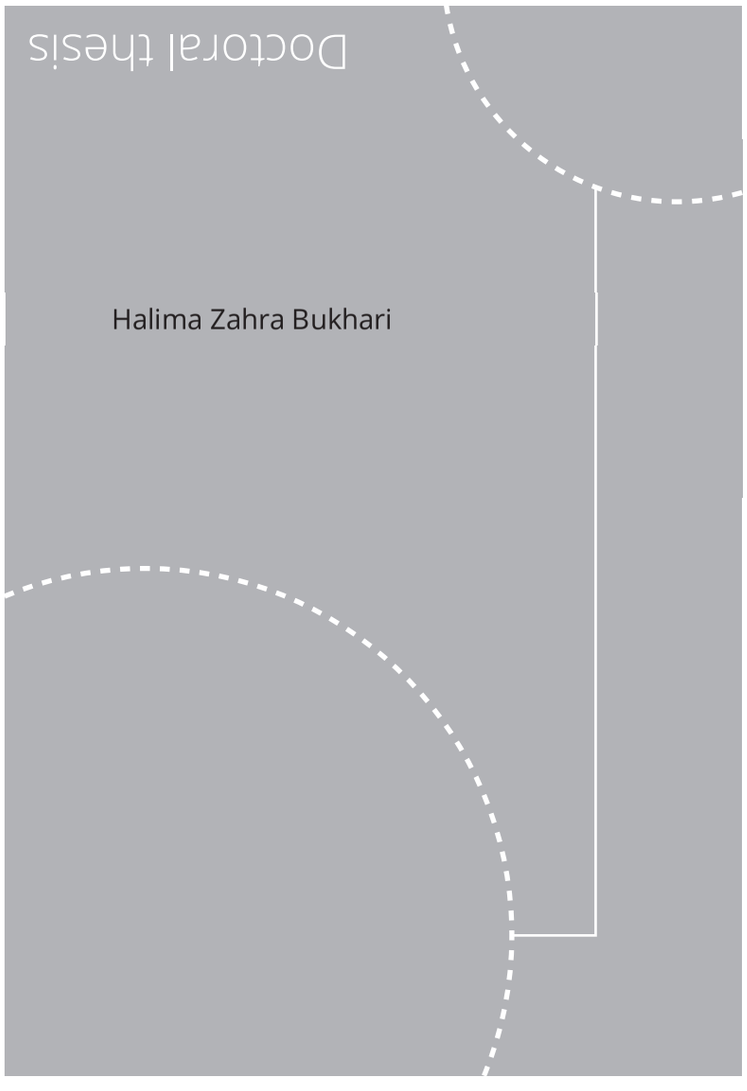

ISBN 978-82-326-6012-4 (printed ver.)
ISBN 978-82-326-5765-0 (electronic ver.)
ISSN 1503-8181 (printed ver.)
ISSN 2703-8084 (electronic ver.)

NTNU
Norwegian University of
Science and Technology

NTNU
Norwegian University of
Science and Technology
Thesis for the degree of
Philosophiae Doctor
Faculty of Information Technology
and Electrical Engineering
Department of Engineering Cybernetics

Doctoral theses at NTNU, 2021:269

NTNU

NTNU
Norwegian University of
Science and Technology

Halima Zahra Bukhari

Modeling and Control of the Czochralski Crystal Growth Process

Thesis for the degree of Philosophiae Doctor

Trondheim, August 2021

Norwegian University of Science and Technology
Faculty of Information Technology
and Electrical Engineering
Department of Engineering Cybernetics

NTNU
Norwegian University of
Science and Technology

NTNU
Norwegian University of Science and Technology

Thesis for the degree of Philosophiae Doctor

Faculty of Information Technology
and Electrical Engineering
Department of Engineering Cybernetics

ISBN 978-82-326-6012-4 (printed ver.)
ISBN 978-82-326-5765-0 (electronic ver.)
ISSN 1503-8181 (printed ver.)
ISSN 2703-8084 (electronic ver.)

ITK-report: 2021-5-W

Doctoral theses at NTNU, 2021:269

Printed by Skipnes Kommunikasjon AS

Summary

This thesis provides the basis for improved control of the Czochralski (Cz) process – a process used on a commercial scale to produce monocrystalline silicon (Si) ingots. This is done by developing a model for the crystal radius measurement that is, in turn, used in the process control. This model enables the design of a modified control structure that accounts for the physics of the process and removes the main limitation in the achievable performance for the crystal radius control while still being simple for the operators to understand. *(a.)* At present, the Czochralski crystal pulling process is an industrialized process that is not sufficiently automated. This process involves complex heat and mass transfers, thereby leading to both time- and spatially- varying operating conditions. Therefore, the majority of the plant operations rely on intervention by skillful operators, running these operations rather crudely on empirical knowledge of the process.

(b.) There is no *in-situ* measurement of the controlled variable, i.e., the diameter of the crystal ingot produced by the Cz process. Instead, the control of this process depends on some estimated measurement of the crystal ingot diameter. Furthermore, the measurement related to the melt temperature is also indirect. This indirect measurement, not being accurate enough to the actual temperature, hinders the control capability by delaying the appropriate temperature feedback for timely corrective action.

While the aim is to improve the control of the Cz process by skilled operators, thereby making the operation less dependent on the skills of the individual operators, there is still a need to make the process control both acceptable and understandable for the operators. While very detailed models exist, typically using some finite element model of the plant, the lack of online measurements makes it hard to update such models during the production of individual ingots. These factors

limit the complexity of a realistic control approach. While it is desirable to make effective use of the process knowledge in the controller design, the model(s) used for controller design should be simpler yet robust rather than very detailed.

In light of the above, the model-based control regime adds the knowledge of plant dynamics to the overall control system that was otherwise tuned through empirical knowledge only.

A detailed investigation into the mechanism of an anomaly exhibited by the measurement of the crystal diameter is taken up at the first stage. As a common practice in the Cz industry, this measurement relies on the image of the growing ingot obtained via a CCD camera. In a dynamic simulation, the measurement signal manifests its anomalous trend by moving initially in a direction opposite to that of the actual response of the crystal diameter. The measurement anomaly is crucial because it poses a limiting factor in the design of the feedback control system. Therefore, a 3D ray-tracing scheme was developed to determine the dynamic response of the camera measurement, also commonly referred to as the *bright-ring radius* signal. The dynamic analysis of the measured signal serves as a guideline for designing effective radius control, undertaken at the next stage.

Before proceeding with the control design, the inverse dynamic characteristics were first determined/quantified by linearizing the Cz growth model. It is noteworthy that the output of the Cz growth model is the camera image, modeled by the 3D ray-tracing simulation. Furthermore, in the context of *linear control theory*, any linear system with the inverse response in measurements is represented by a state-space model with right-half-plane zero(s).

Systems with right-half-plane zeros also fall into the category of *non-minimum phase systems*. These systems suffer from fundamental bandwidth limitations.

To mitigate this undesired inverse response, this Ph.D. study proposes a combination of a parallel compensator and a feedback controller. The actual diameter signal is void of this inverse behaviour as it is merely an artifact caused by the system measurement technique. Therefore, the use of parallel compensation is a feasible approach for eliminating the inverse characteristics without altering the system dynamics, but enabling a faster diameter control. This technique for *removing* the non-minimum phase characteristic enables faster diameter control without pushing against the stability limitations. The designed compensator and controller are tested and validated in the nonlinear environment under the influence of temperature variations, which act as disturbances at the crystallization/growth interface.

This Ph.D. project is a part of the ASICO project (*A*dvanced *SI*ngle crystal *CO*ntrol growth for high-end photovoltaics) involving Norsun, Sintef, NTNU and TU Dres-

den, Germany. The ASICO project (‘project No. 256806/O20’) is a BIA project with funding from the Research Council of Norway.

Contents

List of Tables

List of Figures

Acknowledgements

First and foremost, my whole self is eternally grateful to all the blessings of Allah, the Almighty, especially bestowing me with the knowledge and strength to complete this doctoral thesis.

I express my deep-felt gratitude to the Research Council of Norway and Norsun Corp, the bulk crystal growth facility at Årdal, for funding this project.

Among all the persons who have been the prime influencers during this Ph.D. course, my supervisor Dr. Morten Hovd's role is the foremost. I am profoundly thankful to him for his kind support, keen guidance, and sheer diligence that led this project towards successful completion. I sincerely appreciate the strong support extended to me by my co-supervisor, Dr. Jan Winkler, affiliated with Dresden University, Germany. Together, the technical assistance by both professors at all phases of the project has contributed significantly to this work.

I am highly indebted to my parents Mr. and Mrs. Bukhari and my sister Javeria for their incredible love and support to fight all the odds.

Last but not least, comes my immediate family of three adorable boys and a loving husband. I express my immense appreciation to my husband, Faisal, for not just being the best partner but being a person who exudes a great deal of positivity. He continuously lent me encouragement and kindled perseverance and enthusiasm within me despite the difficult hours. I am equally thankful to my elder sons Talha and Abdullah, for almost always understanding the limitations of a working mother and being extra caring towards their little brother, Ismail.

It goes without mentioning that the overall conducive research environment and facilities at NTNU, combined with the experience of being a researcher at this premier institute, would be the cherishable memories of my life. I am also grateful

to the administrative staff at the Department of Engineering Cybernetics for their support during my stay at NTNU.

Halima Bukhari

Trondheim

Nomenclature

List of Abbreviations

ADC	Automatic Diameter Control
BVP	Boundary Value Problem
CSP	Concentrated Solar Power
Cz	Czochralski
FEM	Finite Element Method
GPC	Generalized Predictive Control
ILC	Iterative Learning Control
IMC	Internal Model Control
IVP	Initial Value Problem
LVSC	Learning Variable Structure Control
MPC	Model Predictive Control
ODE	Ordinary Differential Equation
PDE	Partial Differential Equation
PV	Photovoltaics
RHP	Right-Half-Plane
SDG	Sustainable Development Goals

SMC Sliding Mode Control

SOSM Second-Order Sliding Mode

SSAE Stacked Sparse Autoencoder

VSC Variable Structure Control

Czochralski Hydrodynamical Model (cf. Chap. 4)

α Overall growth angle

α_0 Wetting angle

α_c Cone angle

ϕ Inclination of the meniscus

a Capillary constant

h_c Meniscus height

r_c Crystal radius

r_{br} Bright ring radius

v_g Growth rate

v_p Pulling speed

Czochralski Thermal Model (cf. Chap. 4)

β_{conv} Convective heat transfer coefficient

β_{int} Overall heat transfer coefficient

ϵ_c Emissivity of the crystal

ϵ_m Emissivity of the melt

ϕ_l Heat flux from the meniscus to the interface

ϕ_s Heat flux from the interface into the crystal

σ_{sb} Stefan-Boltzmann constant

A_{fm} Free melt surface area

A_i Cross-sectional area of the crystallization interface

Q_H Heater input

$Q_{int,\,mb}$ Heat transfer from the meniscus to the interface

Q_{int} Overall heat transfer from the melt to the crystallization interface

Q_{in} Heat entering the melt

$Q_{loss,1}$ Heat loss from control volume 1

$Q_{loss,2}$ Heat loss from control volume 2

$Q_{mb,\,bulk}$ Heat transfer from the bulk of the melt to the meniscus

Q_{out} Heat transferred away from the melt

Q_{rad} Radiative heat loss

T_1 Intermediate temperature

T_2 Intermediate temperature

T_S Temperature in the vicinity of the crystallization interface

$T_{B,0}$ Initial temperature of the meniscus

$T_{bulk,0}$ Initial temperature of the melt bulk

T_{env} Temperature of the environment

V_s Volume of the melt

Compensator Design (cf. Chap. 6)

$\tilde{r}$ Compensated measurement

$G_m(s)$ Measurement transfer function

$G_p(s)$ Plant transfer function

G_{hpf} High pass filter

$G_{pc}(s)$ Parallel compensator transfer function

$r_{c,ref}$ Crystal radius reference

Physical Constants for Silicon

ΔH Latent heat of fusion

ρ_l Liquid state density

ρ_s Solid state density

σ_{lv} Surface tension between liquid and vapour phase

a Capillary constant

C_p Specific heat capacity

k_l Liquid thermal conductivity

k_s Solid thermal conductivity

General Parameters

ΔP Pressure difference across the meniscus surface

$\dot{W}_c$ Differential weight gain of a crystal

κ Mean curvature of the meniscus

σ_i Sliding variable

g Gravitational acceleration constant

r Radial coordinate of the meniscus

$R_1,\ R_2$ Principal radii of curvature of the meniscus

R_{cru} Crucible radius

s Length of a small arc or segment of the meniscus boundary

V Lyapunov function

v_{cru} Lifting rate of crucible

z Vertical coordinate of the meniscus

Chapter 1

Motivation and Contributions

This chapter provides the motivation for the research documented in this thesis, both from a global view, and when focussing specifically on the Czochralski process for monocrystalline silicon production. Thereafter, the contributions of the research are explained briefly, and the organization of the thesis is presented.

While the global energy demands are always on the rise alongside the climatic concerns due to the continual use and depletion of natural resources such as coal, oil, and gas, viz., non-replenishable in a human time frame, the quest for renewable sources of energy as well as harnessing them for mankind is a matter of high and increasing interest. In relation to renewable energy sources, the UN has laid down the following sustainable development goals (SDG) (United Nations 2018):

1. SDG1: No poverty
2. SDG7: Affordable and clean energy
3. SDG11: Sustainable cities and communities
4. SDG13: Climate action

These sustainable development goals are clearly interrelated:

I.) Reduction in poverty and higher living standards must be expected to result in higher energy consumption.

II.) The world has abundant affordable energy in the form of coal (and, somewhat less abundantly, of other fossil fuels). However, fossil fuels are not

clean, as they cause large emissions of CO_2, and thereby affect SDG13 negatively.

III.) Making cities and communities more sustainable will contribute positively to climate change, but will clearly require affordable and clean energy.

While carbon capture and storage to some extent can reduce the problems associated with consumption of fossil fuels, it is commonly accepted that society must cover more of its energy needs from renewable sources, such as hydro, wind, solar, and geothermal. The EU has a target to have 32% of its energy from renewable sources by 2030 (increasing from 20% in 2020) (eurostate newsrelease, 17/2020 - 23 January 2020 2020), and to be climate neutral by 2050 (Europen Union 2020). Of all renewable energy sources, solar energy is getting increasingly popular. People can harness solar energy to solar power generation in two different ways: concentrated solar power (CSP) and photovoltaic (PV) power generation. In CSP, the rays from the sun are concentrated by mirrors, using the resultant solar heat to drive a conventional thermal power generator. The PV-based electric power generation, in contrast, converts the energy in the light from the sun directly into electric energy using a semiconducting material. Currently, PV is the dominant form of solar power generation in Europe, with electric power from photovoltaics further anticipated as a major contributor to the desired increase in renewable energy production. Europe has experienced rapid growth of installed PV capacity over the past decade, and this fast growth is projected to continue into the future (SolarPower Europe 2019).

Panels for PV electricity generation use thin wafers of silicon (Si), sliced from bigger blocks of silicon metal. These blocks of Si metal may either possess a poly- or monocrystalline structure (i.e., consisting of a single large Si crystal). On the other hand, the polycrystalline structure has several small crystals or multiple crystals of Si. While polycrystalline Si is easy to produce, monocrystalline Si renders PV panels much higher efficiency. The higher efficiency of monocrystalline PV panels attributes to the single-crystal structure that enables a smooth flow of free electrons for electricity generation. On the other hand, polycrystalline Si possesses a visual grain, i.e., a metal flake effect. The polycrystalline structure is characterized further by non-uniform grain sizes, orientations, and clusters of defects and impurities. These characteristics limit the minority carrier recombination and the overall efficiency (Abdelkader et al. 2010). The use of monocrystalline Si is not only limited to PV panels because these also have widespread applications in electronics – particularly for the production of computer chips.

1.1 Motivation

The object of study in this Ph.D. thesis is the so-called Czochralski process (for convenience often abbreviated as the Cz process). The Cz process will be described in detail in subsequent chapters. This is one of several processes for the production of large single crystals. However, the focus here is on production of monocrystalline Si, for which the Cz process is the industrially dominant one.

Modeling and control of the Czochralski process have been studied for more than half a century. The Czochralski process is demanding owing to its complex thermal dynamics involving complex heat and mass transfers, thereby leading to both time- and spatially- varying operating conditions. There do exist detailed dynamic simulation models for the Cz process. However, while such models are useful for process design and product quality studies, they are very complex and are therefore poorly suited for control design. The effective control system design is further compromised by the lack of direct measurements for the key process variable, i.e., the diameter, and the anomalous behaviours associated with its measurement[1]. Moreover, the control scheme commonly employed in industrial practice relies heavily on operator intervention.

Another distinctive characteristic of the Czochralski process from the viewpoint of its working principle and, of course, control is its inherent batch nature. To understand why the Czochralski process is specifically a batch process, the reader may refer to Sect. 2.4.2. The batch processes are inherently characterized by varying operating conditions without any steady-state values. Furthermore, in batch processes, a predefined set of tasks is carried out repetitively. In general, the effective control of batch processes shall conjointly account for the process control within each run/batch along with the control over various runs, also termed as *run-to-run control*. The distinction between the two strategies is:

I. *in-run* or *in-batch operation* tends to:

   i. improve on the pre-defined trajectories to account for changes happening and information obtained within the present run, and

   ii. use control to track the (improved) system trajectories. The control strategy within each batch can either be the conventional control scheme with nested PID loops (cf. Fig. 2.4) and time-varying feedforward trajectories to compensate for non-steady-state conditions, or an advanced control strategy like MPC.

[1] The anomalous phenomena observed in the Cz measurements are discussed in Sect. 3.4.

II. *run-to-run control*, on the other hand, uses the information from the previous runs to optimize system trajectories for the upcoming run. In this scheme the output can be evaluated after the end of each batch and to counteract any systematic disturbances or variations experienced during previous batches, iterative techniques are applied to improve the end product quality. In the Czochralski process, when using the conventional control structure, the natural way to implement such run-to-run control is by updating the feedforward trajectories between each run as mentioned in the second point of I, i.e., *in-run* or *in-batch operation*. A comprehensive presentation on the control of batch processes can be found in Srinivasan et al. (2003), Srinivasan and Bonvin (2007).

Considering the batch nature of the Cz process, it is, therefore, natural to explore two approaches to improving control quality:

I. The *first approach* is to design systematic run-to-run control of the process. Consequently, there is a potential to explore some kind of iterative learning schemes in this regard.

   In (Rahmanpour et al. 2017), a Kalman-type smoothing estimator provides the basis for the run-to-run control, while Kalman filters and MPC is used for the in-batch control. The approach is quite complex and assumes a measurement of the melt temperature to be available - which is not commonly the case for the production of Si ingots in the Czochralski process. A relatively simple approach utilizing only the measurements commonly available is therefore desirable.

II. *Secondly*, it is natural to focus on the in-run control, attempting to improve the performance of the crystal radius control. A key first step here is a thorough understanding of the measurement scheme employed. Since the measurement scheme makes use of optical diameter sensing with a camera capturing the image of the growing crystal, a ray-tracing method/mechanism (cf. Sect. 5.3) was an obvious choice for the development of the measurement model. In addition, there was a clear motivation to develop a dynamic simulation of the camera image and to understand the mechanism causing the anomalous behaviour in the radius measurement. The presence of this anomalous behaviour has previously been identified in (Gevelber et al. 1987, Winkler et al. 2013). However, existing literature only describes the existence of the measurement anomaly qualitatively, thereby lacking a detailed investigation of the mechanisms causing it.

The detailed understanding of phenomena underlying the measurement anomaly provides an opportunity for improved control design. This has led to the design of a parallel compensator to remove the limitations in achievable performance for feedback (only) control caused by the measurement anomaly, subsequently allowing for faster tuning of the feedback control.

1.2 Contribution

Motivated by the research questions described above, this thesis makes the following key contributions:

I. ***Development of a model for the crystal radius (or diameter) measurement, based on 3D ray-tracing simulation.***. The high reflectivity of Si melt enables optical diameter sensing, which has been modeled effectively via 3D ray-tracing simulation.

II. ***Detailed investigation of non-minimum phase behaviour of the camera-based crystal radius measurement***. Two different measurement principles can be used for measuring the crystal radius, a *weight-based measurement* and a *camera-based measurement*. While it has been known that both these measurements show non-minimum phase behaviour, a detailed explanation of the occurrence of the non-minimum phase behaviour has only been available for the weight based measurement. Nowadays the camera based measurement is more common in industry. This thesis provides a detailed explanation of the non-minimum phase behaviour for this measurement principle, thereby adding to the overall understanding of the process. The analysis combines simplified modeling of the thermal dynamics with accurate hydrodynamic modeling of the melt surface around the crystal base, and detailed ray-tracing to represent the camera image.

III. ***Development of a control scheme to mitigate the non-minimum phase behaviour in camera-based radius measurement***. Although systems theory tells us that the non-minimum phase behaviour is a fundamental limitation on achievable control performance, this problem is circumvented by taking advantage of the fact that the camera based measurement is only an indirect measurement of the real crystal radius. A parallel compensator based control scheme is proposed for *removing* the non-minimum phase characteristic, and enabling fast diameter control without pushing against stability limitations, and therefore achieving fast diameter control with moderate (and not very oscillatory) changes in pulling rate.

IV. ***Iterative learning control (ILC)***. The continual wear of process components

resulting from repetitive batch operations contributes even more to system uncertainties. Thus, a run-to-run control strategy, based on *iterative learning control (ILC)*, was investigated during the preliminary phase of this Ph.D. work (Bukhari et al. 2017). Since the Cz system dynamics suffer from varying parametric, structured, and unstructured uncertainties, the ILC approach was combined with the *second-order sliding mode (SOSM)* to achieve robustness in the overall system performance despite uncertainties and model inaccuracies.

1.3 Publications

The course of this Ph.D. has resulted in the following publications.

paper A: (Bukhari et al. 2019) Bukhari, H.Z., Winkler, J., Hovd, M., "Limitations on control performance in the Czochralski crystal growth process using bright ring measurement as a controlled variable", published in *Proceedings of the 18th IFAC Symposium on Control, Optimization and Automation in Mining, Mineral and Metal Processing*, pp. 129-134, August 2019.

paper B: (Bukhari et al. 2020). Bukhari, H.Z., Hovd, M., Winkler, J., "Design of parallel compensator and stabilizing controller to mitigate non-minimum phase behaviour of the Czochralski Process", published in *Proceedings of the 21st IFAC World Congress, First Virtual Conference*, pp. 11710-11715, July 2020.

paper C: (Bukhari et al. 2021a) Bukhari, H.Z., Hovd, M., Winkler, J.,"Inverse response behaviour in the bright ring radius measurement of the Czochralski process I: Investigation", published in *Journal of Crystal Growth*.

paper D: (Bukhari et al. 2021b) Bukhari, H.Z., Hovd, M., Winkler, J.,"Inverse response behaviour in the bright ring radius measurement of the Czochralski process II: Mitigation by Control", published in *Journal of Crystal Growth*.

paper E: (Bukhari et al. 2017) Bukhari, H.Z., Aftab, M.F., Winkler, J., Hovd, M., "Adaptive Nonlinear Control of the Czochralski Process via Integration of Second Order Sliding Mode and Iterative Learning Control", published in *Proceedings of the 11th Asian Control Conference*, pp. 2732-2737, December 2017.

1.4 Thesis Organization

This thesis has been organized mainly into the following chapters:

Chapter 1 is the introductory chapter that specifies the high-level motivation behind this project, its scope, the contributions of this Ph.D. study, and the research outcome, in the form of publications.

Chapter 2 starts by providing an introduction to processes for the production of large scale crystals, explains the importance of silicon for photovoltaic electricity production, and gives a brief description of the routes for producing raw material for monocrystalline silicon production. The rest of the chapter focuses specifically on the Czochralski process, which is the process used industrially for monocrystalline silicon production and the process investigated in this thesis. The core assembly and basic modes of operation of the process are described, followed by more detailed description of cost and quality-related aspects for the process, and the corresponding operational challenges. The final section of the chapter contains information about the measurements and manipulated variables available for control, and describes the conventional control structure for the Cz process.

Readers interested primarily in the Cz process may skip directly to Sect. 2.3, while readers already familiar with the Cz process including its control and operation may skip the entire chapter.

Chapter 3 presents an in-depth literature review of the Cz growth process, covering miscellaneous aspects of modeling, control, and functional measurements, that have been employed by the research community. The analysis of the basic meniscus profile, pioneered by *Young and Laplace*, and its numerical approximations proposed by other researchers, are also discussed here.

Chapter 4 presents mainly the Cz growth dynamics at the crystallization interface. Also presented in this chapter is a simplified heater model that mimics the thermal environment, experienced by the crystallization interface, in a much coarser sense. The use of this heater model is postponed until Chap. 6, where the main focus is testing of the designed control scheme in an approximate, yet qualitatively reasonable thermal environment. Hence, an accurate thermal model is not required in this context. The modeling work in this chapter evolves from the previously published models, in particular, (Winkler et al. 2010a) and (Rahmanpour 2017).

Chapter 5 covers the ray-tracing method for the estimation of a controlled variable (crystal radius) in great detail. The findings of this method, i.e., the estimation of crystal radius in the form of bright ring radius and its dynamic simulation, revealing the presence of anomalous behaviour, i.e., the inverse response characteristics, are also presented here. This chapter is based on the work presented in Paper C (Bukhari et al. 2021a).

Chapter 6 covers the scheme for the linearization of nonlinear Cz growth dynamics, accompanied by the design of a parallel compensator to mitigate the undesired inverse dynamics, revealed by the bright ring radius measurement. Additionally, the design of a feedback controller, which when combined with a parallel compensator, yields a fairly good response for the overall Cz system without any bandwidth limitations, is also the main topic addressed in this chapter. The testing and validation of the proposed control scheme in a nonlinear dynamic environment, including testing the response to disturbances entering through the energy balance about the interface, are also given.

This chapter is based on Paper D (Bukhari et al. 2021b), where some effort is spent on introducing control concepts to the crystal growth community. The corresponding material is trivial to control engineers, and readers with a strong background in control may therefore want to skip parts of this chapter.

Chapter 7 discusses the application of the iterative learning control (ILC) method on the Cz crystal growth process. This chapter is based on Paper E (Bukhari et al. 2017).

Chapter 8 is the last chapter that summarizes this dissertation. In addition, relevant further work is described, both with a view to bring the results from this thesis to industrial practice, as well as more theoretical work and extensions to what is reported here.

It is to be noted that this thesis format resembles a paper-based dissertation such that papers are reformatted to make standalone chapters ranging from Chap. 4-Chap. 7. Therefore, repetitions in these chapters are a natural consequence. The reader may choose to skip the repetitive content.

Chapter 2

Background

This chapter provides background information for the research reported in this thesis. The first two sections cover the general background, i.e., Sect. 2.1 provides an overview of alternative processes for the production of large-volume single crystals, while Sect. 2.2 focuses on the importance of Si for photovoltaic (PV) applications, and describes the routes for preparing raw material for the Cz process. These sections may be skipped for readers interested only in the Cz process as such.

Sections 2.3 and 2.4 describe the Cz process itself and the challenges and objectives of Cz crystal growth, while Sect. 2.5.3 describes the conventional control scheme for the process. Readers already familiar with the process will find little new also in these sections.

There has been a tremendous development in the field of crystal growth over the past three decades (Fornari 2018). Among a wide range of crystalline materials developed or produced commercially, those with semiconducting characteristics are of particular interest from our perspective. These semiconductor crystals form a base material in the production of microelectronic and optoelectronic devices that are used further in a myriad of applications.

Several physical phenomena of coupled nature are involved in the creation/ production of bulk crystals. The growth of bulk crystals is primarily affected by heat and mass transport, capillarity, heat radiation, phase change, and anisotropic material characteristics (i.e., properties of a material exhibiting different magnitudes in different directions) (Fornari 2018). Moreover, the thermodynamic properties also influence the growth of bulk crystals. The understanding of these coupled phenomena is crucial for growing good quality crystals with fewer defects and

uniform properties. In a nutshell, several scientific and engineering disciplines, ranging from materials science to automation and control are required to understand all the essential aspects of the crystal growth process.

The key issues in the application of control engineering to the growth of crystals are:

(a.) The high temperatures involved in the crystallization methods, and the scarcity of online measurements imply a model-based approach to control design. *(b.)* While detailed simulation models exist, these are typically developed for system design purposes rather than control, and typically do not simulate the measurements used for control (i.e., the camera-based measurement of crystal radius). Furthermore, the scarcity of online measurements means that updating these models from real-time measurements will be very difficult. This makes advanced control methods such as Model Predictive Control, based on online dynamic optimization, inapplicable. *(c.)* Therefore, control design needs to be based on simplified dynamical models representing the main dynamic phenomena in the plant. This approach is adopted in this thesis.

2.1 Bulk Crystallization Techniques: An Overview

An overview of bulk crystallization processes, addressed in this section, has been excerpted mainly from the multi-author book edited by Dhanaraj et al. (2010a).

An orderly repetitive array of atoms is formally known as a crystal. The subject of crystal growth, be that related to crystals occurring indigenously in nature or produced commercially, is too diverse to be discussed in detail within the purview of this thesis. Therefore, the crystallization process can be categorized broadly on the basis of phase transformation from either of the solid, liquid or vapour phase that the solid crystal is grown from. The *solid-solid* phase transformation is rarely employed except for the growth of few metals or metal alloys (Dhanaraj et al. 2010a). Within our context of bulk single crystals growth, only the crystals grown from the liquid or molten phase are of prime concern.

One of the traditional ways of crystal growth, starting from the liquid phase, is the *solution method*. The solution from which crystals are grown may be any of the three categories: high-temperature solution, low-temperature aqueous solution, or even superheated aqueous solution. The crystals produced out of this process have numerous uses not only in specialized technologies but also in everyday products such as foods, dyes, fertilizers, and pharmaceuticals, to mention a few.

Another important category in the growth of crystals from the liquid phase is the one starting from the *vapour phase*. This technique is commonly employed in

the growth of electronic-grade crystals and has a much lower cost and a higher throughput as compared to those starting from the melt phase (cf. the discussion below). Moreover, it is employed extensively for the growth of advanced epitaxial structures, thin films, and substrates.

The crystals grown from this method tend to have a lower concentration of point defects and dislocation densities compared with crystals grown from the melt because the working temperatures are lower than those of the melting point. Moreover, if the material undergoes an incongruent melting phenomenon, i.e., non-uniform melting followed by the creation of a compound with a composition different from the melt, vapour growth may be the only choice for the growth of single crystals.

Last but not least, there are the most popular techniques of crystal growth, i.e., those which start from the melt phase. In practice, more than half of the crystals used in various technologies are derived from the melt method (Dhanaraj et al. 2010b). On a commercial scale, this method grows large single crystals with reasonable growth rates. Moreover, this method is best suited for the growth of materials with stable melt configuration, i.e., when the respective melts don't undergo any decomposition or polymorphic transformations and have a reduced chemical reactivity. Thus, the materials grown widely from the melt method include elemental semiconductors, pure metals, compounds of oxides and halides, etc.

There are several variants of the melt growth technique, while the choice of any specific technique depends on the physicochemical properties of a material as well as the distinctive characteristics of each growth method (Fornari 2018). The material properties that are essential to consider from the growth perspective are its melting point, its volatility, and solubility in water or other organic solvents, to name a few.

The *Czochralski* growth process is the main topic of this thesis, therefore it will be discussed in detail in Sect. 2.3. A concise overview of the other standard techniques for bulk single crystal growth is presented in the following:

I The *Verneuil method* – pioneered by the French scientist *Auguste Verneuil* in 1883 – is not only the oldest of the melt techniques but also the first to develop on a commercial scale for the production of high melting point materials. Traditionally, this method began with the growth of synthetic gemstones like sapphire and some rare varieties of ruby (Carter and Norton 2007). Apart from precious gemstones, today, this method produces high-quality crystals for laser devices, precision instruments, and even substrates for thin film growth (Carter and Norton 2007). Due to its principle of oper-

ation, this method is often termed as the *flame fusion* technique as the seed crystal has a molten top fed with the molten drops of the source material (i.e., powdered material passing through flame or plasma) (Dhanaraj et al. 2010a).

One main advantage of the Verneuil method is that no crucible is required to contain the melt except for a shallow pool of liquid held above the seed crystal through surface tension. Generally, the reactivity of the melt with the container is more pronounced at high temperatures. Even if the reactivity is less of a problem finding suitable materials for the crucible that can withstand high temperatures is not easy. The main disadvantage of this process is relatively poor control of growth parameters, particularly the melt temperature, because of little melt volume (Carter and Norton 2007).

II The *Floating Zone (FZ) method* was developed at Bell laboratories in the early 1950s by *H.C. Theuerer* (Dabkowska and Dabkowski 2010). This method is similar in essence to the Verneuil method as it is also *crucible-free* – the feed rod material being its own crucible. Due to the absence of crucible, the concentrations of impurities are significantly lowered, thereby leading to the production of high-resistivity Si (Carter and Norton 2007). Though high quality bulk single crystals of Si can be produced through a well-established and highly mature Czochralski technique (cf. Sect. 2.3), however for some important electronic applications, the Si crystals produced through the Cz method are not of sufficient quality. Though the FZ method produces high-quality crystals, it is not amenable to the growth of large-sized crystals (Carter and Norton 2007) as the reported crystal sizes grown by this method are of merely a few millimeters in diameter and a few centimeters in length (Dabkowska and Dabkowski 2010). Today the variants of this method are even applied to various congruently and incongruently melting oxides.

The name floating zone is derived from the fact that the liquid-solid interface is somewhat floating between the polycrystalline Si feed rod at the top and the monocrystalline growing crystal at the bottom. In a general configuration, the feed rod is melted by contactless inductive heating via the radio frequency (ca. 3 MHz) magnetic field of a one-turn induction coil. The zone *floats* upward due to the relative movement between the heating coil and the silicon rods. The induction coil and the RF generator are fixed and crystal and rod are moved downward while rotating (Muiznieks et al. 2015, Lüdge et al. 2010).

III The *Bridgman technique* (also known as *Bridgman-Stockbarger method*) is also one of the oldest techniques for growing crystals from the melt. With

subtle differences between the Bridgman and Stockbarger techniques, the crucible containing the molten material in the former technique is translated along the axis of a temperature gradient in a furnace, whereas in the latter technique, a specialized furnace is used with two heating elements separated by an adiabatic zone. This is the most common method for the production of single crystals of compound semiconductors, i.e., compounds of elements from groups (III-Vs or II-VIs) of the periodic table (Jurisch et al. 2015) halide and chalcogenide crystals, and several oxides for scintillation or laser applications (Duffar and Sylla 2010).

At first the polycrystalline material in the crucible needs to be melted completely in the hot zone and be brought into contact with a seed at the bottom of the crucible. A part of the seed gets remelted when it touches the melt. This provides a fresh interface for the crystal growth. The crucible is then translated gradually into the cooler section of the furnace. The temperature at the bottom of the crucible falls below the solidification temperature and the crystal growth is initiated by the seed at the melt-seed interface. After the whole crucible is translated through the cold zone the entire melt converts to a solid cylindrical monocrystalline ingot (Dutta 2010).

The Bridgman technique can be implemented in either a vertical (*Vertical Bridgman technique*) or a horizontal system geometry (*Horizontal Bridgman technique*). The concept of these two configurations is similar. In the case of the horizontal Bridgman technique, the material to be crystallized is contained in a boat-shaped crucible. First, the material gets melted while passing through the heater and finally crystallized. Like other techniques, a seed crystal with desired crystallographic orientation is placed at the top of the crucible. The crystals formed are not cylindrical but acquire the same shape as that of the crucible boat. However, the crystals grown horizontally exhibit high crystalline quality (e.g. low dislocation density) since the crystal experiences lower stress due to the free surface on the top of the melt and is free to expand during the entire growth process (Duffar and Sylla 2010, Dutta 2010).

IV The *Gradient Freezing technique* is similar in essence to the Bridgman technique. Analogous to the Bridgman technique, the gradient freezing technique can also be realized in vertical and horizontal configurations. While keeping the furnace system as well as the crucible containing the melt and the seed stationary, the temperature gradient is translated to obtain directional solidification. The translation of the temperature gradient is implemented by using a multiple-zone furnace wherein the power to each zone is programmed and controlled by individual PID controllers. This system can

maintain the same temperature gradient at the liquid-solid (i.e. melt-crystal) interface, which changes in turn its location with time during the growth. This method is also used for the growth of binary compounds (Dutta 2010). This technique is mainly used for the production of III-V-semiconductors like gallium arsenide ($GaAs$) or indium phosphide (InP).

V The *Kyropoulos method*, named after the Greek-German scientist *Spyro Kyropoulos*, was regarded as one of the leading technologies for the growth of large single crystals particularly before world war II. The Kyropoulos method, being a variant of the Cz process, performs crystallization by slow cooling as opposed to gradual crystal pulling in the Cz process (Lan 2010). The main difference between the two techniques are the different curvatures of solid-liquid interfaces and the shapes of growing crystals. In Kyropoulos crystallization, the crystal growth starts with a flat top to minimize the formation of twins[1] (Bliss 2010). With the Kyropulos method, the crystal is an ellipsoid of rotation with its centre submerged completely in the melt (Bliss 2010).

To summarize, each technique offers a unique set of thermophysical conditions that make it preferable to a specific class of materials. Sometimes slight modifications to a standard growth technique are necessary to make amenable the growth of certain materials. Thus, crystal growth is a challenging discipline where a thorough insight into a specific growth technique and a sound knowledge of the desired material properties are necessary.

2.2 Silicon: the Enabling Material in PV

The structural, chemical, and electronic properties of single-crystal silicon have been revealed by more than 65 years of research and development, carried out by governments and industries worldwide (Kearns 2019).

At room temperature, silicon is merely an insulator. However, with the addition of small electronic impurities (dopants), silicon can become a conducting material with electrons in the conduction band and holes in the valence band, thereby making it a semiconductor. The single crystal of semiconductor silicon (Si) is a phenomenal material with unique electrical, mechanical, and physical properties. Due to these properties, silicon qualifies as a core material in many state-of-the-art micro-and optoelectronic devices with structurally robust and high-temperature resistant applications (Sinno et al. 2000), such as electronics, photonics, communication systems, and photovoltaic industries (Zharikov 2012).

[1]The crystal twins refer to two separate crystals sharing some of the same lattice points (Carter and Norton 2007)

Due to increased demand for PV systems, several programs for upgrading naturally occurring silicon have continued to progress actively over the past many decades. These programs encompass all the initiatives and efforts to make the production of purified[2] polycrystalline silicon (a starting material for bulk single crystal) both cost-effective and efficient. The *polycrystalline* silicon has a structure comprising of multiple small crystals with small grain size and a high density of grain boundaries [3]. These grain boundaries trap the electrons, and consequently, the minority carrier lifetime becomes considerably low. The polysilicon structure is often converted to a single crystal ingot to enhance its usefulness (i.e., improved minority carrier lifetime) in electronic and solar cell applications (Maurits 2014).

With the recent advancements, the purity level of polysilicon has reached a remarkable level of eleven nines, i.e., 11N/99.999999999% (Kearns 2019), thereby enabling greater control and less variation of silicon bulk crystal properties. The main benefit of purified silicon is rendering improved performance and higher efficiency to the final product via relatively larger thermal conductivity, withstanding higher thermal gradients, and fast solidification and cooling rates.

It has been reported by multiple sources (Narayanan and Ciszek 2010, Delannoy 2012) that more than 80% of the solar modules are produced from silicon crystals. However, in some references, these figures are reported to be even higher than 90% (Müller et al. 2006). The feedstock for the PV industry is either monocrystalline silicon (a highly purified form of polysilicon produced by the conventional Siemens polysilicon process or by a fluidized bed process) along with the silicon recycled from wafer manufacturing (Narayanan and Ciszek 2010, Delannoy 2012).

The value stream of silicon, encompassing all the main steps for refining this natural raw material to a photovoltaic-grade (PV-grade) or electronic-grade (E-grade) silicon, is highlighted below.

2.2.1 Raw material for monocrystalline silicon

Silicon is the second most abundant element by mass in the Earth's crust. While silicon rarely occurs in its pure elemental form, more than 90% of the Earth's crust is made up of *silicates*, in which silicon is bound to oxygen, such as SiO_2, SiO_4 and Si_2O_7, to name a few. Silica, the dioxide form of silicon (SiO_2), is both thermally and chemically stable native oxide (Kearns 2019), i.e., quartz.

[2] from the undesired contaminants like metals and heavy elements

[3] The varying orientations in polycrystalline structure appear as small crystals or *grains*, while the interfaces between these grains are termed as the *grain boundaries* (Maurits 2014).

2.2.2 Purification of silicon

Undoubtedly, the purer the silicon, the higher the efficiency of solar cells; however, the main limiting factor is the increasing cost incurred due to higher purification levels. The naturally occurring silicon is purified to the solar/PV-grade or electronic/semiconductor (E-grade) silicon, depending upon the extent of purification. The PV- or E-grade silicon signifies the level of purity that makes each material amenable for use in the corresponding industry, i.e., photovoltaic or electronic industry, respectively. The minimal level of purity for PV-grade Si is 6-7N (i.e., six/seven nines or 99.9999/99.99999%) (Hosseinpour and Tafaghodi Khajavi 2018), while this purity level for Si wafers in the semiconductor industry is 9N (Safarian et al. 2012) and in some references, this value is reported up to ≈11N (Itaka et al. 2015). Since the allowable concentrations of impurities in semiconductor-grade Si are much lower than those in the PV-grade; therefore, the silicon used for semiconductors is the purest and “most structurally and chemically perfect" material made by man (Kearns 2019).

For either PV- or E-grade specifications, the silica/quartz (a crystalline form of Si) is purified first to the *metallurgical grade* (MG) silicon. This MG-grade Si is further treated via the chemical or metallurgical route to obtain semiconductor or solar-grade materials, respectively. The purified MG-Si suitable for the PV industry is commonly referred to as the *upgraded metallurgical grade* (UMG) Si (Maurits 2014).

The first processing performed on a quartz material is the carbothermic reduction of silica, i.e., removal of oxygen from silica by reaction with carbon at high temperatures (1500 °C to 2000 °C). This process takes place in an electric arc furnace and results in the metallurgical grade (MG) silicon (Delannoy 2012, Braga et al. 2008), with purity level often reported to be 98.0-99.0 % (Maurits 2014).

The MG-silicon produced from carbothermic reduction may contain impurities from the silica and carbon raw materials as well as the electrodes of the arc furnace. One way to reduce them is to use almost pure raw materials, such as carbon black and milled silica (or sand) derived from high purity quartz rock with low concentrations of iron, aluminium, and other metals (Delannoy 2012).

At this point, the MG-silicon contains undesired metallic impurities such as Fe, Al, Ti, Mn, C, Ca, Mg, B, P, to name a few (Safarian et al. 2012).

From metallurgical grade silicon, there are further two routes of silicon purification depending upon its subsequent use, i.e., feed material for producing either PV- or E-grade silicon (Delannoy 2012, Braga et al. 2008). These two routes for purifying MG silicon are:

Metallurgical Route:

A crucial step in poly-Si purification on the metallurgical route is the removal of boron (B) and phosphorous (P). These materials, with relatively high distribution coefficients, viz., the ratio of concentration in the solid to that in the melt, make their separation quite challenging. However, the commonly employed subprocesses, for the removal of the majority of impurities on the metallurgical route, except B and P, are based on the *directional solidification* (Delannoy 2012, Gribov and Zinov'ev 2003, Hosseinpour and Tafaghodi Khajavi 2018) and *acid leaching* methods (Safarian and Tangstad 2012). These processes exploit the segregation properties of metallic/non-metallic impurities. In directional solidification of the melt, both the heat necessary to be removed from the melt for solidification and the latent heat generated due to phase change flow along the same direction, usually in the vertical direction. The end part with concentrated impurities is removed afterward. Many metallic impurities have high concentrations in molten Si. During solidification of molten MG-Si, the majority of these impurities precipitate at grain boundaries in polycrystalline silicon. Hence, acid leaching of MG-Si dissolves the impurities located at the grain boundaries of silicon, while keeping the silicon matrix intact (Safarian et al. 2012).

As mentioned earlier, due to relatively large segregation[4]/distribution coefficients, the removal of both B and P via directional solidification (Safarian et al. 2012; 2013) is neither feasible nor cost-effective. Therefore, these deleterious impurities are dealt with through two important processes, namely the *slag refining* (effective for removing Boron) and *vacuum refining/distillation* (effective for removal of phosphorous) methods on the metallurgical route.

The application of slag refining processes for the removal of B from silicon has been extensively studied and commercialized in the *ELKEM Solar Silicon process (ESS)* in Norway (Safarian et al. 2013). It is a well-established process on the metallurgical route and can be performed economically on a large industrial scale. The boron impurity in molten Si is first oxidized and then gasified for its effective removal by the molten silicate slags. Safarian et al. (2013), Hosseinpour and Tafaghodi Khajavi (2018) have investigated various compositions of silicate slags of which $CaO - SiO_2$ and $CaO - Na_2O - SiO_2$ are the most commonly used. The temperature, as well as the chemical composition of slag, greatly affect the removal of boron by altering its concentration levels in slag and molten Si (Safarian et al. 2012, Safarian and Tangstad 2012, Safarian et al. 2013). It is noteworthy

[4] A generic definition of this parameter is simply a ratio of the solute concentration (C_S) within the solid crystal and the molten charge (C_L), i.e., $k = C_S/C_L$. However, some other definitions, taking into account the actual growth conditions are also defined in literature to derive more accurate segregation models (Friedrich et al. 2015).

that the Elkem solar process doesn't employ any specific method for phosphorus removal; the P elimination can take place likely to some extent through the slag refining (Safarian et al. 2012). Later, the directional solidification and acid leaching processes are carried out in the ESS process to obtain UMG silicon.

Some other methods, (cf. Safarian and Tangstad (2012) for a more comprehensive review) employed on the metallurgical route are *plasma refinining* and *solvent refining* (Safarian et al. 2012, Hosseinpour and Tafaghodi Khajavi 2018). Despite the promising results of the last-mentioned method, there are challenges and limitations to its industrialization.

Chemical Route:

The most common *chemical route* for the purification of polysilicon is the *Siemens process*. The MG-grade Si is allowed to react with HCl at moderate temperatures to form trichlorosilane (TCS) $SiHCl_3$ at the first stage (Delannoy 2012). In the second stage, further purification is obtained through distillation by boiling TCS at 32 °C. In the third stage, the TCS is broken down in a reducing atmosphere at around 1000 °C, so that Si atoms from the vapour are deposited on a cylindrically arranged array of thin Si rods. This *chemical vapour deposition* (CVD) process produces thick rods of highly pure silicon. Dopants such as boron, phosphorous, or arsenic are introduced at the desired concentrations to produce p-type (B) or n-type (As, P) solar cells. After deposition the rods are removed from the reactor and broken into small polysilicon pieces – thereby providing a starting material for the silicon growth used later in semiconductors (Cowern 2012).

Two of the main drawbacks of the Siemens process are its high cost and the involvement of toxic materials like trichlorosilanes, hydrochloric acid and chlorine emissions, all needing utmost care and specialized handling (Braga et al. 2008). There have been concerted efforts to reduce the purification cost of silicon feed material.

Norway is a major producer of MG-grade silicon, ranking third in the world (USGS 2020). There has also been significant research on silicon purification (Braga et al. 2008, Safarian et al. 2012), leading in 2009 to the opening of Elkem Solar's plant at Vågsbygd in Kristiansand for the production of PV-grade Si. The production in this plant is based on a *fluidized bed reactor* (FBR), and is claimed to have significantly lower capital cost and lower energy consumption per ton of PV-grade silicon produced compared to the conventional Siemens process. The plant in Kristiansand is now a part of the REC Group.

A good and concise resource on various silicon purification projects run by different governments, be those including chemical refinement or metallurgical refine-

ment, are presented in Müller et al. (2006). Similarly, interested readers may find reviews on proposed schemes and research processes for the purification of PV-grade feedstock material in the following references: (Gribov and Zinov'ev 2003, Itaka et al. 2015, Safarian et al. 2012).

2.3 The Czochralski Process

The *Czochralski* (Cz) process is named after the Polish chemist *Jan Czochralski*, who accidentally discovered it in 1916 while examining the crystallization rates of various metals. This process is renowned for producing single crystals of a wide range of materials such as metals, minerals, salts, semiconducting materials (Si, Ge, GaAs), and gemstones. Today, Czochralski is an advanced industrial technique used mainly for the production of monocrystalline silicon ingots on a commercial scale, i.e., contributing to almost 90% of the worldwide production of purified monocrystalline Si. The high-purity Si ingots, when transformed as substrates and wafers, find widespread usage in both electronics and photovoltaic industries, respectively.

In an industrial framework, the production assembly of Si ingot is often called a *pulling chamber* or simply, a *puller*. As the name suggests, the industrial Cz pullers make use of a pulling mechanism that supports the seed crystal of the desired monocrystalline lattice structure. With the seed crystal lowered into the surface of molten Si, the pulling mechanism results in the solidification of molten Si at the base of the seed crystal. The solidification process is controlled in a way to yield a cylindrical structure of the solidified Si, commonly referred to as an ingot or a boule.

With the precise control of the thermal gradients, pulling speed and rotation rates, the production of larger sizes of silicon crystal ingots can be achieved. Furthermore, modern state-of-the-art Cz systems can support a much higher capacity of molten Si charge, i.e., above 500 kg capable of producing crystal diameters up to 450 mm.

The automatic control of the Cz process is essential, not only to achieve maximum yield and reproducibility but also to produce crystals with fewer diameter fluctuations and lower levels of defects and impurities (Tatartchenko 2010). The absence of defects and impurities allows for a perfect lattice structure with the highest light-to-electricity conversion efficiency for the silicon wafers produced from the crystals — a prime quality consideration for photovoltaics. Moreover, a constant (well-controlled) diameter means balanced growth/thermal conditions that limit the possibility of defect formation. In addition, the cutting-off of expensive material in the post-grinding of the Cz crystals can be reduced significantly

with a better diameter control of the Cz ingots. Hence, a well-controlled Cz system not only results in an improved quality of the final product outcome but enhances the cost-effectiveness of the overall process.

2.3.1 Principle of operation

The Cz process commences by dipping a continuously rotating seed crystal (of monocrystalline lattice) into the molten silicon and withdrawing it gradually out of the melt. The moment the seed crystal touches the melt, the molten Si starts to solidify around the seed crystal with the same monocrystalline structure as that of the immersed seed. The solid crystal is then pulled slowly out of the melt, carefully balancing the pulling rate and the crystal growth rate. Due to surface tension/capillary forces, a *meniscus* is formed. The meniscus is a small volume of molten Si that is lifted above the horizontal surface of the melt and connects the solid crystal with the molten Si. The phase change from liquid to solid phase takes place across the boundary separating the growing crystal from the molten Si. This boundary is referred to as the *melt-crystal interface* and is depicted schematically in Fig. 2.1.

With the Czochralski method, the growing crystal surface never comes in direct contact with the crucible walls. This technique is different from the traditional crystal fabrication techniques which produced bulk crystals in a vessel, i.e., similar in essence to the casting method. Instead, the shape of the lateral crystal surface depends on the shape of the melt meniscus, which in turn, is controlled by the surface tension/capillary forces (Tatartchenko 2010). Furthermore, the heat and mass transfer phenomena across the interface region determine the quality of the finished crystal.

As a means for controlling the crystal-melt interface shape and the transfers of mass (e.g., dopants, oxygen) and convective heat flow around the crystallization interface, the crystal and crucible are rotated continuously in opposite directions at appropriately pre-designed rotation rates (Noghabi et al. 2011, Friedrich 2016).

2.3.2 Assembly of a Czochralski crystal puller

Fig. 2.2 shows the Cz puller assembly for the silicon ingot production. The main inner structures of the pulling chamber, collectively known as the hot zone (HZ), are shown, except the heat shield[5]. A typical Cz crystal puller is a vacuum furnace comprising mainly of the lifting and rotating assemblies for both the crucible and the growing crystal, the hot zone (HZ) assembly, receiving chamber to receive the growing crystal, specialized mechanisms for providing effective vacuuming,

[5]Since the heat shield around the growing crystal obscures the view of other HZ components, therefore, for a clear view of the heat shield, one can refer to Fig. 5.4.

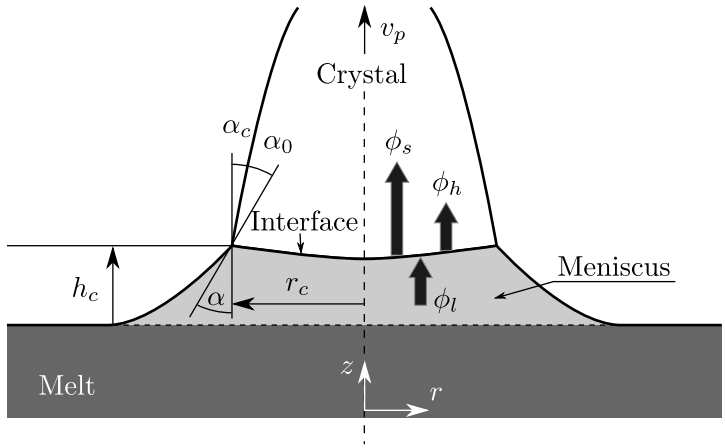

Figure 2.1: Schematic view of the crystal growth regime indicating the melt-crystal interface boundary that separates the growing crystal from the raised melt meniscus above the molten semicoductor.

cooling, and purging[6] of the Cz system and, last but not least, a control console.

The hot zone, being the most crucial assembly in the Cz puller, provides proper temperature distribution required for efficient crystal growth. In the case of the hot zone itself, the key elements include silica/quartz crucible, graphite susceptor (not shown explicitly in Fig. 2.2), heat shield around the growing crystal, and lastly, the annular and base heaters. A brief introduction of the HZ components that play a key role in the regimen of crystal growth are listed below:

- *Crucible*: The crucible and its contents play a pivotal role in the crystallization phenomenon. The crucible is a vessel that contains the feedstock material (polysilicon) that is heated up to produce Si melt to proceed with the crystallization. To prevent the contamination of Si crystal from the crucible material, chemically inert material such as fused silica (SiO_2) is a preferred choice for the construction of the crucible. With the ongoing crystallization, the melt level drops, therefore the crucible is gradually lifted upwards so that the level of the three-phase boundary (melt-crystal-vacuum) can be maintained constant despite the fall in melt height.

- *Seed Crystal*: The seed crystal plays a fundamental role as its main purpose is to provide the crystallographic orientation for the entire ingot in addition to supporting the ingot. It is clamped by a seed holder/chuck and

[6]The growth of the Cz crystal takes place in a water-cooled vacuum chamber where the continuous flow of inert gas, i.e., argon, is maintained.

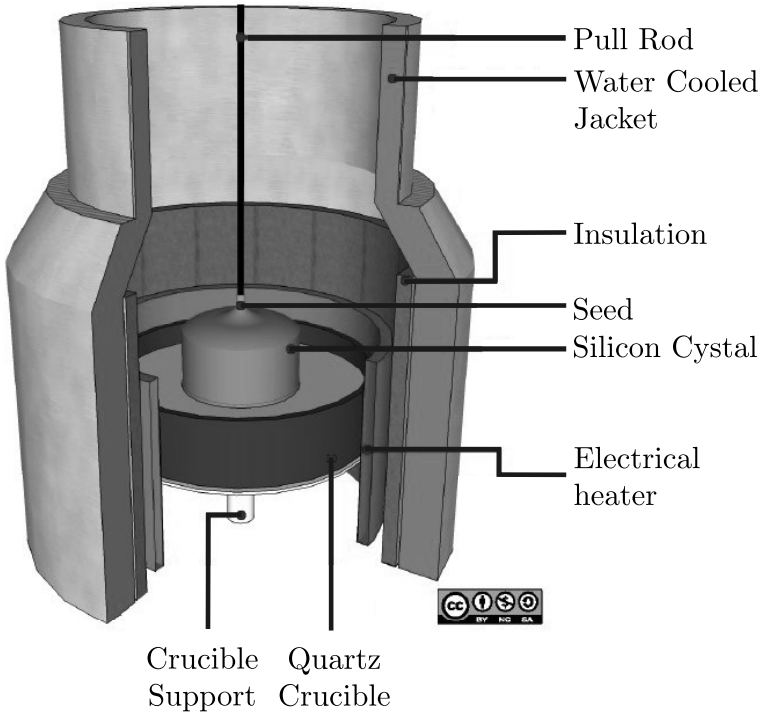

Figure 2.2: Assembly of a typical Cz puller (Rahmanpour 2017).

suspended from a stainless steel wire/rod. At a suitable melt temperature, slightly higher than the silicon melting point, a seed crystal is dipped into the melt and gradually lifted upwards until the end of crystallization. The formed crystal will have the same crystallographic orientation as that of the seed itself.

- *Camera*: Though the camera is not directly a part of the HZ, it is auxiliary equipment that should be focused on the melt surface in the vicinity of the three-phase boundary at all times. It is installed at one of the viewports on the pulling chamber to capture the image of the glowing meniscus[7]. The brightness pattern on the meniscus image serves as an estimate of the radius of the growing ingot. Thus, the crucible lifting mechanism enables the optical measurement system to continue focusing at the same location, thereby removing the need for any camera readjustments due to the dropping melt level.

[7]Changes in the camera position will cause shifts in the radius measurement. Operators are therefore careful to avoid bumping into the camera when cleaning the puller and preparing it for the next run.

- *Susceptor*: Traditionally, graphite is the most suitable material when it comes to high-temperature exposures similar to those experienced by the hot zone interior. The graphite susceptor holds the quartz crucible, thereby providing mechanical support and reinforcement to the quartz crucible, which may otherwise get softened and distorted at high temperatures. Furthermore, the high heat conductivity of the graphite material allows the heat from the heaters to be distributed uniformly around the walls of the crucible (Anttila 2015).

- *Heat shield*: The heat/radiation shield is a circular funnel-shaped structure that extends above the melt surface like an inverted frustum of a cone while surrounding the growing crystal. It is usually made of molybdenum or graphite and offers a wide range of benefits. Firstly, it shields the growing crystal from the heat radiating from the hot crucible walls. Consequently, the radiative heat transfer from the crystal surface can be improved, which, in turn, permits the increase in the pulling rate. Secondly, the axial temperature gradient can be increased (Su et al. 2010), which is important for controlling the concentration of intrinsic point defects (Friedrich et al. 2015, Voronkov 1982). Thirdly, the radiation-induced heat losses, from the melt surface to the top of the chamber, can significantly be reduced (Su et al. 2010). Lastly, the heat shield guides the argon flow for effective purging of the system.

  The heaters and the cooled walls of the main vessel are also separated by insulation layers usually made of graphite felt or foil. These insulation layers, also referred to as the bottom heat shield, reduce the heat losses considerably and provide improved power consumption.

- *Argon gas flow*: During the crystallization, the dissolution of the quartz crucible results in the release of oxygen into the melt. More than 99% of oxygen leaves the melt as SiO, but the remaining small amounts stay in the melt and get incorporated into the growing crystal (Friedrich et al. 2015). Furthermore, the evaporating SiO from the melt interacts with the hot graphite susceptor to form carbon monoxide CO, which then reenters the melt and causes the potential transport of carbon in the crystal (Newman 1982). Both SiO and CO are undesired as the former is a volatile and corrosive oxide, while the latter tends to precipitate as SiC at the silicon crystal (Dold 2015). Thus, the heat shield guides the argon flow (from top $\rightarrow$ bottom of the chamber) closely along the melt surface to efficiently purge the system of undesired SiO and CO. Moreover, argon is an inert gas with poor thermal conductivity. It facilitates better insulation of the hot areas around the melt from the water-cooled vacuum chamber walls. Modern Cz pullers, particularly the PV related ones, operate at reduced pressure of approximately

$5\,\mathrm{mbar}$ to $50\,\mathrm{mbar}$, while the argon flow is kept in the range of $10\,\mathrm{L\,min^{-1}}$ to $30\,\mathrm{L\,min^{-1}}$ (Dold 2015). Oftentimes, in preparation for the production of a new ingot and prior to purge gas flow, a leak test is performed to ensure a vacuum-proof environment to prevent oxygen from entering the pulling chamber during the crystal production.(Anttila 2015).

- *Heaters*: The Cz pulling chamber is equipped with an annular/main heater and a base/bottom heater. For the construction of heaters, graphite material, owing to its excellent electrical and thermal conductance properties, is used. The heater is usually connected to two or four electrodes at its bottom edge, using a support structure made from graphite. The electrodes deliver the required power ranging from a few tens of kW to well beyond $100\,\mathrm{kW}$ (Anttila 2015).

Lastly, in the case of any unfortunate event, if the high-temperature silicon melt spills[8] at the base of the chamber, considerable damage may occur to a rather expensive crucible lifting and rotating mechanism. Furthermore, the molten silicon may come in contact with the water from the water-cooled vacuum chamber that may lead to dangerous steam or detonating gas explosion. Therefore, as a contingency, most hot zones are equipped with trays to hold up silicon charge spillage (Anttila 2015).

2.3.3 Stages of the crystal growth process

When producing a Si ingot in the Cz process, the first step is to charge the crucible with silicon pellets. While charging the crucible, the operators need to take special precautions to eliminate any risk of contamination to both the crucible and its contents. Thereafter, a fully charged crucible is placed at its designated location inside the pulling chamber. The various steps involved in single batch production of a crystal ingot, through the Cz process, are outlined in Fig. 2.3 and listed below:

I *Melting*: One of the prime considerations before starting each run of silicon ingot production is to ensure a vacuum-proof environment in the growth chamber, effectively purged with the flow of inert gas like argon. Once the growth environment is made vacuum-proof with the reduced operating pressure, the melting of the silicon starts. Without any proper vacuum, contamination into the melt and the crystal surroundings result due to the airflow.

The temperature within the growth chamber is increased to a level slightly above $1420\,^{\circ}\mathrm{C}$, which is the melting point of Si. The temperature is maintained there for a while to allow complete melting of silicon feed/pellets

[8] The occurrence of any leaks or cracks is quite rare, though.

while ensuring the removal of any tiny bubbles that may otherwise generate voids or other crystal defects (Shimura 2017).

Once the Si feed is fully melted, i.e., after a few hours, the crucible is raised to the desired starting position. The operators use their acquired experience to stabilize the melt temperature before dipping the seed into the melt. At this stage, a careful adjustment of heater power is essential to control the melt temperature at the right level before dipping the seed crystal into the melt. At a temperature lower than the desired, the seed crystal does not merge with the molten semiconductor to start crystallization. Similarly, at higher melt temperatures, the seed crystal can fully melt away, thereby inhibiting any crystallization. Often a two-color pyrometer focusing on the proximity of seed dip location is used to sense the melt surface temperature (Anttila 2015).

II *Necking*:

With the proper heater power adjustment in place and the seed crystal in contact with the melt surface, a portion of the seed crystal melts to form a meniscus (Müller and Rudolph 2001), and the crystallization starts from the free melt surface. The first stage of crystallization is the growth of a thin neck, usually of diameter ranging from $2\,\mathrm{mm}$ to $4\,\mathrm{mm}$ and lengths up to $30\,\mathrm{mm}$ (Dash 1958). During necking, the growth rate is kept quite high, i.e., with pulling rate up to $6\,\mathrm{mm\,min^{-1}}$ (Friedrich et al. 2015). Throughout the necking stage, the manipulation of the pulling rate and the main heater power provides control of the neck diameter. That is, the increase in pulling speed and the decrease in heater temperature are adjusted pragmatically to produce the neck with the desired diameter. In general, the pulling rate control instantaneously alters the interface geometry to allow for quick diameter adjustments.

Henceforth, the gradual upward pulling of the seed crystal causes the molten silicon to crystallize at the base of the seed. In this way, the pulling mechanism maintains crystallization with the continuous repetition of the crystalline lattice structure as dictated by the seed crystal.

The temperature shock experienced by the seed crystal due to its contact with the hot melt may cause dislocations in the seed lattice structure. The very purpose of growing long necks before the start of the main body is to prevent any dislocations that may otherwise pass on to the crystal body from the seed crystal itself. A specialized necking technique, as devised by Dash in the late 1950s (Dash 1959), relies on the fact that in specific crystallographic orientations, dislocations have limited mobility. Thus, by

incorporating fast pulling and growth rates, the dislocation growth is compelled to the sides of the neck and eventually removed. In this way, after only a few centimeters of neck growth, the dislocations are altogether inhibited. Additional details on the necking phase in general and Dash technique in particular, may be viewed in (Anttila 2015) and (Dash 1958; 1959), respectively. An overview of scientific arguments about the dislocation elimination during the necking phase is given in (Zulehner and Huber 1982). Today Cz is the only method for growing dislocation-free single crystal silicon in very large volumes (Kearns 2019). Further to dislocation rejection, the idea behind growing a small diameter neck offers multiple other benefits such as lesser removal of the latent heat of fusion and reduced exposure to radial temperature gradients.

The length of the neck is usually longer than that required to eliminate the dislocations. Thus, a long neck not only provides additional assurance to the better quality of the material before the start of rather crucial crystal growth stages but serves as a precise measure of the melt temperature to proceed with the *crown* stage of crystal growth. The Cz system has a relatively slower response to the heater temperature changes, however, the right temperature to start with the crown phase should be correct to 1 degree. Therefore, growing a thin, long neck acts as a temperature sensor, which has even better consistency than the pyrometers or other instrumentation, if used instead. Hence, based on the experience, once the neck diameter and average growth rate stay in the prescribed range for a sufficient time, the temperature by then also reaches the right value for the upcoming pulling stage (Anttila 2015).

III *Crown*: The crown growth follows the necking phase. The crown and the subsequent *shoulder* phase are intermediary stages to transition fully from the crystal neck to the main body of the crystal.

During this phase, the diameter should be increased steadily by either decreasing the heater temperature or pulling speed, or both. A rapid increase in diameter alternatively means rapid changes in the process conditions that will, in turn, rapidly alter the shape of the freezing interface leading thereby to a potential structural loss. To put it differently, too slow a pulling speed will result in a flatter crown with the interface shape being convex as contrasted to its tendency as flat or concave shape during the body phase. Large variations in the interface shape, when transitioning from crown to body, may lead to a loss of structure. Conversely, with a slow increase in diameter, the resultant crown is a steeper cone with less effect on the interface shape, thereby allowing smoother transition into the body phase. However, it can be

cost-intensive from a material usage standpoint as well as time-consuming due to extended process duration. Thus, a good compromise on the rate at which diameter shall increase in the crown phase provides not only a success from the structural loss viewpoint but renders both cost-effectiveness and time-efficiency (Javidi 2003, Anttila 2015).

IV *Shoulder*: When transitioning from the *crown* phase to the main body phase, the growing crystal enters a short intermediary phase, termed as the *shoulder phase*. This phase is particularly important to maintain *dislocation-free* growth, before and after transitioning to the body stage (Zhang et al. 2019). This phase usually starts after attaining almost 80% of the required cylindrical body diameter. During this short transitory shoulder phase, a significant rise is applied to the pulling speed, thereby constraining the diameter increase right up to the desired crystal diameter. Eventually, by the end of the shoulder phase, any further rise in the diameter is stopped so that in the subsequent body growth phase, the crystal body grows as a vertical cylinder with a constant diameter Anttila (2015).

The portion of the ingot corresponding to the crown/shoulder phases as well the start of the body (nearby the crystal shoulder) is discarded at the time of wafer slicing because it exhibits nonhomogeneous crystal characteristics due to abruptly varying growth conditions in the transitory stages (Shimura 2017).

Up to the shoulder phase, the crystal growth is performed in an open-loop, i.e., without any feedback for the diameter control, as the camera-based optical imaging system is incapable of continuously tracking a wide range of diametrical changes between the neck and the shoulder stages. The optical imaging system is engaged in the body phase, during which both the crystal ingot and the attached meniscus are well within the camera viewing range.

Moreover, the pulling speed should not be maintained too high further after the shoulder phase to prevent the crystal diameter from growing inwards during body growth.

V *Body*: The part of the produced crystal ingot used for the wafer fabrication is its cylindrical body with constant diameter characterized by the least possible surface striations.

The physical estimate for the crystal radius/diameter comes from the camera-based measurement of the crystal radius that depends on the location of the glowing *bright ring* on the meniscus surface. The bright ring location alters with the curvature of the meniscus surface that in turn depends mainly on the two quantities, i.e., the angle of the melt meniscus at the triple point of the

crystal-melt interface (cf. α_c α_0 in Fig. 2.1) and the height of the meniscus (cf. h_c in Fig. 2.1). Full details of the calculation of this measurement are given in Sect. 5.2.

The conventional control structure used in the body stage is illustrated in Fig. 2.4 and described in detail in Sect. 2.5.3. Basically, the conventional control structure combines the use of the pulling speed for crystal diameter control with the use of the heater power to get the desired growth rate.

Some other controllable parameters along the body length are gas flow, pressure, and the rotation rates of crucible and crystal, to name a few (Anttila 2015). These parameters are usually adjusted apriori for the given crystal configuration.

VI *Tail*: The body stage culminates in the tail stage during which the crystal tail is grown from a small portion of the melt, left in the crucible. At the base of the ingot, the tail resembles an inverted cone with the slant angle ranging from 30° to 40°. Thus, the diameter of the crystal is decreased steadily up to zero such that the ingot no longer touches the melt surface. The formation of the tail prevents any slip dislocations which may otherwise be propagated upwards following a sudden detachment of the body from the melt. Furthermore, such a sudden detachment of the ingot body without proper tail growth causes rapid cooling at the ingot base, which in turn affects the uniform thermal history towards the end of the ingot (Anttila 2015). During the tail phase, the control of diameter is performed in the open-loop because the crystal's cylindrical body blocks any view of the tail by the optical diameter sensing equipment.

2.4 Challenges and Objectives of Czochralski Crystal Growth

The crystal manufacturers have to face a plethora of challenges in a bid to satisfy a range of crystal control objectives/specifications (most often related to quality and efficiency). Due to the coupled nature of the process, combined with the complex heat/mass flow dynamics, the simultaneous fulfillment of multiple control criteria may not be an easy task from a fundamental viewpoint (Duanmu 2006).

2.4.1 Growth challenges related to crystal quality

The requirements on structural perfection of the surface and bulk of single-crystal silicon have continually been on the rise. Apart from the most obvious criterion of

[9] Wikimedia Commons, the free media repository
https://commons.wikimedia.org/wiki/File:Czochralski_Process.svg

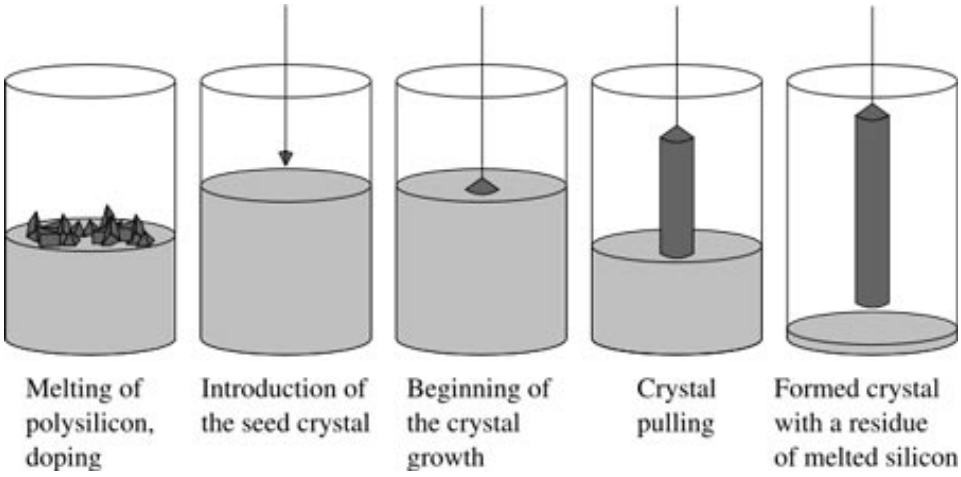

Figure 2.3: The Czochralski growth cycle (source wikimedia.org)[9]

uniform diameter, it is also desirable to have the right amount of dopant concentrations, reduced density of contaminants, and a perfect crystalline structure in the grown crystal. Any undesired drift from a uniform crystallographic orientation, i.e., an imperfection appears in the form of dislocations (aka structural defects or line defects) and other types of defects (explained briefly below) in the finished crystal. It is noteworthy that these imperfections have a profound effect on the characteristics of the material.

From the crystal quality perspective, the frequently encountered challenges related to crystal growth may be characterized under the three broad categories explained briefly below.

I. *Dopants and Impurities*:

The polycrystalline silicon feed material contains contaminants/ impurities that are not desired. Other contaminants come from the hot zone materials, such as oxygen and carbon (cf. *Argon gas flow* in Sect. 2.3.2). Dopants, on the other hand, are the materials that are intentionally added to the molten charge to incorporate electrically active donor or acceptor impurities within the final crystal. Even though the end crystal can never be completely pure, the purity and hence quality of the end crystal can be improved while maintaining the desired concentration of dopants and reduced concentration of undesired contaminants. The impurities can cluster or precipitate and this process leads to structural defects. The latter defects may then act as nucleation sites for further interactions with impurities. An important parameter,

known as the *segregation coefficient*, determines the segregation phenomena occurring at the growth interface. Most metallic impurities in Si have a segregation coefficient of $k \ll 1$, the feedstock is purified upon melting and solidification during the growth process. Doping elements such as boron, phosphorous, and arsenic have segregation coefficients closer to 1. Boron is a very favorable dopant because a k value of 0.8 allows one to obtain very uniform electronic properties throughout the crystal. In the case of oxygen, $k \approx 1$, implies that the oxygen incorporated into the crystal has almost the same concentration as that in the melt.

The higher concentrations of oxygen may lead to higher oxygen precipitate density that can drastically lower the *minority carrier lifetime*[10]. A significant increase in oxygen precipitation is also observed for crystals that are doped heavily with boron, or have high concentrations of metal contaminants. Other factors that influence the concentration of oxygen incorporated into the crystal are the reaction rate of crucible wall dissolution, heat shield design to guide argon flow, melt convection, and the rotation rates of crystal and crucible, to name a few. Therefore, these factors are usually adjusted/tailored by crystal manufacturers to limit the amount of oxygen as per the specifications of wafer users (Friedrich et al. 2015).

II. *Defects*: Even the most perfect, modern, and dislocation-free single crystals of Si are known to possess micro defects (MDs) of various types with dimensions as low as up to nano/micron levels. MDs have deletrious effects on electronic, optical, mechanical and degradation properties of devices made from monocrystalline silicon. One of the most common disorders destroying the characteristic morphology of a regular crystallographic lattice is a point defect at or around the lattice point. Two main types of point defects, frequently encountered in crystal quality resources, are *vacancies* and *interstitials*. A vacancy is marked as the absence of an atom from the grid location (lattice site), while the occupation of an atom at any random open space outside the grid location describes an interstitial defect. Both vacancies and interstitials fall in the *intrisic* defect category, i.e., the defects arising due to the configuration of native atoms. Sometimes the vacancies filled in by impurity atoms, larger than those of bulk atoms, are called *substitutional* defects. Some other higher dimensional defects regarding crystal growth

[10] An important material characteristic that is extremely sensitive to smallest amounts of impurities or intrinsic defects and ideal for inline characterization of material quality and process control. This parameter is essential to assess the performance of many semiconductor devices. The minority carrier lifetime is defined as the average time it takes an excess minority carrier to recombine (Rein 2006, Schroder 2015). The Si wafer has a longer lifetime if the minority carriers persist for a longer duration before recombining, i.e., the flow of electric current can be maintained longer.

are called planar and spatial defects. The most common example of planar defects is *stacking* faults which are caused by the aggregation of interstitials during the cooling of the growing crystal. The conglomeration of point defects leads to spatial defects, e.g., condensation of vacancies results in *microvoids*, while the fusion of interstitials gives rise to *precipitates*. Likewise, the conglomeration of foreign particles results in *inclusions* (Hurle and Rudolph 2004), (Klapper and Rudolph 2015).

The defects in crystal growth are mainly caused by thermal stresses, i.e., the stresses caused by *(a.)* the solidification of melt into a crystal, *(b.)* the temperature variations within the crystal (during production, in particular), and *(c.)* the cooling of the crystal. Therefore, the thermal stresses must be limited to control the defect density within the crystal (Bornside et al. 1990).

In the field of semiconductor growth, defect control engineering is mainly a discipline that encompasses the study of complex phenomena related to concentrations, diffusions, and agglomerations of defects (vacancies/interstitials, etc.), as well as their incorporation into the crystal subjected to crystal solidification, cooling and most importantly the temperature variations in the crystal leading to thermal stresses. These thermal stresses can significantly impact the defect density within the crystal (Bornside et al. 1990).

Some other important findings have had been initiated by Voronkov in the 1980's (Voronkov 1982, Falster and Voronkov 2000, Voronkov 2008). His work suggested that the type and incorporation of point defects within a crystalline structure can be controlled via parameters such as crystal growth rate v_g and the axial temperature gradient G_T near the crystallization front. To summarize, the ratio v_g/G_T must be maintained within 10% of the critical value (Falster and Voronkov 2000) to suppress interstitial and vacancy type micro defects to an extremely low level. Further details can be found in (Klapper and Rudolph 2015).

III. *Dislocations*: Dislocations, aka linear defects, occur along a line around which the atoms of the crystal lattice deviate from the perfect periodic arrangement. In this case, imperfection/distortion, centred along a line, separates two regions of a surface that are themselves perfect but are out of register with each other.

In a Cz growth, four distinctive *ridges* or *habitus lines* are apparent on the shoulder growth. During shoulder and body growth, any variations in the pulling speeds or temperature gradients cause the sizes of these habitus lines to vary. Nevertheless, the presence of these habitus lines and ridges on the crystal body is indicative of dislocation-free single crystal growth (Friedrich et al. 2015).

In a nutshell, the temperature gradient in the growing crystal, which is algebraically proportional to the heat flow conducted by the crystal, has a dominant impact on the crystal quality. Thus, the crystal quality specifications, in terms of virtually zero micro defects, can be expressed implicitly as growing a crystal with stable growth kinetics, i.e., with uniform melt temperature conditions and minimal variations in the shape of the crystallization front (Duanmu 2006, Sinno et al. 2000, Krause et al. 2002). Nevertheless, in an actual scenario, with the ongoing crystal growth, it is quite a challenge to maintain uniform thermal distribution in the vicinity of the crystallization front (interface region), especially in an attempt to overcome the following continuously occurring phenomena that inevitably alter the overall temperature distribution within the process:

- ✓ A continuous drop in the melt level is compensated for by the crucible uplift. Consequently, the exposure of the crucible to the surrounding heaters progressively reduces, thereby markedly altering the temperature distribution within the melt.
- ✓ Secondly, the growing crystal in the centre of the hot zone acts as a cooling fin that removes the heat from the interface through conduction and radiation. In this regard, process variables such as crystal shape, length, and ambient temperature strongly affect the temperature distribution and the heat flow patterns around the interface region (Duanmu 2006).

Both phenomena substantially modify the thermal conditions surrounding the interface region. This can potentially change the balance of heat fluxes about the interface, thereby impacting both the shape of the interface (cf. Fig. 2.1) as well as the quality of the crystal. Hence, from the Cz crystallization viewpoint, the interface shape is a well-founded indicator of the thermal stress levels in the newly grown crystal in the vicinity of the interface. The larger the interface deflections, the larger the radial temperature gradient and consequently greater the possibility of crystal micro-structure distortions. Therefore, the interface shape should be maintained as flat as possible during the entire growth. Conversely, smaller interface deflections ensure uniformly distributed material properties in the radial direction of the sliced wafer. In practice, the interface shape can vary from highly convex to slightly or moderately concave (Brice 1973). Unfortunately, the interface shape cannot be measured directly during the crystallization process. However, from a control design perspective, the assumption of a flat interface cannot be expected to hold if the temperature distribution in the melt and crystal changes significantly during the growth process.

2.4.2 Czochralski growth objectives

As stated earlier, the Czochralski process is the crystal fabrication technique that produces crystals by continuous solidification of the molten Si at the growth/crystallization interface. The shape and quality of the crystal rely heavily on the shape of the crystallization interface and the associated heat and mass transfer across it. Since the crystallization interface, surrounded by the meniscus surface, is a free boundary without any mechanical constriction, therefore material transport across this interface may vary with geometric variations in the interface. This explains the variation between different ingots from the same puller/plant despite the consistent and uniform crystallization technology (Duanmu 2006).

Though there exists a variant of the standard Czochralski crystal growth process, i.e., *the continuous Czochralski*, where the feed of molten Si has to be maintained continuously via a premelter Rea (1979), Wang et al. (1999), the standard configuration of the Czochralski process has a batch nature as it lacks the continuous feed of molten Si. With an ongoing change in the crystal length and melt level within the crucible, the crucible has to be continuously lifted. Therefore, to maintain a constant heat flow into the growth chamber, the heater temperature shall increase steadily. The steady rise in heater temperature causes varying heat transfer phenomena thereby, preventing the system from reaching a constant steady-state which is the characteristic property of a batch process.

The key challenge for batch plants is to consistently manufacture each product in accordance with its specifications while maximizing the utilization of available equipment. Since each batch itself is complete and independent of other batches taking place before or afterward, therefore, the product quality specifications must be ensured in each batch separately.

I. *Diameter control*: Ideally, the crystal ingot during the body phase should resemble as smooth a cylindrical structure as possible. However, in reality, the complex and coupled temperature-driven dynamics cause variations in thermal gradients on the melt side of the freezing interface, thereby causing small striations on the crystal surface. Thus, ensuring the growth of crystal with a virtually uniform cylindrical shape and minimal diameter fluctuations throughout the process growth is the primary objective. An effective diameter control not only minimizes the fluctuations on the lateral surface of the crystal but also economizes the Cz process by minimizing the waste of expensive material during the post grinding of the finished ingot before device fabrication or wafer slicing.

   Close to the freezing interface, if the thermal conditions are balanced at least

on average, the pulling rate is essentially the same as the rate of solidification, thereby making the diameter control realizable (Anttila 2015).

In addition to the increasing requirements for quality and structural perfection of the crystal, the demand for larger diameter crystals is also on a steady rise. One of the prime benefits of utilizing larger crystal diameters in the semiconductor industry is the increased manufacturing economy topped and the improved power gain because larger wafer sizes allow for wafers to be less *pseudo-square* with increased surface area, thereby increasing the capacity to capture light (Chunduri and Schmela 2019). The growth of larger diameter crystals is even more challenging because the growth process gets subjected to batch-related disturbances, which are different both in nature and magnitude when compared to those arising during the growth of smaller diameter crystals. Secondly, due to the revised process objectives, the crystal manufacturers need to adapt the system trajectories and the associated growth parameters with the change in process conditions/interactions. Therefore, in industrial practice, the update of the growth parameters is usually performed empirically (Duanmu 2006).

II. *Growth rate control*: The solidification rate, or simply, the growth rate v_g, represents the rate at which the solid mass of the growing crystal changes. As stated earlier, the growth rate heavily influences the quality of the end crystal, therefore its control is quite essential. Nevertheless, in a conventional control approach (cf. Fig. 2.4), typically used for the Cz growth process, the growth rate control is linked with the temperature dynamics such that the manipulated variable, making use of heater input, has only an indirect effect on the growth dynamics, i.e., via changing the energy balance at the interface. Thus, the heat balance at the interface is critical for growth rate control.

   Ideally, a stationary growth interface with virtually no dynamical variations implies the growth rate to be exactly equal to the pulling rate. In reality, due to the temperature variations at the growth interface, the instantaneous pulling speed may differ from that of the actual growth rate. Therefore, using the heater power Q_H as a manipulated variable for the control of the crystal growth rate is understandable.

   As anticipated from economic considerations, the crystals should preferably be pulled at faster speeds to achieve a higher production rate. However, in the case of larger diameter crystals, factors such as the dissipation of latent heat and the increased thermal stress in the growing crystal, fundamentally limit the pulling rate. Furthermore, with the growth of larger diameter crystals, the combined influence of both reduced pulling rates as well as the

reduced efficiency of radiative heat loss arising from a smaller surface to volume ratio, significantly lowers the rate at which the growing crystal can cool down (Von Ammon et al. 1999).

2.5 Conventional Control Scheme for the Czochralski Process

The choice of a control structure for the Cz system is determined by the physics of the system, choice of system inputs/outputs, their dynamical interactions, the available measurements, and their relationship with the controlled quantity as well as the manipulated variable.

2.5.1 Dominant process physics

The control design of any physical process starts with describing the dominant physics, i.e., the key system interactions in the form of mathematical relationships. In model-based control design, a central problem is to determine the extent to which the mathematical model of a physical system can be simplified without serious compromise on feedback control performance and robustness.

In the Cz process, with relatively complex and coupled process interactions, many researchers have proposed different modeling strategies ranging from black box system identification to complex/coupled partial differential equations that are typically solved using computationally intensive finite element methods (FEM). Despite, providing a deep insight into coupled process interactions, assessing the system's control capability/authority, and revealing the time evolution of system states/variables, the complex FEM models are rarely used for the feedback control. Instead, a less complicated modeling paradigm that encompasses the important system interactions combined with sound empirical knowledge can form the basis for the control system design.

The basic model of the Cz growth process, governing the crystal growth dynamics at the interface and the attached meniscus, is derived from the first principles. The heat released due to solidification determines the rate of crystal growth. Any changes in the growth rate influence the interface thereby causing a change in crystal diameter. Thus, the growth dynamics are strongly correlated with the heat and mass transfer across the meniscus and the crystallization interface. The shapes of the crystallization front and the meniscus play a significant role in crystal growth. Therefore, the variables involved mainly in the crystal solidification from the melt are meniscus height h_c, the radius of the crystallization interface r_c, and the growth angle (cf. angle α_c marked in Fig. 2.1 to represent the extent of taper in the Cz crystal). A manipulated variable that directly influences the process conditions about the crystallization interface is the pulling speed v_p. This qualitative description of

the behaviour of the Cz process is given here to facilitate the understanding of the conventional control structure, shown in Fig. 2.4. Furthermore, the significance of feedforward trajectories, depicted in Fig. 2.4 is explained in Sect. 2.5.3. A mathematical representation on process dynamics is given in Chap. 4.

Another important aspect encountered in modeling for control of the Cz crystal growth is modeling the different modes of heat transfer. The precise modeling of these heat transfers is cumbersome, particularly since the aim is to develop a simplified model suitable for control design.

Due to the high temperatures involved in the growth of Si crystals, radiative heat exchange between the surfaces (delimiting the enclosures of the puller) exposed to these high temperatures is quite dominant. The changing process conditions such as the change in the size of the growing crystal, change in the melt level affect the radiative heat losses between the surfaces of the crystal, melt, crucible wall, and the environment. The two modes governing the heat transfer within the melt are convection and conduction, with the former dominant over the latter. Moreover, the two modes of heat transfer within the melt vary in both temporal and spatial dimensions.

The aim of the modeling in this thesis is to derive a time differential equation of manageable order such that the control design methods may be applied directly. To get around this difficulty, a lumped parameter paradigm is adopted to derive the approximate models of the melt/meniscus lumps, while assuming uniform material and physical properties within each lump.

2.5.2 Available measurements and the choice of manipulated and controlled variables

The two measurements that are commonly used for the control of the Cz process are the crystal radius, indirectly measured via a camera, and heater temperature sensed using a pyrometer. The pyrometer is inserted through a small opening in the containment structure, thereby providing it with a view of the graphite lining surrounding the heater element.

The pulling speed v_p and heater power Q_H are the most commonly employed manipulated/control inputs for the diameter control of the Cz process. If the diameter is to be regulated, an appropriate change in the corresponding pulling speed would be the first strategy or an attempt from the operator. A change in pulling speed influences the crystal diameter by either emitting or absorbing the heat of crystallization (Bukowski 2013). Thus, the mass and energy balance across the growth interface undergoes a change leading to the changes in meniscus height, growth angle, and of course, the crystal diameter.

The thermal balance about the interface that determines the rate of crystallization can be altered through adjustments in heater power. Any changes in heater power propagate through the heater, crucible, and the melt before affecting the interface dynamics. This accounts for the fact that any changes in heat input on the crystal growth rate are noticeable after a significant time lapse.

Firstly, owing to the lag in heat flow from the heater to the interface region, and secondly because changes in pulling speed change the meniscus height immediately, the pulling speed is considered a better actuator for diameter control than the heater power. Conversely, due to desired acceleration constraints and possible speed limits for the pulling speed actuator, the pulling speed shall not be manipulated to an unwieldy extent. A rapid pulling rate stretches the meniscus too much, thereby breaking the meniscus and disconnecting the crystal from its melt. Similarly, a lower pulling speed causes the crystal diameter to increase beyond the set-point value, thereby leading to undesired operating conditions, viz., the solidification of the melt. This undesired increase in the crystal diameter necessitates remelting of the melt that, in turn, can lower the process productivity and efficiency.

If after steady growth rate and proper diameter control, pulling speed deviates from its optimum target level, slower means of control are used, i.e., through adjustments in heater power.

2.5.3 Conventional control structure

Proper control of the meniscus and crystallization interface region is the key for obtaining crystals of well-defined shape. The challenging task in control system design for this process is that the Cz process is a complex process with a combination of both faster as well as slower dynamics.

In conventional Cz control, these different dynamics are accounted for by a cascaded controller structure comprising three control loops: The automatic diameter controller (ADC), the automatic growth rate controller (AGC) and the automatic temperature controller (ATC), respectively (Lee et al. 2005), (cf. Fig. 2.4).

The feedforward reference trajectories, depicted in Fig. 2.4 are also of significant value. Since the changes in pulling speed and the corresponding growth rate can affect the quality of the crystal (Voronkov 2008), therefore the optimal value of growth rate must be chosen carefully. Instead of intuition and experience, the target pulling rate trajectory is designed by considering the dynamic relationship between heater temperature and pulling speed. (Lee et al. 2005)

Furthermore, the disparate time scales are involved in the Cz growth process, viz., the rapid response of pulling speed, and slow response of heater power to the di-

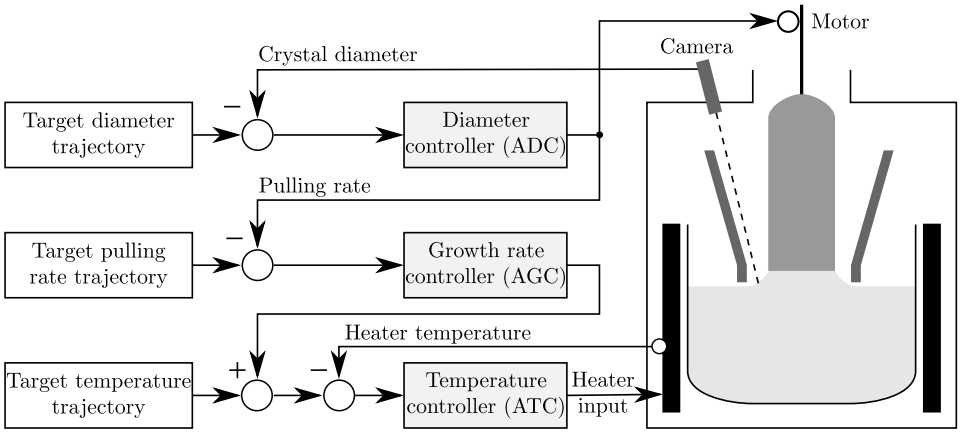

Figure 2.4: Schematics showing a conventional control structure of the Cz system.

ameter adjustment at the freezing interface. Therefore, the empirically derived target temperature trajectory is applied to the temperature controller to account for the anticipative action from rather sluggish heater dynamics (Lee et al. 2005). As reported under the heading *Dislocations* in Sect. 2.4.1, the designed target temperature trajectory follows an increasing trend.

The growth rate controller and the temperature controller, taking measurement from a pyrometer, are connected in cascade. The tracking error for the pulling speed triggers the growth rate controller, which, in turn, adds a trim value to the target temperature trajectory. Due to sluggish dynamics from heater power to crystal growth rate, a time-varying target temperature trajectory is introduced. The intent of introducing the target temperature trajectory is to counteract the factors described above that change the heat transfer characteristics, and thereby, provide anticipative action to reduce variations in the crystal growth rate. A well-designed temperature trajectory implies better tracking of pulling speed and will therefore reduce the contribution from the growth rate controller.

The control system might be extended by the use of a two-colour pyrometer to sense the melt temperature in the vicinity of the seed dipping location. This may provide an intelligent jumpstart for the necking stage (Anttila 2015).

Chapter 3

Literature Survey of Czochralski Modeling, Control and Measurements

This chapter provides a literature review of the Czochralski growth from various aspects such as modeling, control, measurements and the analytical/numerical methods developed to evaluate the shape of the meniscus.

The informed reader may choose to skim/skip this chapter.

In the Cz literature, a myriad of tools and approaches have had been used to model various aspects of crystal growth. These modeling approaches reveal the underlying dominant physics leading, thereby to better insight into the system behaviour. The knowledge of the system behaviour facilitates the process design study as well as the assessment of thermal gradients and stress analysis.

From the viewpoint of system design studies, accurate dynamics of every process component might be very helpful. However, for the control design purpose, approximate system models may suffice while compensating for the lack of accuracy through the feedback control. Therefore, the focus is more on covering the phenomena that are observable online. Still, insights from the detailed models of heat and mass transfers can help determine the objectives of control (such as desired/constant pulling speeds, minimize diameter variations for improved crystal quality, to name a few.)

3.1 Modeling Approaches

To improve the process insight and its design, many researchers in the past came up with complex models of heat and mass transfers within the Cz process. The heat transfers are not only governed by a combination of conduction and convection within the melt and meniscus but by radiative transfers taking place above the melt surface and the puller ambiance. In addition to the heat flow within the melt, when the calculation of radiative heat transfers between various furnace components and the associated view factors are also taken well into account, the models are referred to as global models of heat transfer (Satunkin 1995, Atherton et al. 1987, Dupret et al. 1986; 1990, Bornside et al. 1990, Van den Bogaert and Dupret 1997). The global approach to modeling heat transfer enables accurate prediction of the shape of the melt-crystal interface, the temperature field within the crystal, thereby bringing a better physical insight into the strong coupling between the growth dynamics and the radiative heat transfer (Dupret et al. 1990, Dupret and Van den Bogaert 1994). Furthermore, the effects of changing boundary conditions such as dropping melt level, varying shape of the crystal, interface, and meniscus are also incorporated into these models. This type of modeling leads to fully transient models such that the actual system parameters vary both temporally and spatially. Thus, the mathematical representation of the system is in the form of *coupled partial differential equations*. On the positive side, these detailed models play a significant role in understanding the underlying effects of heat transport and capillarity to improve system design and operation. However, on the negative side, they are computationally intensive to run in real-time, thereby making them unsuitable for direct use in control, like in MPC. They may be used as a starting point for simpler models (e.g., fitting a curve for the heat flux into the crystal, or getting a frequency response from an FEM model - even though this would be computationally demanding). Moreover, there is the difficulty of updating a very detailed model in real-time from the very few measurements available online.

Since the Cz system never reaches steady-state operating conditions due to batch-type and concomitant thermal variations, therefore the disparate time scales have been used to the advantage of simplifying the fully transient models. That is, in comparison to a much longer duration of the complete crystal growth, the time scales for achieving thermal equilibrium of the system are relatively small. Therefore, instead of a fully transient system, the Cz growth can be simplified by assuming the system as comprising a series of quasi-steady-states (Derby et al. 1985, Derby and Brown 1986a;b; 1987, Atherton et al. 1987). In this approach, a sequence of steady-state solutions is used to form the feedforward trajectory. The great advantage of these approaches is the fact that the heat flow in the plant can be modeled quite accurately. On the other hand, much effort is required to adapt

the models to the actual plant design and to determine the physical parameters needed in the model with sufficient accuracy (Winkler et al. 2010c).

Contrary to the quasi-steady-state approach, A. Raufeisen *et al.* introduced a novel algorithm to calculate the transient behaviour (non-stationary) of the crystallization interface, including the movement of the three-phase boundary and the free melt surface. Their work comprised of performing three-dimensional simulations (Raufeisen et al. 2009; 2010; 2011). Sabanskis *et al.* employed two-dimensional simulation to model the transient behaviour of the three-phase boundary movement, thereby reducing the computational cost (Sabanskis et al. 2013).

Due to the complex and coupled dynamics of the Cz process, detailed modeling of various physical phenomena on the full process scale is quite cumbersome and not very relevant to the control design strategy. Therefore, several types of simplified models have been investigated for control design. Some of them have been based upon simulating the flow of the melt bulk, restricting the calculations to the melt only, and assuming a flat solidification interface. Such models are also known as local integrated thermal capillary models where the radiative heat transfers (Derby et al. 1985, Derby and Brown 1986a;b; 1987) and moving boundary conditions are neglected.

For perfecting the Cz technology, the model-based approaches for the control of the Cz process have been actively pursued by the research community to date. The control engineers simplify the mathematical description of the complex Cz process by partitioning the system into lumps or domains. Within each domain, the material properties are considered to be homogeneous, i.e., without any spatial or time dependence, thereby resulting in a set of *ordinary differential equations*.

The pioneering work on modeling the Cz process that formed the basis for closed-loop control design was presented by (Steel and Hill 1975). While considering balanced heat conditions in the vicinity of the growth interface, they derived the transfer function between crystal radius and heater power by linearizing the system around steady-state growth conditions. They also reported that the dynamics of heat transfer to the interface represent a significant lag in the overall transfer function.

In an attempt to understand the relations between the dynamics related to the desired control objectives, measurements, inputs, and disturbances, Gevelber *et al.* developed a low-order process model. The model captured the major dynamics but also took into account the couplings between different components of the system as well as the effects of dominant disturbances for improved control system design. The distributed nature of the process was simplified via averaging over the

spatial domain. Through linearization of the lumped parameter model about the growth trajectory, the overall eigen structure was determined to investigate system stability, transient response characteristics, and the coupled nature of the system (Gevelber and Stephanopoulos 1987).

During the same period, low-order models of the Cz process in state-space form were developed by other researchers, of whom the works of Hurle *et al.* and Satunkin are quite salient. Hurle *et al.* investigated the dynamic relationship between heater power and crystal diameter/weight through experimental techniques (Hurle et al. 1986) as well as by developing approximate analytical models and numerical simulations (Hurle et al. 1990). Satunkin (1995) proposed the lumped parameter approach in state-space form. He also investigated the Cz process from various aspects such as the analysis of steady-state conditions for Cz lumped dynamics, determination of parameters for digital control design, and digital filtering of the measurement noise (Satunkin 2010).

Continuing Gevelber's work, Duanmu formulated a lumped model while taking into account the commercial-scale equipment configurations. Moreover, the radiation heat transfer is studied while considering the real process scale and the effects of both crystal shape as well as the changing crucible and melt levels (Duanmu 2006).

In an attempt to improve the dynamical characterization of the Cz system as well as to facilitate the prediction of crystal radius dynamics due to changing heater power and pulling speed levels, Park *et al.* presented their study on a dynamical model of the ingot diameter elaborating the detailed computation of two types of heat transfer mechanisms, both radiative and conductive. The total radiative heat transfer between various surfaces was calculated by dividing each candidate surface into smaller fragments and summing up the radiated energy from each surface based on the respective view factor calculation. Based on the principle of energy balance, the conductive heat transfer is determined between the graphite susceptor and the quartz crucible, between the quartz crucible and the melt, and between the melt and the crystal. From the simulation results, they claimed their modeling strategy to be in good accordance with the actual process trends (Park et al. 2008).

The basic model representing the crystal growth at the crystal-melt interface (i.e., relating the pulling speed with the variation in meniscus height, crystal radius, and growth angle) has been used consistently in a variety of control approaches. All the modeling approaches listed above have only been used in simulation studies.

3.2 Control Approaches

In the following, the reader will be provided with an overview of various control strategies proposed for control of the Cz process. Except for a few publications, a majority of the publications do not report any results from testing and validation on the actual process. It is unclear whether this is due to commercial secrecy, the costs of implementing on and experimenting with an actual industrial process, or for some other reasons.

Gevelber and associates (Gevelber et al. 1988, Gevelber 1994a;b, Gevelber et al. 2001) have proposed multiloop control structures to mitigate batch disturbances and the coupling among different system parameters. The proposed schemes, though interesting, are quite complex and require the use of an additional set of actuators. Therefore, to the knowledge of this author, the presented control configurations have not found industrial use.

Irizarry-Rivera and Seider (1997a;b) presented a control approach based on two MPC controllers operating on different length and time scales. A capillary MPC controller controls the crystal radius by using pulling speed as a manipulating variable, while the bulk MPC controller manipulates the heater inputs. They tested their control scheme on the Cz model and presented the corresponding simulation results.

Bandoh et al. (2008) presented their experimental results on the application of a sliding mode controller with a nonlinear state predictor to a complex Cz process.

Lee et al. (2005) introduced a scheme for the design of heater setpoint trajectory based on model predictive control (MPC). The complex dynamic effect of the heater temperature on the pulling speed is incorporated into the temperature trajectory design quantitatively. Their method demonstrated promising results when validated on industrial systems. As their approach didn't utilize any feedback, therefore, a similar approach may be used in conjunction with the model-based control without needing to model the thermal part explicitly.

Winkler *et al.* presented the nonlinear model-based control of the Cz process. Their first article was focused mainly on using a less complicated model of the Cz process encompassing only those parts of the process dynamics for which both the structure as well as the parameters were known with sufficient accuracy. To compensate for the missing thermal dynamics, the conventional PID controller was used in conjunction with the model-based control that covers the hydrodynamical-geometrical aspect of the Cz dynamics (Winkler et al. 2010a). In the subsequent articles, they presented the development of a nonlinear observer for the estimation of crystal radius and growth rate. They also performed thorough investigations

into the robustness capability of the designed observer through both the simulations and experiments. Furthermore, they introduced the concept of material and process-specific properties for the scheduling of PI controllers that result in a better system performance overall (Winkler et al. 2010b, Neubert and Winkler 2012). In the last of the article series, they presented the design of a feedforward control for both pulling speed and heater temperature. Despite the lack of thermal dynamics, they designed the associated feedforward control using a qualitative approach to model the relative changes between the manipulated and the controlled variables (Neubert and Winkler 2014).

Winkler and associates demonstrated their scheme in a laboratory setup for the growth runs of GaAs, InP and Ge. Their scheme, however, didn't work for Si that has material characteristics different from those of compound semiconductors mentioned above.

Ng et al. (2011) presented an MPC formulation, based on a discrete-time model of the Cz growth system.

Abdollahi et al. (2014) published their work on diameter control in conjunction with reference temperature tracking based on an FEM model of heat transfer in the Cz growth process. Starting with a predefined/desired crystal shape, an optimized reference temperature trajectory is synthesized using a coarse mesh FEM model. Next, this optimized reference temperature trajectory is utilized for model predictive-based temperature tracking using a refined FEM model that takes into account actual crystal geometry subjected to growth rate disturbances due to variations in the thermal field.

A predesigned feedforward temperature trajectory should be updated periodically to account for any material deteriorations leading to discrepancies in the Cz plant operation. For this purpose, Wei et al. (2015) presented an online trimming technique for the feedforward trajectory. An MPC technique is used to update the feedforward trajectory, i.e., any deviation between the actual pulling speed and the growth rate will trigger a counteracting offset by the MPC controller.

Rahmanpour et al. (2017) have proposed the development of run-to-run supervisory control of the Cz batch process. Their work comprised of reduced-order model of the Cz growth process followed by the measurements/estimations of essential system parameters and the design of two nonlinear MPC controllers to accomplish an improved prediction of system states, parameters, and overall operation from the previous run to the next run (Rahmanpour 2017).

Recently, Liu et al. (2020) have proposed and implemented a new control structure, based on GPC (generalized predictive control) – a special class of MPC. While

maintaining constant pulling speed, the temperature of the thermal field serves as a control variable. The model between diameter and temperature, containing nonlinearities and time delays, is obtained by training neural networks with deep learning methods such as SSAE (stacked sparse autoencoder). Thus, the identified SSAE function is utilized further as a prediction model in GPC (Generalized Predictive Control).

Though several methods have been proposed so far, however, none has tackled the control limitation due to non-minimum phase behaviour. Furthermore, most of the approaches presented above are complex and can be expected to be costly to implement and maintain, as well as being challenging to understand for plant operators. The control methodology proposed in this thesis aims at bridging this gap with a solution that can be implemented with only minor modifications to the existing industrial control scheme, as shown in Fig. 2.4.

3.3 Estimation of the Shape of the Meniscus

For the Cz crystal growth process, an important phenomenon that takes place right after the dipping of seed crystal into the molten Si is the formation of the meniscus (cf. Fig. 2.1). This very phenomenon, often termed as the *capillarity* phenomenon occurs as a result of intermolecular forces between the Si melt and the Si crystal in the centre. The study of this phenomenon and its effects is of fundamental importance for understanding the Cz growth dynamics at the interface, viz., how the variations in the shape of the meniscus affect the crystal diameter.

From the author's perspective, one of the most comprehensive resources on the phenomenon of capillarity is the multi-author book compiled by Thiery Duffar. One complete chapter (Braescu et al. 2010) is dedicated to the meniscus formation, its various mathematical representations, and detailed approaches to numerical solutions as well as the analytical approximations.

Pioneering work on the shape of the meniscus is attributed to the two mathematicians *Thomas Young* and *Pierre-Simon Laplace*. As a continuation to the qualitative work of Young, who defined the concept of mean curvature for a free surface, Laplace presented the first formal analytical expression of the free meniscus surface shape. The mean curvature is defined as ($\kappa = 1/R_1 + 1/R_2$), where R_1 and R_2 are the principal radii of curvature. At any point on a curve, the principal radii of curvature are defined as the radii of osculating circles approximating the curvature in two mutually orthogonal directions. R_2 defines the radius of curvature in a plane parallel to the plane of paper and R_1 represents the radius in an orthogonal plane (cf. Fig. 3.1). Laplace showed that the mean curvature of the free surface is proportional to the pressure change (ΔP) across the surface.

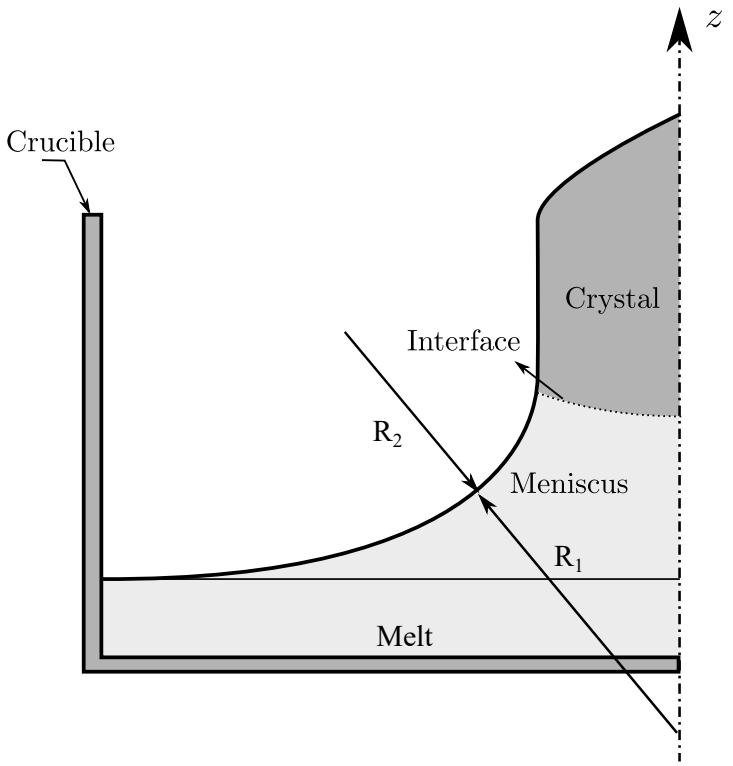

Figure 3.1: Principal radii of curvature

Applying the concept of mean curvature to the Cz meniscus, while neglecting the effects of melt rotation and magnetic induction, a simplified expression for the *Young-Laplace equation*, applicable to the Cz system is given by (Tatartchenko 2010, Braescu et al. 2010),

$$\sigma_{lv}\left(\frac{1}{R_1}+\frac{1}{R_2}\right) = -(\Delta P - \rho_l g z), \tag{3.1}$$

where σ_{lv} is the proportionality constant representing the effect of surface tension between liquid and vapour phases. The pressure difference, given by $\Delta P = p_l - p_v$ is constant for a given height above the flat melt surface, where p_l is the internal liquid pressure determined with reference to the origin, p_v is the pressure exerted by the gas surrounding the melt, and $\rho_l g z$ is the hydrostatic pressure. The value of ΔP depends on the choice of the origin of z-coordinate. The value of ΔP is zero when the axial (vertical) coordinate $z = 0$ lies on the plane of the flat melt surface (Tatartchenko 2010). The physical quantities making up the hydrostatic pressure are z, the vertical distance above the flat melt surface, g, the acceleration due to gravity, and ρ_l is the melt density.

Due to rotational symmetry, the meniscus is an axisymmetric surface, i.e., $z = z(r)$ with r as a radial cordinate and z as an axial coordinate. Therefore, the principal radii of curvature in (3.1) can be expressed in terms of differential geometry as:

$$\frac{1}{R_1} = \frac{\mathrm{d}^2 z/\mathrm{d}r^2}{\left[1 + (\mathrm{d}z/\mathrm{d}r)^2\right]^{3/2}}$$
$$\frac{1}{R_2} = \frac{\mathrm{d}z/\mathrm{d}r}{r\left[1 + (\mathrm{d}z/\mathrm{d}r)^2\right]^{1/2}}$$

Thus, the expression (3.1) can be rewritten as:

$$\frac{\mathrm{d}^2 z/\mathrm{d}r^2}{\left[1 + (\mathrm{d}z/\mathrm{d}r)^2\right]^{3/2}} + \frac{\mathrm{d}z/\mathrm{d}r}{r\left[1 + (\mathrm{d}z/\mathrm{d}r)^2\right]^{1/2}} = -\left(\frac{\Delta P}{\sigma_{lv}} - \frac{\rho_l g z}{\sigma_{lv}}\right) \tag{3.2}$$

The expression (3.2) can be converted into a non-dimensional form by considering the dimensionless variables as $\bar{r} = r/a$, $\bar{z} = z/a$. These dimensionless variables, in turn, define the slopes of meniscus profile as $\mathrm{d}z/\mathrm{d}r = \mathrm{d}\bar{z}/\mathrm{d}\bar{r}$ and $\mathrm{d}^2 z/\mathrm{d}r^2 = a\,\mathrm{d}^2\bar{z}/\mathrm{d}\bar{r}^2$. The *capillary constant*, denoted by the symbol a, is defined as $a = \sqrt{2\sigma_{lv}/\rho_l g}$. Consequently, the expression (3.2) in non-dimensional form is given by (Huh and Scriven 1969)

$$\frac{\mathrm{d}^2 \bar{z}/\mathrm{d}\bar{r}^2}{\left[1 + (\mathrm{d}\bar{z}/\mathrm{d}\bar{r})^2\right]^{3/2}} + \frac{\mathrm{d}\bar{z}/\mathrm{d}\bar{r}}{\bar{r}\left[1 + (\mathrm{d}\bar{z}/\mathrm{d}\bar{r})^2\right]^{1/2}} = -\left(\frac{\Delta P\, a}{\sigma_{lv}} - 2\bar{z}\right). \tag{3.3}$$

The above expression (3.3) may either be solved as an initial value problem (IVP) or boundary value problem (BVP), depending on the configuration or the solution domain. Two approaches that are commonly used regarding the solution of (3.3) are converting the given second-order system into either a set of 2 or 3 linear differential equations. For the solution of (3.3), Princen and Mason introduced the concept of arc length s along a generating curve of the surface of revolution (Princen and Mason 1965a;b). Fig. 3.2 illustrates a segment of meniscus with small differential arc length $\mathrm{d}s$ and the angle of inclination ϕ. Thus, the arc length s, combined with the parameter $\phi = (\pi/2 - (\alpha_0 + \alpha_c))$ (cf. Fig. 2.1) results in the following set of three first-order parametric equations expressed in s as:

$$\begin{aligned}
\frac{\mathrm{d}\bar{r}}{\mathrm{d}s} &= \cos(\phi) \\
\frac{\mathrm{d}\bar{z}}{\mathrm{d}s} &= -\sin(\phi) \\
\frac{\mathrm{d}\phi}{\mathrm{d}s} &= \frac{\mathrm{d}\phi}{\mathrm{d}\bar{r}} \cdot \frac{\mathrm{d}\bar{r}}{\mathrm{d}s} \\
&= -\frac{\sin(\phi)}{\bar{r}} + \left(\frac{\Delta P\, a}{\sigma_{lv}} - 2\bar{z}\right)
\end{aligned} \tag{3.4}$$

In the above set of mathematical relationships, the last expression is obtained by substituting $\mathrm{d}\bar{z}/\mathrm{d}\bar{r} = -\tan\phi$, and $\mathrm{d}^2\bar{z}/\mathrm{d}\bar{r}^2 = -\sec^2\phi(\mathrm{d}\phi/\mathrm{d}\bar{r})$ in (3.3).

Later, Huh and Scriven eliminated the arc length s and transformed the original second-order differential equation (3.3) into a set of two first-order differential equations (Huh and Scriven 1969) given as:

$$\begin{aligned} \frac{\mathrm{d}\bar{z}}{\mathrm{d}\bar{r}} &= -\tan(\phi) \\ \frac{\mathrm{d}\phi}{\mathrm{d}\bar{r}} &= \left(\frac{\Delta P\, a}{\sigma_{lv}} - 2\bar{z}\right)\sec(\phi) - \frac{1}{\bar{r}}\tan(\phi) \end{aligned} \tag{3.5}$$

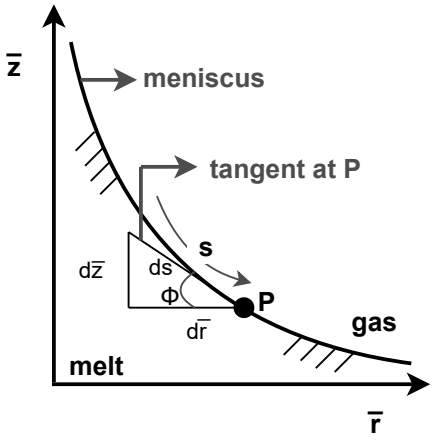

Figure 3.2: Segment of meniscus illustrating arc length s and parameter ϕ representing the meniscus inclination

With the aid of efficient computer algorithms, numerical tools and the knowledge of initial and boundary conditions, such as $z|_{r=r_c} = h_c$; $\mathrm{d}z/\mathrm{d}r|_{r=r_c} = -\tan(\phi)$ and $z|_{r\to\infty} = 0$, the second-order ODE (3.2) can be solved to obtain the desired meniscus shape $\bar{z}(\bar{r})$ for a given Cz system configuration (Huh and Scriven 1969, Tatartchenko 2010). It is noteworthy that to produce a crystal of given radius r_c, the initial height of the meniscus h_c at the interface is unknown. Furthermore, the last boundary condition corresponds to a meniscus that becomes effectively flat, when extended farther away from the crystal. Thus, a meniscus may be regarded as unbounded (Huh and Scriven 1969). For this rather bizarre boundary condition, i.e., no meniscus curvature at $r \to \infty$, many researchers came up with a number of analytical approximations given below:

I *Approximation of Tsivinski*: The approximation of Tsivinski (Tsivinskii 1962) for the estimate of meniscus height as described by (Duffar 2010) is given

by

$$h_c = a\sqrt{(1-\cos\phi) + \left(\frac{a^2\,\sin\phi}{4\,r_c}\right)^2} - \frac{a^2}{4\,r_c}\sin\phi \tag{3.6}$$

where a as explained earlier is the capillary length often termed as *Laplace constant*. This approximation has frequently been used for height estimation in diameter control techniques as well as for derivation and comparison with other numerical/analytical solutions of meniscus shape (Braescu et al. 2010).

II *Approximation by Hurle*: The meniscus profile approximation as defined by Hurle in (Hurle 1983) expresses the horizontal position of meniscus surface relative to crystal radius r_c as:

$$\begin{aligned} r(h_c, r_c, z) = r_c &+ \sqrt{\frac{2}{A} - h_c^2} - \sqrt{\frac{2}{A} - z^2} \\ &- \frac{1}{\sqrt{2A}} \cdot \ln\left[\frac{z}{h_c} \cdot \frac{\sqrt{2} + \sqrt{2 - Ah_c^2}}{\sqrt{2} + \sqrt{2 - Az^2}}\right] \end{aligned} \tag{3.7}$$

where A is given as:

$$A = \frac{1}{2}\left[\frac{\sin\phi}{r_c h_c} + \frac{2}{a^2}\right]$$

III *Approximations based on Bessel Functions*:

Few analytical solutions, for the axisymmetric *Young-Laplace* equation, are based on the use of Bessel functions (Boucher and Jones 1980, Johansen 1992; 1994). The most widely used estimate, derived by Boucher and Jones (1980), algebraically relates the crystal radius r_c and slope angle $\alpha_c := \alpha - \alpha_o$ with the meniscus height h_c as shown in (3.8).

$$h_c = a\sqrt{\frac{1-\cos(\phi)}{1 + \frac{a}{\sqrt{2}r_c}}} \tag{3.8}$$

An advantage of approximation due to Boucher and Jones is the fact that it can be explicitly solved for α_c. The expression (3.8) relates all three essential growth parameters h_c, $\alpha_c = (\pi/2 - \phi - \alpha_0)$ and r_c at the three-phase boundary.

However, based on a comparison with numerical calculations, an approximate analytical meniscus relation $h_c = h_c(r_c, \alpha_c)$ due to Boucher and Jones is modified by (Johansen 1994). The modified relation significantly

improves the overall agreement over a wide range of r and α relevant for Czochralski growth. This modified meniscus expression is given by

$$h_c = a\sqrt{\frac{1-\cos(\phi)}{1+0.6915(r_c/a)^{-1.1}}}. \tag{3.9}$$

To get around the difficulty posed by the boundary condition $z|_{r\to\infty} = 0$, many researchers prefer the analytical approximations over the numerical solutions. However, Mika *et al.* presented a fusion of both analytical and numerical solutions to determine the shape of the meniscus (Mika and Uelhoff 1975). They divided the solution space into two segments, where the asymptotic part $r \in [r^*, \infty)$ was solved using modified Bessel functions, while the remaining initial part was solved using the Runge-Kutta method on the finite range $r \in (r_c, r^*]$ (Braescu et al. 2010).

3.4 Measurements Proposed for the Cz Process

Though the industrialization of the Czochralski crystal pulling process is long-established, the sensing equipment and techniques used in the present state-of-the-art Czochralski pullers are still fundamentally similar to those of the traditional methods. As reported by the U.S. Department of Energy, one of the earlier developments of crystal pulling equipment from Kayex Corporation Rochester, New York, included sensors for determining the melt level, melt temperature, and crystal diameter (Lane 1981). Several approaches/methods were proposed and materialized at that time (almost four decades ago), and with slight modifications, these are invariably the approaches practiced in the Cz growth today. Nevertheless, the production of equipment used in most modern Cz pullers has undergone significant improvements due to a better choice of materials and improved manufacturing techniques.

This section presents a brief overview of the sensing equipment and the associated measurement/estimation techniques employed in the Cz growth system.

A traditional technique of crystal weighing-based diameter measurement for shaped crystal growth was pioneered in patents by Levinson (1959) and Rummel (1966). During the 70s, Bardsley *et al.* employed the weight measurement for the Cz diameter control based on the lumped parameter model of the Cz process. From the automatic diameter control viewpoint, they used the error signal arising from the deviation in the expected crystal weight measurement, as an input to the servo control loop acting upon heater power to the melt (Bardsley et al. 1972; 1974a;b; 1977a;b). An industrial load/weighing cell that suspends the pulling rod was used for the weight measurement. The force experienced by the weighing cell comprises not only the static weight of pulling rod and crystal but also has contributions

arising from the surface tension of the melt and the the hydrostatic head of liquid in the meniscus supported by the growing crystal. This weighing signal, as reported by Bardsley et al. (1977a), exhibits a behaviour associated with the growth of semiconducting materials, i.e., materials with characteristic solid-state density lower than that of the liquid state. Furthermore, the melts of these materials do not completely wet their solids and have therefore nonzero contact angles between the crystals and their respective melts. A comprehensive mathematical description of these issues can be found in (Bardsley et al. 1974a; 1977a). They found that an increase in crystal diameter resulting from a change in heater power resulted in an initial decrease in the height and volume of the attached meniscus. Consequently, the weight signal indicated false diminution (*anomalous behaviour* as discussed before) in the beginning despite the increasing trend of actual diameter.

Similar reasoning can be presented on the basis of the fact that Si has nonzero contact angle, i.e., it cannot be completely wet by its own melt. Therefore, any increase in crystal radius leads to the reduction in the vertical component of the surface tension acting on the crystal (Winkler and Neubert 2015). Based on the mathematical expression of the total force acting upon the pulling rod due to melt mass and crystal (cf. an expression that depends on the vertical component of surface tension (Bardsley et al. 1974a, Winkler et al. 2010c)), the fallacious reduction in total force due to melt mass and crystal is observed which can lead to reduction in the overall weight gain signal.

Hurle et al. (1986) claim to be the first to determine the transfer function between heater power input and differential crystal weight output. They based their work on system identification. Though this technique may apply to a wide range of crystal materials and growth techniques, however, the accuracy of the model significantly depends on the level to which the system dynamics are excited in the identification experiment. An important finding of the work by Hurle et al. (1986), based on the Cz growth of germanium crystals, was detecting the presence of anomalous behaviour in the obtained transfer function, i.e., the presence of RHP zeros.

Gevelber and Stephanopoulos (1987), Gevelber et al. (1988), Gevelber (1994a) had observed a similar anomalous behaviour in the weight signal transfer function due to the presence of RHP zero. This anomalous behaviour is indicated by the initial response of meniscus height opposite to its steady-state response, when subjected to a step increase in heater power.

The weight measurement in the industry is also fundamentally limited by the growth of larger diameter crystals because, with larger diameters, the force on the load cell also increases that in turn calls for load cells with larger capacity. On the contrary, load cells with larger nominal capacity have reduced absolute resolution

for smaller loads (Winkler and Neubert 2015).

In 1967, Patzner et al. (1967) came up with the first reported operational automatic diameter control. They used a signal from a photovoltaic optical pyrometer, focused on the melt surface adjacent to the growing crystal, to sense the radiation propagating from the melt. Dessauer et al. (1970) extended the use of sensed radiation to serve as a means for adjusting the growth conditions of the crystal by means of adjusting the crystal pulling mechanism, the crucible lift mechanism, the crucible rotation rate, or combinations of these mechanisms. A similar measurement technique has also been employed by Domey (1971) for the computer control of the Cz process using the modulation of heater power and pulling rate. Gross and Kersten (1972) and Lorenzini et al. (1974) incorporated optical measurement of crystal shape for growth control applications of different crystals. The meniscus reflection has also been used by Turovski *et al.* in their work, reported in 1977.

For quite some time, many researchers associated the formation of the bright ring with the evolution of latent heat of solidification from the growing crystal into the meniscus (Patzner et al. 1967, Domey 1971, Lorenzini et al. 1974). Digges et al. (1975) proved this hypothesis wrong because the flow of heat from crystal to melt implies supercooled melt that is quite unrealistic. Moreover, the brightness on the meniscus is visible for crystals with slower growth rates resulting in smaller heats of fusion. In an extreme situation, even when the crystal growth gets halted, these brightness patterns on the meniscus are still apparent. He also identified that the bright ring formation is attributed to the reflection by the meniscus of light emitted from the hot zone assemblies. For better diameter estimation based on light reflected from the meniscus, there are certain material characteristics that play an important role in this regard. Firstly, the height of the meniscus and the curvature of the meniscus are strongly related to material characteristics such as its density and surface tension, as follows from the Young-Laplace equation (cf. (3.1)). Moreover, the material clearly has to be reflective. Silicon qualifies as a suitable material for the optical diameter sensing owing to its high value of capillary constant (i.e., modestly large surface tension and low density resulting in large meniscus heights) and metallic reflectivity (Digges et al. 1975).

To the author's knowledge, the anomalous behaviour in the bright ring-based radius measurement signal has not been explained in much detail before.

As stated earlier, there is no direct measurement of the melt temperature. The only temperature measurement used widely in the industry is with the pyrometer inserted through a hole from the containment exterior to the graphite lining surrounding the heater. This method provides a crude estimate for the heater temperature. Moreover, the sluggish temperature dynamics of the Cz system mar the

value of the temperature feedback because of the delays introduced between the melt temperature and the measured temperature. Silicon is indeed a difficult material when it comes to non-contact temperature measurements. Nevertheless, the real-time monitoring of the silicon melt temperature may help improve the growth regime because the melt temperature can directly influence the growth rate (Rahmanpour 2017).

In this regard, many researchers proposed the use of thermocouples to determine thermal gradients at the crystallization interface. Due to the strong reactive nature of molten Si, almost all the schemes making use of thermocouples need this sensor to be enclosed in a thin quartz glass capillary tube. Although thermocouples have not found use in the regular production of Si ingots in the industry (owing to the high reactivity of Si), their use has nevertheless provided significant insight in experimental studies.

Kuroda *et al.* pioneered research on the use of thermocouples at Hitachi Ltd. research laboratories (Kuroda 1983), (Kuroda and Kozuka 1983), (Kuroda et al. 1984). The use of thermocouples in their research has proven highly advantageous for studying the effects of temperature gradients and oscillations on the Cz growth process, particularly concerning the density and distribution of micro defects in the growing crystal. By now it is well known that the quality of the crystal in terms of the density of micro defects improves with the decrease of thermal oscillations which will also reduce diameter oscillations. This insight originally came from the studies by Kuroda *et al.*

Dornberger et al. (1997) performed experimental validation of numerically calculated temperature distributions within the industrial silicon Czochralski puller. Their validation method also made use of thermocouples for temperature sensing in the crystal as well as inside the lateral and bottom insulations. They claimed that the advanced simulation methods are verifiable as being capable of handling complex heat transfers similar to those encountered in the actual Czochralski silicon growth furnaces, except for the melt convection problem, which is not solved satisfactorily as of yet.

Huang et al. (2001) also proposed the use of a differential type thermocouple with quartz capillary to measure the temperature gradient in Cz Si crystal growth. The two junctions of a differential thermocouple provide a measure of temperature difference between the two junctions. They also verified their measured value of thermal gradients with the energy balance at the interface[1].

[1]The energy balance connects the thermal gradients on both sides of the interface, the crystal growth rate and the latent heat of solidification (cf. (4.1e) in Sect. 4.1).

Komperød et al. (2011) presented a study with a little more focus on the instrumentation. They designed a sensor fusion algorithm to merge the signals of two pyrometers, one measuring heater temperature and the other measuring the melt temperature, in order to give an estimate of the melt temperature. Their algorithms were based on a dynamic model and two complementary filters. The algorithm worked well within a limited temperature range. However, to handle larger temperature variations, more research is needed to understand and incorporate the nonlinear temperature dynamics into the process model used for sensor fusion.

At the start of the seed dip to commence the neck stage, a pyrometer can be useful for sensing the melt temperature. A good dipping is essential to the success of the neck stage of the process (Anttila 2015). Phuc et al. (2019) have recently devised an automated scheme based on artificial intelligence (AI) to identify those scenarios captured by camera images that correspond to dipping a seed at the right temperature, also referred to as good seed dipping. They also determined the duration up to which a good seed dipping scenario lasts. The approach seems advantageous in the industry where less/no operator intervention is required to switch the process automatically from dipping to the necking phase.

Chapter 4

Mathematical Description of Czochralski Process

This chapter describes the mathematical model of the Cz process used in subsequent chapters of this thesis. The model can be decomposed into a hydrodynamic part and a thermal part, the hydrodynamic part is described before the thermal part. The hydrodynamical model sets up a baseline for performing a 3D ray-tracing simulation and the study of associated anomaly in the bright ring radius measurement (cf. Chap. 5). The thermal part provides an approximate (qualitative) model for the flow of heat from heaters to the crystallization interface and into the crystal. Although the model for the flow of heat into the crystal is very rough but this model is used to check the robustness of the crystal radius controller designed in Chap. 6, when faced with temperature disturbances.

This chapter is partly based on the work presented in Bukhari et al. (2021a), in which the modeling work starts from models previously published, most notably (Winkler et al. 2010a) and (Rahmanpour 2017).

From the perspective of control system design, the mathematical model of the Czochralski process comprises two main components. The first component is the basic crystal growth dynamics at the interface, explained in detail in Sect. 4.1, while the second component is the heater/temperature dynamics that qualitatively simplify heat transfers from heaters to the melt, melt to the crystal, and eventually to the crystal ambiance. The dynamics of the heater itself is not much in focus but rather the temperature dynamics of the whole puller are of interest.

An accurate model of the thermal dynamics would require expressing the heat-related phenomena as a system of nonlinearly coupled partial differential equations

(PDE) defined on varying time and spatial scales (Dreyer et al. 2012), followed by discretizing these PDEs on a fine grid/mesh to result in a set of high-order ordinary differential equations. Temperature dynamics have a significant impact on the outcome of the system. Specifically, the crystal growth rate, denoted by v_g, is a result of the thermal situation at the interface.

While such a model may be appropriate for process design studies, it is commonly considered way too intensive computationally, and hence impractical for use in control design studies. Therefore, in Sect. 4.2, a simplified model based on a coarse lumped model assumption is developed. The basics of this model have been adapted from the model presented in (Rahmanpour 2017).

While the heat transport from heaters to melt is quite slow and therefore is of little importance for the investigation of an anomaly in the bright ring measurement and its mitigation via control, it is central while evaluating the control performance in a qualitatively reasonable manner. Therefore, the reader may skim the section of temperature dynamics, i.e., Sect. 4.2 until the last chapter, where the performance of the closed-loop system with the designed compensator and controller, is evaluated.

4.1 Crystal Growth Dynamics

The modeling in this dissertation primarily aims at the investigation and mitigation of anomalous behaviour in the crystal radius measurement/estimation signal. Through understanding of the anomaly in the radius measurement opens an opportunity for achieving better control of the Cz process, as will be shown in subsequent chapters.

During crystallization, a change of phase from the molten silicon to solid crystal occurs continuously at the crystallization interface. The standard Cz growth model, commonly referred to as hydrodynamical/geometrical (Winkler et al. 2010a) model defining the crystal growth dynamics at the crystal-melt solidification interface (cf. Fig. 2.1) is given by,

$$\dot{r}_c = v_g \tan(\alpha_c) \tag{4.1a}$$

$$\dot{h}_c = v_p - v_g \tag{4.1b}$$

$$r_{br} = f_{br}(r_c, h_c) \tag{4.1c}$$

$$\alpha_c = \arcsin\left\{1 - \left(\frac{h_c}{a}\right)^2 \left[1 + 0.6915\left(\frac{r_c}{a}\right)^{-1.1}\right]\right\} - \alpha_0 \tag{4.1d}$$

$$v_g = \frac{\phi_s - \phi_l}{\rho_s \Delta H} \tag{4.1e}$$

where r_c is the crystal radius, h_c is the height of the meniscus at the three-phase boundary, v_p is the pulling speed, v_g is the growth rate of the crystal (in axial direction assuming a flat solid-liquid interface) and α_c is the cone angle at the interface. Finally, the output r_{br} is the bright ring radius obtained from the camera image. It is assumed to depend on the crystal radius and the meniscus height which is expressed in general by the function f_{br}. That this approach is reasonable will be shown in the next chapter.

The expression of α_c in (4.1d) is derived from the analytical approximation of meniscus height h_c given in (3.9). It is noteworthy that the angle ϕ in (3.9) equals $90^\circ - \alpha$, such that the angle $\alpha = \alpha_0 + \alpha_c$ denotes the overall growth angle, where α_0 is the contact/wetting angle at constant radius growth when cone angle $\alpha_c = 0$. As explained in Sect. 3.3, a is the Laplace constant, also referred to as the *capillary constant*.

The value for $\alpha_0 = 11^\circ$ (Tatarchenko 1993, Rahmanpour 2017). In the case of Si, the values of interfacial surface tension and melt density are $\sigma_{lv} = 0.732\,\mathrm{N\,m^{-1}}$ and $\rho_l = 2570\,\mathrm{kg\,m^{-3}}$, respectively, that in turn, results in the value of Laplace constant as $a = 7.62\,\mathrm{mm}$.

With reference to (4.1e), ϕ_s is the heat flux from the interface into the crystal, while ϕ_l is the heat flux from the meniscus to the interface. ρ_s is the density of the solid crystal, and ΔH is the specific latent heat of fusion. The derivative of the meniscus height expressed in (4.1b) assumes perfect compensation for melt level changes through crucible lift. The crystal growth rate is a direct result of the fact that the rate of solidification results in a proportional rate of heat release. Therefore the growth rate is determined directly from the difference between the rate of heat entering and leaving the interface. The heat balance across the crystallization interface should be maintained such that the net flow of heat is towards the crystallizing interface, i.e., the thermal flux density on the side of the crystal is higher than that on the melt side by the amount of heat released in the solidification process. Consequently, the continuous heat loss from the meniscus into the crystal ensures the continuity of crystallization/solidification (Winkler et al. 2010c).

4.2 Heater/Temperature Dynamics

This section describes a simplified model of the thermal dynamics from heater to the solidification interface. The total path for the heat transfer, from the heaters to the interface, is divided into control volumes. For each control volume a heat balance can be established from which an ordinary differential equation for its temperature can be deduced. In the following, two different modes of heat transfer are considered for the heat transfer across the meniscus, resulting in in two distinct

mathematical expressions of ϕ_l (cf. (4.1e)):

I. The heat transfer from the bulk of the melt into the meniscus is caused by convection, while the heat transfer across the meniscus itself is based on pure conduction. This results in a model consisting of four control volumes (cf. Fig. 4.1(a)). In this model, the heat flux entering the solid-liquid interface from the melt will depend on the meniscus height as will be shown in Sect. 4.2.1. This mode of heat transfer will be referred to as *Model I* in the text to follow.

II. The heat transfer from the bulk of the melt to the interface is based on convection only, resulting in a model consisting of three control volumes (cf. Fig. 4.1(b)). Here, the varying meniscus height does not have any influence on the heat flux entering the solid-liquid interface (cf. Sect. 4.2.2). This model of heat transfer will be referred to as *Model II* in the subsequent text.

These two assumptions are in a sense two extremes and the actual heat transfer across the meniscus is likely to be a combination of both convection and conduction. Thus, a control design that works for both models can be expected to work for the heat transfer mode(s) occurring in the actual process.

4.2.1 Heat transport in Model I

The first two control volumes are used to provide a coarse second-order approximation to the dynamics of the heat transfer from the heater to the melt. The temperature T_1 of control volume 1 may roughly correspond to the temperature measured by the pyrometer on the graphite lining surrounding the heaters, while the second control volume of fictional temperature T_2 introduces an additional time lag representing the thermal inertia of the inner assemblies surrounding the crucible. Their dynamics is given by

$$\dot{T}_1 = \frac{Q_H - Q_1 - Q_{loss,1}}{\tau_1} \tag{4.2a}$$

$$\dot{T}_2 = \frac{Q_1 - Q_{in} - Q_{loss,2}}{\tau_2} \tag{4.2b}$$

where τ_1, τ_2, are time constants used to mimic the slow heat transfer dynamics from the heaters to the melt (Rahmanpour et al. 2017). These parameters are chosen to approximate an effective time delay of $600\,\mathrm{s}$ for each of the two control volumes. In (4.2) one has the heat input Q_H from the heaters, i.e., the manipulated variable for the ATC controller, the thermal energy Q_1 that enters the control volume 2 from control volume 1 and the thermal energy Q_{in} that enters the melt. These heat transfer rates are modeled using (Rahmanpour et al. 2017)

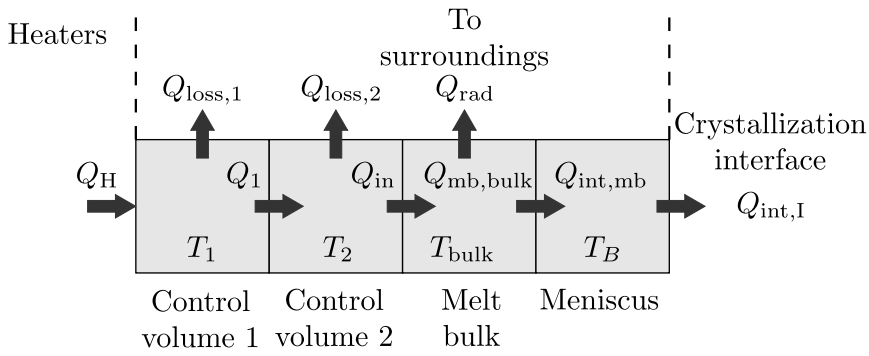

(a) Model I: Conduction based heat transport across the meniscus.

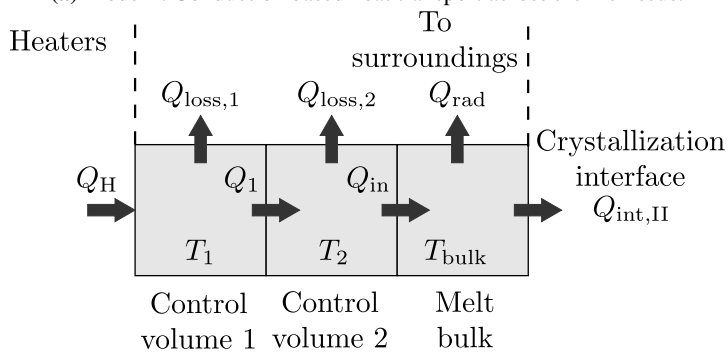

(b) Model II: Convection based heat transport across the meniscus.

Figure 4.1: Illustration of the lumped heat transport models with their control volumes.

$$Q_1 = \beta_1 \left(T_1 - T_2\right) \tag{4.3}$$

and

$$Q_{in} = \beta_2 \left(T_2 - T_{bulk}\right), \tag{4.4}$$

with the overall heat transfer coefficients β_1, β_2 between the control volumes and the melt bulk with temperature T_{bulk}. The two heat losses $Q_{loss,1}$ and $Q_{loss,2}$ in (4.2) are assumed to be constant for a shorter time scale of dynamical analysis.

The last two control volumes to the right of this model distinctively represent the melt bulk region and the meniscus, respectively. Together, these indicate the complete heat transfer from the bulk of the melt to the crystal interface, which in turn, is determined by two independent heat transfers in series, i.e., the convective heat transfer through the bulk of the melt and the conductive heat transfer through the meniscus. The dynamics of the melt bulk temperature T_{bulk} reads

$$\dot{T}_{bulk} = \frac{Q_{in} - Q_{mb,\,bulk}}{V_s \cdot \rho_l \cdot C_p}, \tag{4.5}$$

where V_s, ρ_l and C_p define the melt volume, the density and the specific heat capacity of liquid Si, respectively. The convection-driven heat flow $Q_{mb,\,bulk}$, from the melt bulk region into the meniscus, at temperature T_B, can be calculated from

$$Q_{mb,\,bulk} = \beta_{conv,I}\,(T_{bulk} - T_B), \tag{4.6}$$

with the $\beta_{conv,I}$ as the convective heat transfer coefficient.

The conductive heat flow through the meniscus $Q_{int,\,mb}$ reaches the crystallization interface (with Si melting point temperature T_S). Mathematically, it reads as

$$Q_{int,\,mb} = \frac{k_l\,A_i\,(T_B - T_S)}{h_c}, \tag{4.7}$$

where $A_i = \pi\,r_c^2$ is the cross-sectional area of the solidification interface and k_l is the heat conductivity of liquid Si[1]. Due to a short length of the meniscus, it is reasonable – on the timescale of relevance for crystal growth – to neglect the *dynamics* of T_B, i.e., $\dot{T}_B = 0$, and assume the two heat transfers $Q_{int,\,mb}$ and $Q_{mb,\,bulk}$ to be equal. This allows us to eliminate T_B from (4.6), (4.7) and arrive at the following expression for the overall heat flow $Q_{int,I}$ entering the crystallization interface from the bulk:

$$Q_{int,I} = \beta_{int}(T_{bulk} - T_S) \tag{4.8}$$

$\beta_{int} = (\beta_{conv,I}^{-1} + h_c\,k_l^{-1}\,A_i^{-1})^{-1}$ is the overall heat transfer coefficient that combines the two coefficients from expressions (4.6) and (4.7) in series. Similarly (cf. (4.6), (4.7)), the heat transfer coefficient $\beta_{conv,I}$ is given by

$$\beta_{conv,I} = \frac{k_l\,A_i\,(T_{B,0} - T_S)}{h_c\,(T_{bulk,0} - T_{B,0})}, \tag{4.9}$$

using initial steady-state values $T_{B,0}, T_{bulk,0}$ for T_B, T_{bulk}, respectively. Hence, its value is assumed constant throughout the simulations. Moreover, $\beta_{conv,I}$ is calcuated by balancing thermal gradient in proportion to the desired growth rate. This means that growth conditions at the crystallization interface are balanced, i.e., thermal gradient results in the desired growth rate only.

[1] As can be seen in Eq. (4.7), the temperature gradient is assumed to be $(T_B - T_S)/h_c$ which is a quite rough but common approximation in lumped parameter models of the Cz process (Hurle et al. 1990). In reality, the thickness of the thermal boundary layer is the driving force for conductive heat transfer. But since this layer is not modeled here this approximation is used. It simply reflects the heuristic assumption that the closer the interface to the hot melt, the more the crystallization is inhibited (Neubert and Winkler 2014).

Eventually, the heat flow from the meniscus surface splits into two parts, i.e., one part enters the interface $Q_{int,I}$, and another part gets radiated out to the chamber surroundings Q_{rad}. This bifurcated flow of heat is mathematically represented by $Q_{mb,bulk} = Q_{int,I} + Q_{rad}$, where the radiative heat loss from the melt surface is expressed as:

$$Q_{rad} = A_{fm}\, F_{mc}\, \epsilon_m\, \sigma_{sb}\, (T_{bulk}^4 - T_{env}^4) \tag{4.10}$$

where A_{fm} is the free melt surface area expressed as $A_{fm} = \pi\,(R_{cru}^2 - r_c^2)$, F_{mc} is the radiation view factor considering the heat radiation from the free melt surface to the crystal surroundings, ϵ_m is the melt emissivity, σ_{sb} is the *Stefan-Boltzmann constant* and T_{env} is the temperature of the environment. Note, that under these assumptions, (4.5) can be rewritten as

$$\dot{T}_{bulk} = \frac{Q_{in} - Q_{int,I} - Q_{rad}}{V_s \cdot \rho_l \cdot C_p}. \tag{4.11}$$

4.2.2 Heat transport in Model II

In the case of model II, only the convective heat transport from the melt to the crystallization interface is considered, i.e., the bulk of the melt, as well as the temperature of the meniscus, are at the same temperature level. Hence, the model consists of only three control volumes (cf. Fig. 4.1, II).

The temperature dynamics of the first two control volumes is given by (4.2), while the bulk melt temperature T_{bulk} is given by:

$$\dot{T}_{bulk} = \frac{Q_{in} - Q_{int,II} - Q_{rad}}{V_s \cdot \rho_l \cdot C_p}. \tag{4.12}$$

In the above equation (4.12), the radiative heat loss Q_{rad} is formulated as in (4.10), while $Q_{int,II}$, the *convective* heat transfer from the melt bulk to the crystallization interface, is given as

$$Q_{int,II} = \beta_{conv,II}\,(T_{bulk} - T_S), \tag{4.13}$$

where $\beta_{conv,II}$ represents the convective heat transfer from the bulk of the melt to the crystallization interface. The value of $\beta_{conv,II}$ given by

$$\beta_{conv,II} = \frac{\phi_l A_i}{(T_{bulk,0} - T_S)}$$

is calcuated by assuming balanced growth conditions at the interface, i.e., thermal gradient is proportional to the nominal growth rate.

4.3 Overall Model

With the results from Sect. 4.1 and 4.2, the overall Cz dynamics, including both growth and temperature dynamics, can be written in state-space form with the state vector $\mathbf{x} = (r_c, h_c, T_{bulk}, T_1, T_2)^T$:

$$\dot{\mathbf{x}} = \begin{pmatrix} v_g \tan(\alpha_c) \\ v_p - v_g \\ (Q_{in} - Q_{int} - Q_{rad})/(V_s\, \rho_l\, C_p) \\ (Q_H - Q_1 - Q_{loss,1})/\tau \\ (Q_1 - Q_{in} - Q_{loss,2})/\tau \end{pmatrix} = \mathbf{f(x,u)} \tag{4.14a}$$

$$\mathbf{y} = \begin{pmatrix} r_{br} \\ T_1 \end{pmatrix}, \qquad \mathbf{u} = \begin{pmatrix} v_p \\ Q_H \end{pmatrix}. \tag{4.14b}$$

In (4.14a), Q_{int} can either be $Q_{int,I}$ or $Q_{int,II}$ depending on the choice of the heater model. The growth rate v_g is calculated according to (4.1e) with $\phi_l = Q_{int}/A_i$. In this model, u indicates the input vector comprising two manipulating inputs (v_p, Q_H), while the measured output y comprises the bright ring radius r_{br} and the temperature T_1 sensed by the pyrometer. Note, that in case of model I the growth rate depends on the meniscus height (cf. (4.7), (4.8)). A method for determining r_{br} is described in detail in Sect. 5.2. The initial/nominal values of various model parameters are listed in Table 4.1.

Table 4.1: Parameters/ states for thermal models I and II. The initial values of states and nominal values of parameters are taken from Rahmanpour et al. (2017), Gevelber and Stephanopoulos (1987).

States/parmeters for the two thermal models			
Q_H	$58.6\,\mathrm{kW}$	Q_1	$27.3\,\mathrm{kW}$
Q_{in}	$7.3\,\mathrm{kW}$	$Q_{loss,1}$	$30\,\mathrm{kW}$
$Q_{loss,2}$	$20\,\mathrm{kW}$	Q_{out}	$7.3\,\mathrm{kW}$
T_1	$1970\,\mathrm{K}$	T_2	$1914\,\mathrm{K}$
T_S	$1683\,\mathrm{K}$	$T_{B,0}$	$1688.6\,\mathrm{K}$
$T_{bulk,0}$	$1704\,\mathrm{K}$	ρ_l	$2570\,\mathrm{kg\,m^{-3}}$
ρ_s	$2330\,\mathrm{kg\,m^{-3}}$	C_p	$1000\,\mathrm{J\,kg^{-1}\,K^{-1}}$
ΔH	$1.79 \times 10^6\,\mathrm{J\,kg^{-1}}$	ϕ_s	$1.3 \times 10^5\,\mathrm{W\,m^{-2}}$
ϕ_l	$4.6 \times 10^4\,\mathrm{W\,m^{-2}}$	ϵ_m	0.2
σ_{sb}	$5.67 \times 10^{-8}\,\mathrm{W\,m^{-2}\,K^{-4}}$	T_{env}	$1262\,\mathrm{K}$
F_{mc}	0.5	k_l	$57\,\mathrm{W\,m^{-1}\,K^{-1}}$
T_{bulk}	$1704\,\mathrm{K}$	T_B	$1688.6\,\mathrm{K}$
Q_{mb}	$7.3\,\mathrm{kW}$		

Remark 1. *The basic crystal growth dynamics in Sect. 4.1 are based on the hydrodynamic effects that are established in literature and theory, while the thermal model (cf. Sect. 4.2) is rather qualitative and cannot be expected to be very accurate. The validity of the model and its use in this thesis is discussed further in Chap. 8.*

Chapter 5

Ray-Tracing Method for Bright Ring Radius Estimation

This chapter delves into the mathematical details of the 3D ray-tracing scheme to simulate the camera image and the measurement of the crystal radius. The dynamics of the ray-tracing simulation reveal the presence of anomalous behaviour in the radius measurement.

This chapter is based on the work presented in Bukhari et al. (2021a).

Any automated feedback control system needs measured quantities in order to gain information about the current state of the process, especially the deviation of the quantities to be controlled from their setpoint values (i.e., the crystal radius and the growth rate). In the Cz process, the measured variable generally used for the feedback control of the crystal radius can either be the force acting on a load cell connected with the upper end of the pulling rod (usually referred to as *weight measurement*[1]) (Levinson 1959, Bardsley et al. 1974b; 1977a) or the radius measurement of a CCD camera (cf. Fig. 5.1), installed through one of the viewports on a pulling chamber (Patzner et al. 1967, Digges et al. 1975, Lorenzini et al. 1974, Duffar 2010). Since the boundary between crystal and the melt is indistinguishable, the CCD camera is adjusted to continuously focus the meniscus in the vicinity of the three-phase boundary. It optically senses the radius of a specific bright ring formed on the meniscus. The bright annular rings on the meniscus are caused by the reflection of light by the curved meniscus in such a way that the hotter crucible wall and the heatshield underside form varying brightness patterns on the illumi-

[1] In fact it measures the weight of the crystal *and* the forces resulting from the surface tension and hydrostatic pressure of the meniscus.

nated meniscus. Any clearly and consistently identifiable point on this brightness pattern, illuminated by a specific component within the hot zone, may serve as a basis for the crystal radius measurement. Therefore, in the jargon of crystal growers, this very radius measurement is termed as the *bright ring radius* denoted by r_{br}. Fig. 5.1 shows an image of the illuminated meniscus as captured with a CCD camera. It is apparent that the bright ring image is a view-occluded glowing ring as some of the meniscus reflections from the opposite side of the camera are obscured either by the heat shield or the cylindrical ingot in the centre or both.

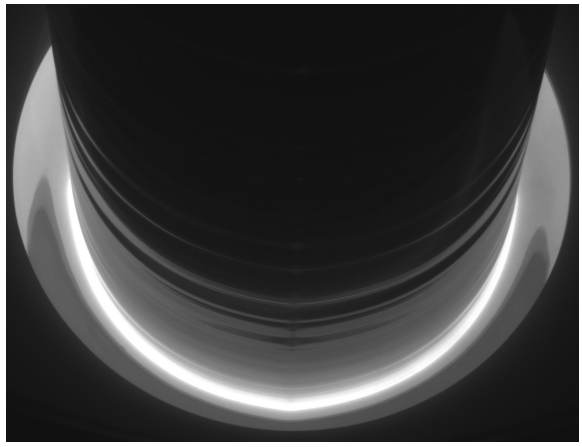

Figure 5.1: Actual plant image from the CCD camera showing the bright ring on the meniscus. *Note: The viewing angle is from above the melt looking down on to its surface.*

5.1 Overview of the Measurement Anomaly

The idea behind the weight measurement method is that the change of crystal mass per time unit divided by the pulling speed is proportional to the square of the crystal radius (Satunkin and Leonov 1990). For that purpose, the measured weight signal is differentiated with respect to time and used as an indirect value for the controlled variable. However, since the measured weight signal is also affected by the meniscus dynamics this equality does not hold, especially during changes of the radius. For example, in the case of a crystal radius increase the vertical component of the meniscus' surface tension decreases. Additionally, the melt column below the crystal (responsible for the static pressure) decreases and – because the density of the melt is larger than that of the solid – another decreasing effect is added. As a consequence, the measured variable initially responds inversely to the actual crystal radius. This anomaly in the measured signal is depicted in Fig. 5.2 (middle) for a change of the crystal radius in the positive direction. This fact is

well-known and widely investigated in the Cz crystal growth literature (Bardsley et al. 1977b, Hurle 1977, Gevelber et al. 1988, Gevelber 1994a).

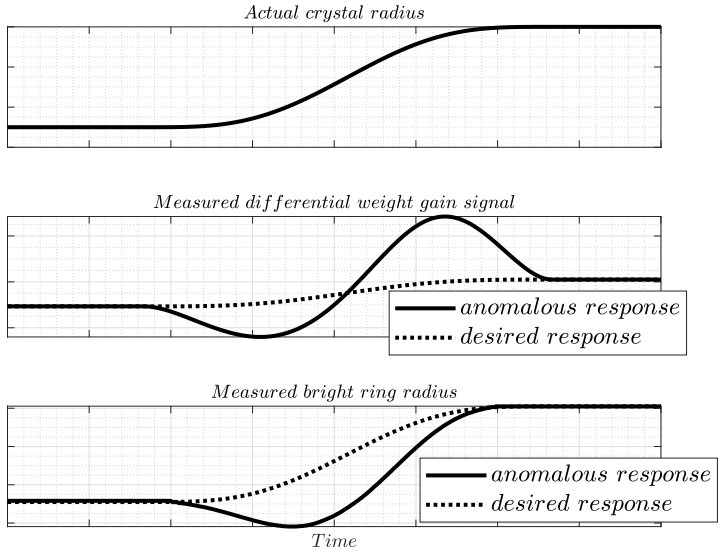

Figure 5.2: Illustration of anomalous behaviour in the bright ring and weight measurement signals.

Similar anomalous behaviour is known to be possessed by the bright ring measurement in a qualitative sense (Gevelber 1994a). For example, with a decrease in pulling speed, the meniscus height decreases, making the meniscus profile flatter. This effect will result in an increase in the crystal radius, while at the same time causing the camera to initially detect a decrease in the bright ring radius. Only after the crystal radius has grown significantly will the camera detect an increase in the bright ring radius. Fig. 5.2 (bottom) illustrates this anomalous behaviour measuring the bright ring radius. Although there are publications dealing with the calculation of the bright ring diameter (Kimbel and O'Sullivan 2001) a thorough investigation of the impact of the anomalous behaviour on control system performance remains. This work, in particular, aims at investigating the aforementioned from both systematic and quantitative standpoints.

5.2 Bright Ring Radius Estimation

The ray-tracing method had been adopted by Kimbel and O'Sullivan (2001) to estimate a bias between the actual crystal radius and the measured bright ring radius for a static case. However, in this chapter, a rigorous ray-tracing simulation, combined with the crystal growth dynamics, is developed to dynamically simulate the camera image of the illuminated meniscus. This simulated camera image is further

used up for control system design and analysis. Moreover, the dynamic trace of the bright ring radius measurement aids in an effective and improved control system design (cf. Chap. 6).

Since this very measurement depends on the geometry of the hot zone, the shape of the meniscus, and the position and orientation of the camera, therefore these components are highlighted in a simplified ray-tracing setup as shown in Fig. 5.3. It presents a vertical cross-sectional view of the Cz growth furnace (crucible wall, heat-shield, and camera location). For the sake of simplicity, only one ray from each source is shown to be incident onto the meniscus and reflected thereof before reaching the camera. Though the rays may undergo multiple reflections before reaching the camera, an instance of the ray reflected twice from the meniscus is shown by a dashed line in the referred figure.

It is clear that a key factor when modeling the dynamics of the bright ring radius is the knowledge of the meniscus shape. The meniscus shape can be calculated from the so-called *Laplace-Young equation* that accounts for surface tension, gravity, and hydrostatic pressure to express the shape and height of the meniscus. Unfortunately, there is no analytical solution to the Laplace-Young equation, which, therefore, has to be solved numerically (Huh and Scriven 1969). An alternative to the aforementioned approach is the use of an analytical approximation of the meniscus shape.

5.2.1 Meniscus shape approximation

An approximation of meniscus shape, as derived by Hurle (cf. Sect. 3.3) is applied to obtain meniscus profile between the three-phase point and the crucible wall. For the sake of completeness, the expression (3.7) is repeated below (Hurle 1983):

$$\begin{aligned} r(h_c, r_c, z) = r_c &+ \sqrt{\frac{2}{A} - h_c^2} - \sqrt{\frac{2}{A} - z^2} \\ &- \frac{1}{\sqrt{2A}} \ln \left[\frac{z}{h_c} \cdot \frac{\sqrt{2} + \sqrt{2 - A \cdot h_c^2}}{\sqrt{2} + \sqrt{2 - A \cdot z^2}} \right] \end{aligned} \tag{5.1}$$

In (5.1), r and z are the radial and vertical coordinates of the meniscus surface, respectively. Thus, one has $(r, z) = (r_c, h_c)$ where the meniscus connects to the crystal, while roughly $(r, z) = (R_{cru}, 0)$ at the crucible wall. The parameter A is defined as:

$$A = \frac{1}{a^2} + \frac{\cos(\alpha)}{2 r_c \, h_c}.$$

This meniscus profile can be extended to define a full 3D meniscus surface by rotating the profile about the z-axis, i.e., 360° along the azimuthal plane.

In a nutshell, to start with the ray-tracing simulation, the information about the Cz growth model parameters, i.e., (r_c, h_c) as discussed in Sect. 4.1, and a knowledge of the meniscus profile (cf. (5.1)) and hot zone geometry (cf. Sect. 5.2.2) are necessary. Later will be presented, the computation of light rays incident on the meniscus and the outgoing rays reflected in the camera. These particular computations focus on vector mathematics. Therefore, the direction of rays may not be confused with those of vectors.

5.2.2 Hot zone geometry

The schematics of the hot zone used in illustrating the ray-tracing method are shown in Figs. 5.3 and 5.4. The reference frame origin $\mathcal{O}$ is placed at the level

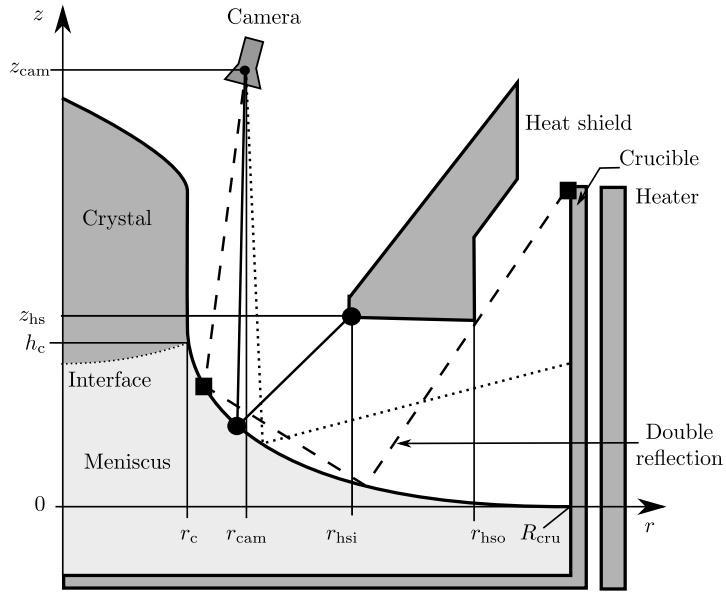

Figure 5.3: Ray-tracing set up showing incident and reflected light rays within the growth furnace.

of free melt surface such that the horizontal x-axis and the lateral y-axis form the xy-plane spanning the base of the meniscus, while the z-axis extends vertically along the centre of the ingot. The camera is located in the xz-plane ($y = 0$). In terms of cylindrical coordinates, the camera location is in the rz-plane, i.e., in the 0° azimuthal plane. The hot zone components, such as the crucible wall and annular heat shield surrounding the growing crystal, have dimensions defined as:

- Crucible radius: R_{cru}
- The coordinates for the heat shield underside are described in terms of its

height as well as inner and outer radii given by:

- z_{hs} is the height of the heat shield underside w.r.t. the free melt surface
- r_{hsi} is the inner radius of the heat shield underside w.r.t. $\mathcal{O}$
- r_{hso} is the outer radius of the heat shield underside w.r.t. $\mathcal{O}$

- The camera location w.r.t. $\mathcal{O}$ is described by the position vector $\vec{\mathbf{p}}_c$ such that: $\vec{\mathbf{p}}_c = x_{cam}\hat{i} + 0\hat{j} + z_{cam}\hat{k}$ [2], where
  - z_{cam} is the height of the camera w.r.t. the free melt surface
  - x_{cam} is the radial location of the camera, i.e., $x_{cam} = r_{cam}$ as $y_{cam} = 0$

5.2.3 Computation of tangents and normals to the meniscus surface

Followed by the generation of 3D meniscus surface is the calculation of tangents and normals to the entire meniscus surface. This, in turn, helps to determine the incoming and outgoing rays for the camera image simulation. The tangents and the unit normals to the meniscus surface are mathematically notated by $\vec{\mathbf{T}}$ and $\vec{\mathbf{N}}$ in $\mathbb{R}^3$, respectively. Since the meniscus surface is axisymmetric, tangents and normals can be calculated using the 2D meniscus curve, and then rotate these around the z-axis to the required azimuthal orientation.

For any arbitrary point $(x_{m_0}, 0, z_{m_0})$ (or equivalently $(r_{m_0}, 0, z_{m_0})$ in cylindrical coordinates) on the meniscus profile such that $z_{m_0} = f(r_{m_0})$, the tangent vector can be calculated as:

$$\begin{aligned}\vec{\mathbf{T}}|_{(r_{m_0},0,z_{m_0})} &= \frac{1}{\sqrt{1+f'^2(r)}} \begin{bmatrix} \frac{\Delta r}{\Delta r} \\ \frac{\Delta \theta}{\Delta r} \\ \frac{\Delta f(r)}{\Delta r} \end{bmatrix} \Bigg|_{(r_{m_0},0,f(r_{m_0})} \\ &= \frac{1}{\sqrt{1+f'^2(r_{m_0})}} \begin{bmatrix} 1 \\ 0 \\ f'(r_{m_0}) \end{bmatrix}. \end{aligned} \tag{5.2}$$

The normal vector, orthogonal to the tangent, is given as

$$\vec{\mathbf{N}}|_{(r_{m_0},0,z_{m_0})} = \frac{1}{\sqrt{1+f'^2(r_{m0})}} \begin{bmatrix} -f'(r_{m_0}) \\ 0 \\ 1 \end{bmatrix}. \tag{5.3}$$

Finally, the unit normal to any arbitrary point in question (say $\mathbf{m}_{(r,\theta,z)}$) can be determined by rotating $\vec{\mathbf{N}}|_{(r_{m_0},0,z_{m_0})}$ through an angle θ about the z-axis, such that

$$\vec{\mathbf{N}}_{m_{(r_m,\theta,z_m)}} = R_z(\theta) \cdot \vec{\mathbf{N}}|_{(r_{m_0},0,z_{m_0})}, \tag{5.4}$$

[2] $\hat{i}$, $\hat{j}$ and $\hat{k}$ are the unit vectors directed along x, y and z-axes, respectively

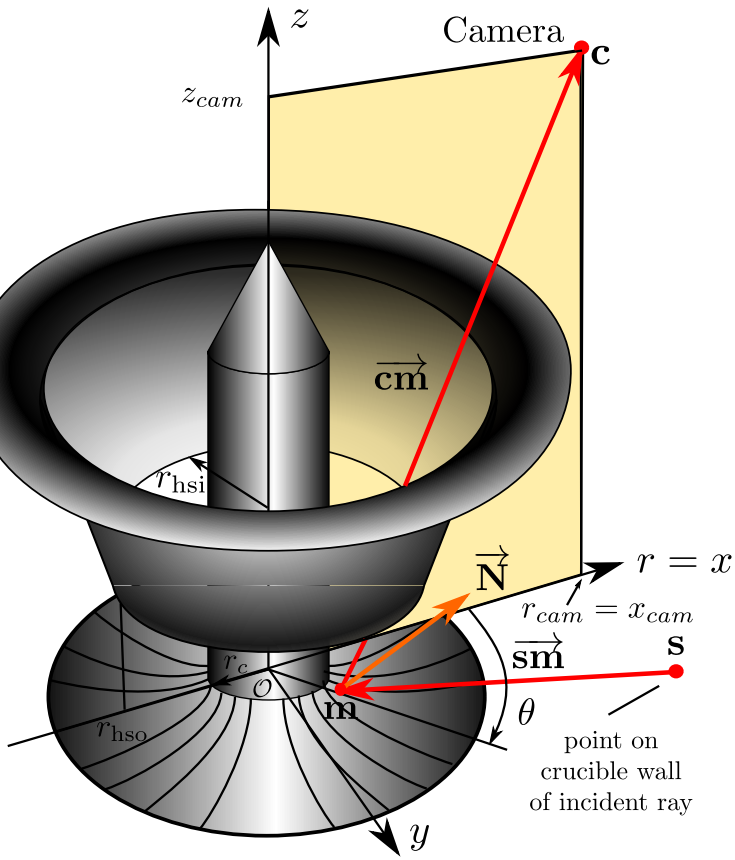

Figure 5.4: 3D ray-tracing scheme featuring an instance of an incident ray $\vec{\mathbf{sm}}$ emerging from the crucible wall. The reflected ray from a point (**m**) reaches the camera with location marked as (**c**). The incident and reflected rays may or may not exist in the same plane.

where $R_z(\theta)$, the rotation matrix yielding the desired rotation through an arbitrary angle θ, about the z-axis is given as

$$R_z(\theta) = \begin{bmatrix} \cos(\theta) & -\sin(\theta) & 0 \\ \sin(\theta) & -\cos(\theta) & 0 \\ 0 & 0 & 1 \end{bmatrix}. \tag{5.5}$$

5.2.4 Computing incoming and outgoing rays

A rigorous ray-tracing method that abides the laws of reflection is employed to simulate the bright ring formation over the curved meniscus. Fig. 5.4 illustrates the schematic of the 3D ray-tracing. The outgoing ray that enters the camera after reflection from a point **m** on the meniscus (described by position vector $\vec{\mathbf{p}}_m$ in

cylindrical coordinates as (r_m, θ, z_m) or as (x_m, y_m, z_m) in cartesian coordinates) is given by

$$\begin{aligned}\overrightarrow{\mathbf{cm}} = \vec{\mathbf{p}}_c - \vec{\mathbf{p}}_m = \\ (x_{cam} - x_m)\hat{i} \; - \; y_m\hat{j} \; + \; (z_{cam} - z_m)\hat{k}.\end{aligned} \tag{5.6}$$

Based on the knowledge of meniscus normals given in (5.4), the incoming and outgoing rays to the meniscus and camera, respectively can be determined such that the angle of incidence equals the angle of reflection, though the two angles are not necessarily coplanar. For a specific point on the meniscus, the projection of the reflected ray $\overrightarrow{\mathbf{cm}}$ in the direction of normal vector $\vec{\mathbf{N}}$ at the same point is given by

$$proj_{\vec{\mathbf{N}}}\overrightarrow{\mathbf{cm}} = (\overrightarrow{\mathbf{cm}} \cdot \vec{\mathbf{N}})\vec{\mathbf{N}}, \tag{5.7}$$

where $(\cdot)$ indicates the vector dot product operation. Similarly, the projection of $\overrightarrow{\mathbf{cm}}$ in the direction orthogonal to $\vec{\mathbf{N}}$ is given as

$$proj_{\perp \longrightarrow \vec{\mathbf{N}}}\overrightarrow{\mathbf{cm}} = \overrightarrow{\mathbf{cm}} - proj_{\vec{\mathbf{N}}}\overrightarrow{\mathbf{cm}} = \overrightarrow{\mathbf{cm}} - (\overrightarrow{\mathbf{cm}} \cdot \vec{\mathbf{N}})\vec{\mathbf{N}}. \tag{5.8}$$

The orthogonal projection of incoming ray vector $\overrightarrow{\mathbf{sm}}$ is the same as the reflected ray vector $\overrightarrow{\mathbf{cm}}$ but with the opposite sign, i.e., $proj_{\vec{\mathbf{N}}}\overrightarrow{\mathbf{sm}} = -\overrightarrow{\mathbf{cm}} + (\overrightarrow{\mathbf{cm}} \cdot \vec{\mathbf{N}})\vec{\mathbf{N}}$. However, the projection of incoming ray vector in the direction of normal vector $\vec{\mathbf{N}}$ is the same as that of the reflected ray vector, i.e., $proj_{\vec{\mathbf{N}}}\overrightarrow{\mathbf{sm}} = (\overrightarrow{\mathbf{cm}} \cdot \vec{\mathbf{N}})\vec{\mathbf{N}}$. Thus, the incoming ray from a given source point inside the hot zone, represented as $\overrightarrow{\mathbf{sm}}$, is given by

$$\begin{aligned}\overrightarrow{\mathbf{sm}} &= (\overrightarrow{\mathbf{cm}} \cdot \vec{\mathbf{N}})\vec{\mathbf{N}} - \overrightarrow{\mathbf{cm}} + (\overrightarrow{\mathbf{cm}} \cdot \vec{\mathbf{N}})\vec{\mathbf{N}} \\ &= 2(\overrightarrow{\mathbf{cm}} \cdot \vec{\mathbf{N}})\vec{\mathbf{N}} - \overrightarrow{\mathbf{cm}} \\ &= 2\vec{\mathbf{N}}(\vec{\mathbf{N}}^T \overrightarrow{\mathbf{cm}}) - \overrightarrow{\mathbf{cm}} \\ &= (2\vec{\mathbf{N}}\vec{\mathbf{N}}^T - \mathbf{I})\overrightarrow{\mathbf{cm}},\end{aligned} \tag{5.9}$$

where I is the identity matrix. It is noteworthy that the incident rays $\overrightarrow{\mathbf{sm}}$ and the reflected rays $\overrightarrow{\mathbf{cm}}$ may pass through planes corresponding to different azimuthal orientations. In order to determine if the source of illumination on the illuminated meniscus is the crucible wall or the heat shield underside, the following steps can be followed:

- A position vector for the point **s** of incident ray w.r.t. $\mathcal{O}$, lying at an arbitrary radial distance $\leq R_{cru}$ from the origin can be determined as:

$$\vec{\mathbf{p}}_s = \vec{\mathbf{p}}_m \; + \; \overrightarrow{\mathbf{sm}}, \tag{5.10}$$

  - In (5.10), $\overrightarrow{\mathbf{sm}}$ shall not be confused with the incoming ray (cf. Fig. 5.4). Instead, the expression (5.10) makes use of vector mathematics by interpreting $\overrightarrow{\mathbf{sm}}$ as a vector that has to be extended appropriately as in (5.11).

- The intersection of the incident ray with the crucible wall can be found by scaling $\overrightarrow{\mathbf{sm}}$ by a factor 'k' such that it emerges from the crucible wall of radius R_{cru}. This can be achieved by solving the expression given in (5.11) for the positive root of 'k':

$$(x_m + k\,\overrightarrow{\mathbf{sm}}_x)^2 + (y_m + k\,\overrightarrow{\mathbf{sm}}_y)^2 = R_{cru}^2. \tag{5.11}$$

- The elevation of the scaled up incident ray $k\,\overrightarrow{\mathbf{sm}}$ emerging from the crucible wall is given by $k\,\overrightarrow{\mathbf{sm}}_z$

  - The double reflection (shown in Fig. 5.3) is caused by the incoming ray that emerges from the portion of the crucible wall lying below the melt level, i.e., the z-coordinate of $k\,\overrightarrow{\mathbf{sm}}$ is negative ($k\,\overrightarrow{\mathbf{sm}}_z < 0$). The origin of rays undergoing double reflection can be found by calculating another reflection where the incoming ray hits the meniscus surface. The details are omitted for brevity. Note that it is possible for some rays to be reflected more than twice, especially when the meniscus close to the crystal is highly curved, which may occur when the meniscus is high. Such multiple reflections have not been considered further in this work – but the calculations required to include them in the ray-tracing are more tedious than difficult.

- The incident ray from the heat shield is the one whose x and y-coordinates at z_{hs} satisfy the following inequality condition:

$$r_{hsi} < \sqrt{sm_x^2 + sm_y^2} < r_{hso} \tag{5.12}$$

Thus, a 3D ray-tracing simulation, based on the procedure outlined above, traces every ray that reaches the camera back to its emission point (the complete annular heat shield surrounding the growing crystal and the cylindrical crucible wall containing the molten Si). The rays, which are reflected twice from the meniscus, are also included in the simulated bright ring image. However, some of the reflections from the meniscus surface, lying on the side farther to the camera, are obscured either due to the presence of a cylindrical crystal ingot or by the heat shield. Likewise, the heat shield blocks many of the light rays which emanate from various emission points, above and beyond the heat shield underside, from reaching the camera.

The various sources of illumination on the simulated bright ring image are depicted in Fig. 5.5.

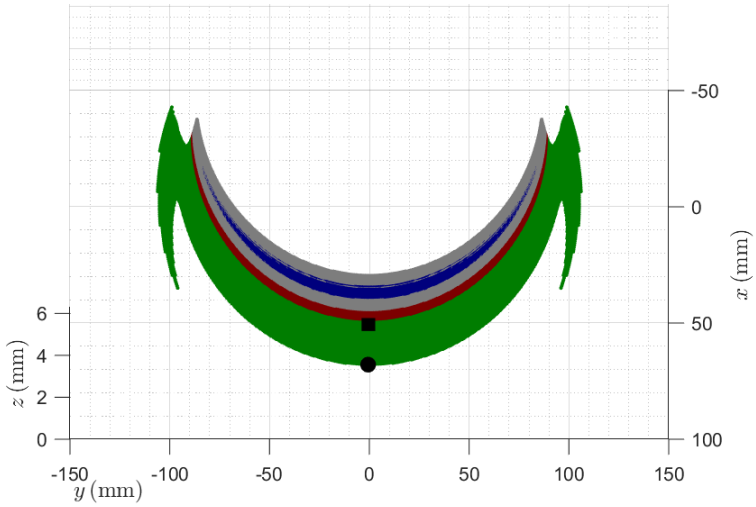

Figure 5.5: Colour-coded meniscus image where each coloured region corresponds to illumination by a specific structure/component within the hot zone, i.e., heat shield base ( ), crucible wall ( ), from heat shield base after double reflection ( ), and from crucible wall after double reflection ( ). The view is symmetric on either side of the xz[3]-plane/camera plane. *Note: The colours in the meniscus image do not relate to the intensity/brightness as observed in the camera image (cf. Fig. 5.1).*

The brightness sensed by the camera will depend on three factors:

i.) The brightness of the emitting surface.

ii.) The orientation of the emitting surface relative to the direction of the emitted ray.

iii.) The focusing of light caused by the curvature of the meniscus.

Accounting accurately for i.) will require knowledge both of the emissivity of the heat shield and the crucible wall, as well as the temperature distribution along these surfaces. Due to the lack of such information that can be obtained through some very detailed simulators only, it is assumed that both the underside of the heat shield and the crucible wall have uniform (and the same) brightness. Luckily,

[3]The x and y-axes in Figs. (5.5 & 5.6) define the radial coordinates of the meniscus, i.e., $r = \sqrt{x^2 + y^2}$, while z-axis represents the height of the meniscus above the melt surface. Thus, the plane of the camera expressed in cylindrical coordinates is $(r, \theta = 0, z)$.

this simplification does not impede the ability to study the bright ring anomaly, as will become apparent.

Factors ii.) and iii.) are accounted for by performing small perturbations around the point on the meniscus where the ray is reflected before entering the camera. Let these perturbations define the vertices of a region on the meniscus surface, and let A_m be the area of that region when projected in the direction of the ray $\overrightarrow{\mathbf{cm}}$. Reflection calculations are then performed to find the point of origin for each of the perturbed rays. The origins of the perturbed and reflected rays define a region on the emitting surface. Let A_s be the area of this region of the emitting surface, when projected in the direction of the emitting ray $\overrightarrow{\mathbf{sm}}$. A relative brightness measure[4] is then found from the ratio of A_s to A_m.

The calculated brightness profile obtained, therefore, is illustrated in Fig. 5.6 – where the colour denotes the brightness of the reflection..

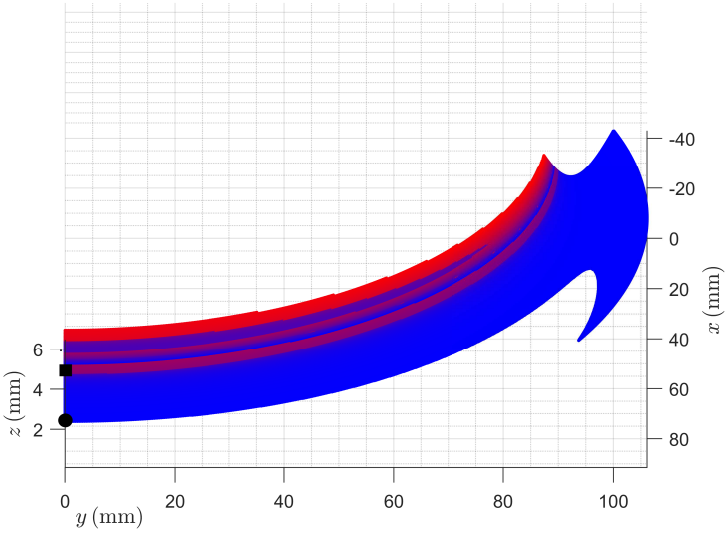

Figure 5.6: Theoretically calculated brightness profile as observed by the camera. Minimum brightness ( ); maximum brightness ( ). Since, the view is symmetric on either side of the xz-plane/camera plane, the left portion of the meniscus is not shown.

An effort was made to correlate the brightness pattern of Fig. 5.6 with that of the actual image (cf. Fig. 5.1) from the plant. Unfortunately, this didn't turn out as

[4]Note that it would be easy to account also for the brightness of the emitting surface, if such information is available.

planned/expected because camera images were saturated and it was not possible to identify distinct boundaries due to different sources. Another possible reason is the increased noise levels, thereby, creating blurry effects on the actual image. However, a camera with better resolution and faster sampling may render the 3D simulation to identify different features on the bright ring.

In order to use a feature of the camera image for control of the crystal radius, two obvious criteria must be fulfilled: i.) the feature should be located close to the actual crystal radius, and ii.) the feature should be clearly and reliably identifiable in the camera image for all conditions that are expected during the body stage of the process (i.e., for all values of crystal radius and meniscus height that are likely to occur in the body stage) it should be clearly and reliably identifiable in the camera image. Studying the calculated reflection images (and comparing to the camera image in Fig. 5.1), two such features can be identified:

- A point marked as a '■' on the meniscus in Figs. 5.5 & 5.6, illuminated by a ray that emerges from a higher point on the crucible wall while touching simultaneously the outermost edge of heat shield, can distinctively be identified.
- The innermost edge of the underside of heat shield) illuminating a point '●' on the meniscus in Figs. 5.5 & 5.6.

The first of these features indicated by '■' is closer to the actual crystal radius and is, therefore, the preferred feature to use for crystal radius control. It corresponds to the lower brightness border in the overexposed Fig. 5.1. Knowledge of the point from where the light that causes this feature originates, allows us to study the behaviour of the corresponding measurement under dynamical process conditions.

5.3 Anomaly Detection via 3D Ray-Tracing Simulation

Under normal operating conditions, physical systems rarely encounter any abrupt changes in their physical parameters/state variables. Therefore, the objective is to input a smooth crystal radius change to the ray-tracing simulation and investigate how the resultant bright ring measurement differs from the actual input signal (crystal radius). Thus, a pulling speed profile is selected[5] such that it drives the Cz dynamics to generate an output that comprises of smooth profile for the crystal radius.

Fig. 5.7 depicts how the chosen pulling speed profile, driving the Cz dynamics, results in the desired crystal radius (r_c) variation. Besides, the same figure shows

[5]Details can be seen in (Winkler et al. 2010a)

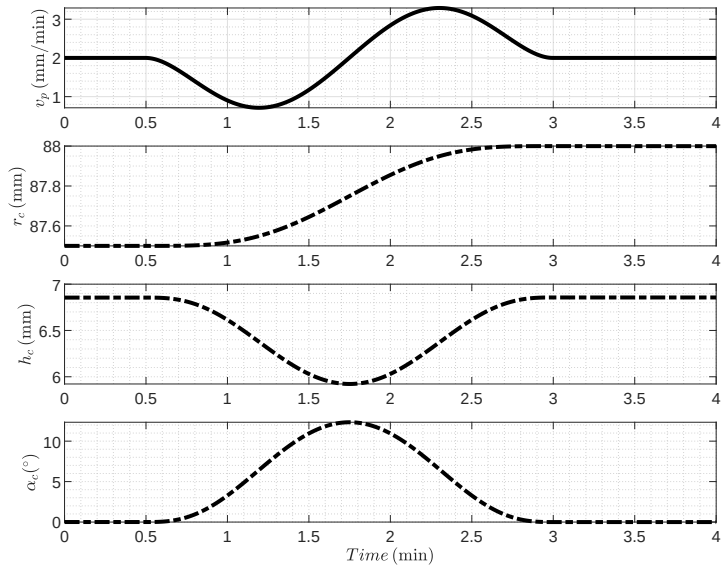

Figure 5.7: Smooth and continuous profile for the applied pulling speed (solid) and the resultant profiles (dash-dotted) for crystal radius, meniscus height and growth angle.

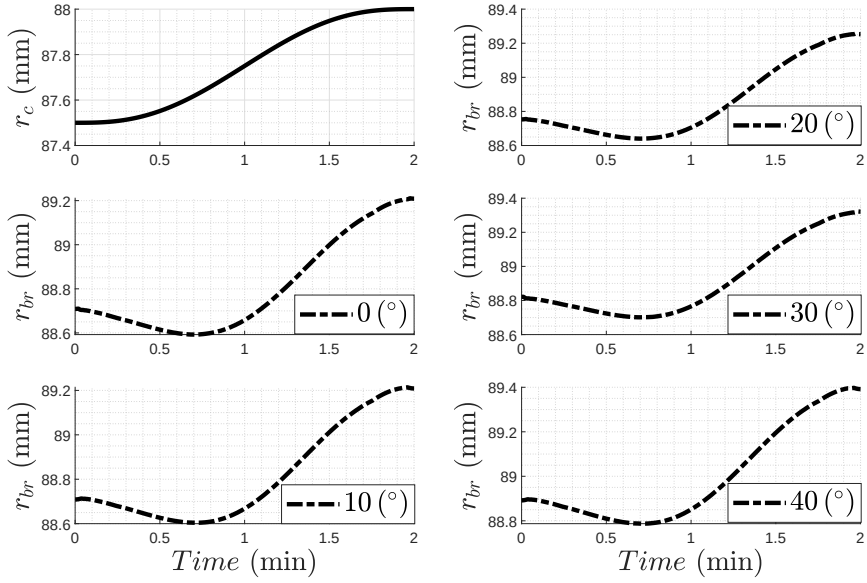

Figure 5.8: Actual crystal radius r_c (solid) v.s. bright ring signal r_{br} (dotted) measured at different azimuthal orientations, indicated respectively, at the bottom right corner of each subfigure.

the system trajectories for meniscus height (h_c) and cone angle (α_c). Furthermore, it is worth mentioning that for this particular choice of a smooth pulling speed profile, the crystal growth rate is assumed to be constant.

For a smoothly varying crystal radius profile (cf. second subfigure in Fig. 5.7), the corresponding bright ring measurement based on the ray-tracing method is carried out at various points along the highest contrast line on the 3D meniscus image. One of the aforementioned illuminated meniscus points lies in the plane of the camera (0° azimuth), while the others lie in the planes at azimuthal orientations 10°, 20°, 30° and 40° off the camera plane.

The resultant bright ring radii responses versus the expected crystal radius r_c response presented in Fig. 5.8, clearly reveal the presence of the inverse response behaviour in the measurement signal at other azimuthal orientations also.

Remark 2. *The responses in Fig. 5.8 show that there always exists a bias between the actual crystal radius and its measurement. The bias values vary as the meniscus point used for the estimate of radius changes its location to varying azimuthal orientations afar the plane of the camera. Any accidental change or slight offset in the camera position could lead to errors in the calculated radius. This should be compensated within a few runs by adjusting the bias/offset applied to the calculated radius measurement.*

Remark 3. *At the Czochralski pulling facilities, special precautions have to be adopted to ensure contamination-free crystallization environments. The facilities are therefore very clean, and dust or dirt on the camera lens should therefore not be a major problem. Moreover, the proposed radius calculation is based on a distinctive feature of the camera image, and is quite robust to the lens getting dirty.*

Since the main focus has been on understanding the inverse response and how to compensate for it, only a single point on the meniscus lying in the plane of the camera has been considered.

Chapter 6

Mitigation of Inverse Behaviour via Control

This chapter presents the linearization of hydrodynamical model to identify the presence of non-minimum phase behaviour. The linearized dynamics help to quantify the anomalous behaviour and provide a baseline for devising a control strategy. The scheme based on a parallel compensator in combination with the feedback controller is proposed for mitigating the anomalous response. Later, the scheme has been validated through nonlinear simulations while considering the effect of heater dynamics.

This chapter is based on the work presented in Bukhari et al. (2019; 2021b). It should be noted that these works (in particular (Bukhari et al. 2021b)) have been written with the intent to make results from control engineering understandable to the crystal growth community. Similarly, the author intends that the thesis should be accessible to people in the crystal growth community. For that reason, this chapter contains material that may appear trivial to control engineers, such as the detailed introduction to linearization in Sect. 6.1.

The presence of an inverse behaviour in the ingot radius estimation was determined in the previous chapter. Such an inverse response is known to pose a fundamental limitation in achievable control performance. However, for the bright ring radius measurement, the inverse response is an artifact of the measurement technique and does not appear in the physical variable one needs to control (the actual crystal radius). This chapter addresses control for the mitigation of the inverse response behaviour, using a combination of parallel compensation and feedback control. The validation of the proposed design in a nonlinear plant framework follows in the

end. Besides validating merely with the Cz growth model, this step aims particularly at assessing the overall Cz system performance in the presence of a qualitative heater model (cf. Sect. 4.2) as well. The heater model is included to qualitatively mimic the thermal variations occurring in an actual Cz process.

The nonlinear Cz dynamics expressed in Chap. 4 (cf. (4.1)) combined with the bright ring radius measurement r_{br}, constitute a nonlinear model relating pulling speed to bright ring radius. This nonlinear model comprises, in turn, of two different modes of heat transfer, referred to as *Models I & II* (cf. Sect. 4.2.1 and Sect. 4.2.2, respectively).

To remind the reader, the heat transfer from meniscus to interface in **Model I** depends on the meniscus height (cf. (4.8), (4.9) in Sect. 4.2.1), while in **Model II**, the heat transfer to the interface is independent of the meniscus height (cf. (4.13) in Sect. 4.2.2). The same holds for the growth rate since it directly depends on this heat transfer (cf. (4.1e) in Sect. 4.1).

To illustrate the difference between the two models, both models are simulated with the smooth profile for the crystal pulling rate shown in Fig. 6.1 while the heater power is kept constant. The resulting responses of the two models are depicted in Figs. 6.2 and 6.3 for models I and II, respectively.

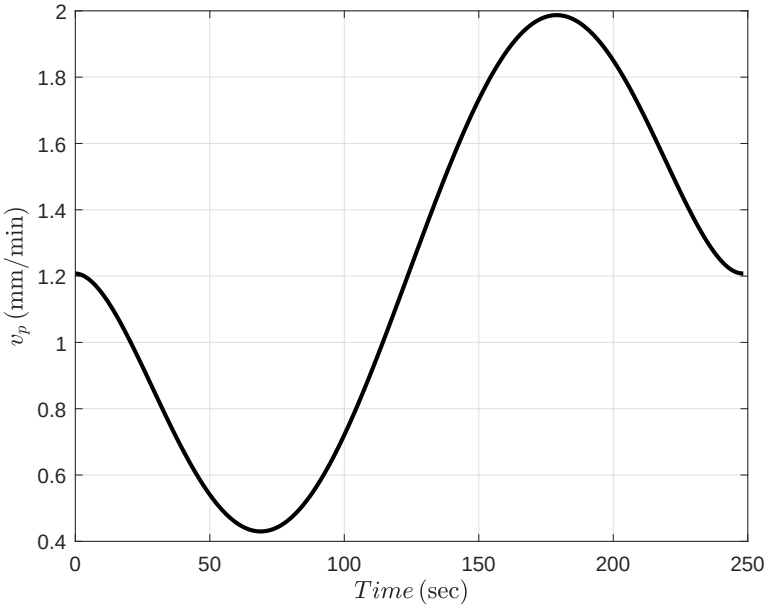

Figure 6.1: Applied pulling speed profile

It is apparent that a decrease in pulling speed causes the crystal radius to increase.

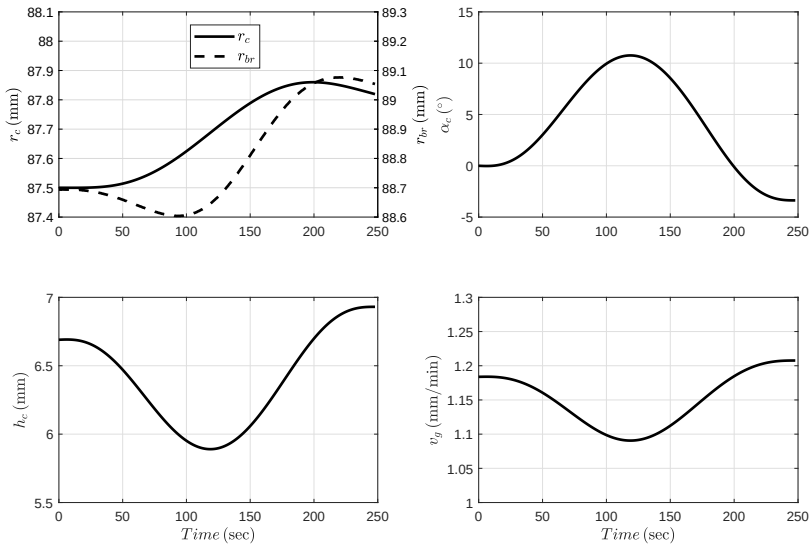

Figure 6.2: Nonlinear plant response for **Model I** subjected to the applied pulling speed input shown in Fig. 6.1, crystal radius (r_c), bright ring radius (r_{br}) and crystal growth angle (α_c) in top-left and right panes, respectively, the meniscus height (h_c) and the growth rate (v_g) in the bottom-left and right panes, respectively.

However, the measurement of crystal radius, (i.e., the estimation through bright ring radius) initially moves in an opposite direction to that of the actual crystal radius, thereby confirming the presence of inverse response (non-minimum phase behaviour). Moreover, the heat flux into the interface based on convective heat transfer (Model II) yields a constant growth rate v_g, whereas it varies with height for the case with pure conductive heat transfer across the meniscus (Model I).

6.1 Linearization of the Cz Growth Model

For any physical system, the linearization of nonlinear dynamics is nothing but the approximation of a nonlinear function of system states and inputs $f(x, u)$ with that of a linear one at a given operating point (x_0, u_0) and its small neighbourhood, i.e., $(\delta x_0, \delta u_0)$. The advantage of linearization is the use of linear analysis tools for studying the complex nonlinear dynamical behaviour in the vicinity of operating points. Since linearization is valid around an operating point (x_0, u_0), therefore the system state(s) and input(s) being sufficiently close to (x_0, u_0), yield infinitesimal weight to higher powers of $(x - x_0)$ and $(u - u_0)$ in Taylor's series expansion. Therefore, these infinitesimal terms are neglected for the linear approximation,

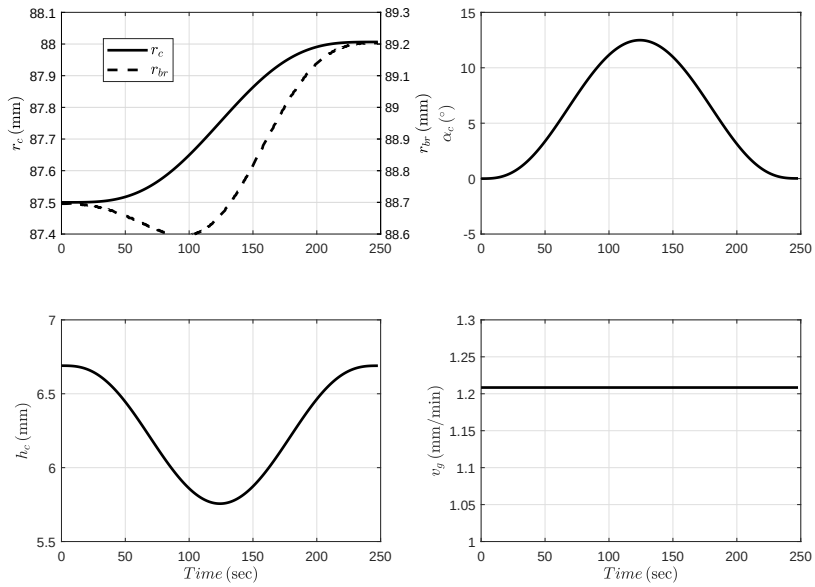

Figure 6.3: Nonlinear plant response for **Model II** subjected to the applied input shown in Fig. 6.1, crystal radius (r_c) and bright ring radius (r_{br}), crystal growth angle (α_c) in top-left and right panes respectively, the meniscus height (h_c) and the growth rate (v_g) in the bottom-left and right panes, respectively.

while retaining the first-order terms only. Thus, $f(x,u)$ can be rewritten as:

$$f(x,u) \approx f(x_0,u_0) + \left.\frac{\partial f(x,u)}{\partial x}\right|_{(x_0,u_0)} (x-x_0) + \left.\frac{\partial f(x,u)}{\partial u}\right|_{(x_0,u_0)} (u-u_0) \quad (6.1)$$

If the operating point (x_0,u_0) is chosen such that $f(x_0,u_0)=0$, then this operating point is also referred to as the equilibrium point. In connection to the Cz growth model, the nonlinear dynamics may generically be expressed as

$$\dot{\mathbf{x}} = \begin{bmatrix} \dot{r}_c \\ \dot{h}_c \end{bmatrix} = \begin{bmatrix} f_1(r_c,h_c,v_p) \\ f_2(r_c,h_c,v_p) \end{bmatrix} \quad (6.2a)$$

$$\mathbf{y} = r_{br} = g(r_c,h_c) \quad (6.2b)$$

where $f_1(r_c,h_c,v_p)$ and $f_2(r_c,h_c,v_p)$ are the right handed terms of (4.1a) and (4.1b), respectively. Keeping (6.1) in view, the first function from the set of non-

linear functions (6.2) may be expanded as:

$$\begin{aligned} f_1(r_c, h_c, v_p) = f_1(P_0) + \left.\frac{\partial f_1(r_c, h_c, v_p)}{\partial r_c}\right|_{P_0} (r_c - r_{c,0}) + \\ \left.\frac{\partial f_1(r_c, h_c, v_p)}{\partial h_c}\right|_{P_0} (h_c - h_{c,0}) + \\ \left.\frac{\partial f_1(r_c, h_c, v_p)}{\partial v_p}\right|_{P_0} (v_p - v_{p,0}) + \cdots \end{aligned} \tag{6.3}$$

where $P_0 = (r_{c,0}, h_{c,0}, v_{p,0})$ is the operating point for the linearization. Similarly, (6.2a) and (6.2b) can be expanded in the format (6.3). The complete result can be presented in the matrix notation as:

$$\underbrace{\begin{bmatrix} \dot{r}_c \\ \dot{h}_c \end{bmatrix}}_{\dot{\mathbf{x}}} = \underbrace{\begin{bmatrix} \dot{r}_{c,0} \\ \dot{h}_{c,0} \end{bmatrix}}_{\dot{\mathbf{x}}_0} + \underbrace{\left.\begin{bmatrix} \frac{\partial f_1(r_c,h_c,v_p)}{\partial r_c} & \frac{\partial f_1(r_c,h_c,v_p)}{\partial h_c} \\ \frac{\partial f_2(r_c,h_c,v_p)}{\partial r_c} & \frac{\partial f_2(r_c,h_c,v_p)}{\partial h_c} \end{bmatrix}\right|_{P_0}}_{\mathbf{A}} \begin{bmatrix} \delta r_c \\ \delta h_c \end{bmatrix} + \underbrace{\left.\begin{bmatrix} \frac{\partial f_1(r_c,h_c,v_p)}{\partial v_p} \\ \frac{\partial f_2(r_c,h_c,v_p)}{\partial v_p} \end{bmatrix}\right|_{P_0}}_{\mathbf{B}} \delta v_p \tag{6.4a}$$

$$\underbrace{r_{br}}_{\mathbf{y}} = \underbrace{r_{br,0}}_{\mathbf{y_0}} + \underbrace{\left.\begin{bmatrix} \frac{\partial g(r_c,h_c)}{\partial r_c} & \frac{\partial g(r_c,h_c)}{\partial h_c} \end{bmatrix}\right|_{P_0}}_{\mathbf{C}} \begin{bmatrix} \delta r_c \\ \delta h_c \end{bmatrix} + \underbrace{\left.\begin{bmatrix} \frac{\partial g(r_c,h_c)}{\partial v_p} \end{bmatrix}\right|_{P_0}}_{\mathbf{D}=0} \delta v_p \tag{6.4b}$$

where $\delta r_c = (r_c - r_{c,0})$, $\delta h_c = (h_c - h_{c,0})$ and $\delta u = \delta v_p = (v_p - v_{p,0})$. Moreover, the state vector derivative for small deviation about the operating point is given by $(\dot{x} - \dot{x}_0) = \delta\dot{x}$, while the output deviation about the operating point is represented as $\delta y = \delta r_{br} = (r_{br} - r_{br,0})$. Introducing the state-space matrices A, B, C & D the linearized Cz growth model as followed from expression (6.4) is given by:

$$\begin{aligned} \dot{\delta x} &= A\delta x + B\delta u \\ \delta y &= C\delta x \end{aligned} \tag{6.5}$$

The linearized model is always in terms of deviation variables δx, δu, and δy, whether mentioned explicitly or not. For the Cz growth model, there is no direct throughput term from input u to output y, i.e., the measurement only depends on the states, thereby making $D = 0$.

Both crystal growth models are linearized around a steady-state crystal radius of $87.5\,\mathrm{mm}$ and a pulling speed of $1.2\,\mathrm{mm\,min^{-1}}$. The linear models thus obtained possess right-half-plane (RHP) zero in the bright ring radius measurement transfer function, thereby confirming the non-minimum phase behaviour as discussed in Sect. 5.3. The resultant transfer function describing the linear response of the

bright ring radius R_{br} to changes in the crystal pulling rate V_p has the following general expression:

$$G(s) = \frac{R_{br}(s)}{V_p(s)} = \frac{R_{br}(s)}{R_c(s)} \cdot \frac{R_c(s)}{V_p(s)} = G_m(s) \cdot G_p(s).$$

The above transfer function is in fact a series connection of the process dynamics $G_p(s)$ between pulling speed and crystal radius $R_c(s)$ and the measurement dynamics $G_m(s)$ between the crystal radius and the bright ring radius[1] (cf. Fig. 6.4). The uppercase signals represent the complex-valued Laplace domain quantities expressed in the complex frequency variable s.

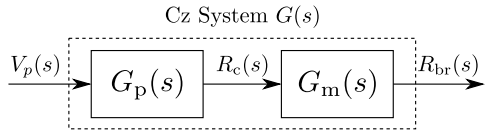

Figure 6.4: Series connection of the transfer functions describing the pulling speed to the crystal radius dynamics $G_p(s)$ and the measurement dynamics $G_m(s)$.

For model I, one has

$$G_{p,I}(s) = \frac{-0.0047626}{(s - 8.78 \times 10^{-6})\,(s + 1.684 \times 10^{-3})} \tag{6.6a}$$

$$G_{m,I}(s) = -47.1864s + 1.0041, \tag{6.6b}$$

and for model II

$$G_{p,II}(s) = \frac{-0.0048849}{(s - 4.63 \times 10^{-7})\,(s - 7.602 \times 10^{-6})} \tag{6.7a}$$

$$G_{m,II}(s) = \frac{R_{br}(s)}{R_c(s)} = -46.0050s + 1.0043. \tag{6.7b}$$

The units are omitted here for the sake of clarity. The static gain of (6.6a) and (6.7a) is in min, while that of (6.6b) and (6.7b) is unitless.

The roots of the numerator polynomial of a transfer function are called *zeros*, the roots of the denominator polynomial *poles*. These roots are real-valued or occur in complex conjugate pairs, since the coefficients of the polynomials are real. Their unit is in $\mathrm{rad\,s^{-1}}$. A system is stable if a finite perturbation in any input signal results in a finite response in all output signals. For a pole at $s = p_i$, the corresponding dynamics are stable if $\mathrm{Re}(p_i) < 0$, i.e., if the pole p_i is in the left-half-plane

[1] It is noteworthy that the transfer functions in (6.6b) and (6.7b) are not physically realizable because they contain a direct differentiation of the input signal. They only make sense when multiplied with the corresponding terms in (6.6a) and (6.7a), respectively.

of the complex plane. If $\mathrm{Re}(p_i) > 0$, the corresponding dynamics is unstable. Unstable poles are often called *Right-Half-Plane* (RHP) poles. The system is stable if all poles are in the left-half-plane. Clearly, stability (possibly through control) is a basic requirement for the operation of any system. The two models differ in their pole configuration: Model I has one RHP pole at $8.78 \times 10^{-6}\,\mathrm{rad\,s^{-1}}$, while in Model II both poles are unstable with $p_1 = 7.602 \times 10^{-6}\,\mathrm{rad\,s^{-1}}$ and $p_2 = 4.63 \times 10^{-7}\,\mathrm{rad\,s^{-1}}$.

A real-valued zero $s = z_i$ for which $\mathrm{Re}(z_i) > 0$ is called a RHP zero, and will cause an inverse response from the control input to the measurement. All RHP zeros cause fundamental limitations in achievable control performance[2]. It is apparent from (6.6b) and (6.7b) that both models have a RHP zero at $\approx 0.021\,\mathrm{rad\,s^{-1}}$, as expected based on the nonlinear simulations. The location of the right-half-plane zero is nearly independent of the heat transfer mechanism characterizing the heat flux into the interface.

The RHP zero will put an upper bound on the achievable closed-loop bandwidth for the control of crystal radius, whereas the RHP pole(s) put a lower bound on the required bandwidth (Skogestad and Postlethwaite 2007). Moreover, the RHP zero and RHP pole(s) are separated by more than three orders of magnitude, indicating that acceptable control quality should be obtainable.

In order to authenticate the linearization process, the responses of the nonlinear and linearized models are compared by exciting both nonlinear as well as linear models with the same applied input. Consequently, the input as shown in Fig. 6.1 is applied to both linear and nonlinear models, and the resultant system responses for thermal models I and II are shown in Fig. 6.5. Another comparison between the nonlinear and linear models is obtained by using the step perturbation of $1\,\mathrm{mm\,min^{-1}}$ in pulling speed to both linear and nonlinear models. The response of measured bright ring radius to the step perturbation at steady state is shown in Fig. 6.6 for the thermal model assumption I. Since the bright ring radius response to step perturbation for thermal model II is practically indistinguishable from that of thermal model I and is therefore not shown in Fig. 6.6. The close agreement between the nonlinear and linear model response, especially in the initial non-minimum phase response, confirms the validity of the obtained linear models.

Remark 4. *The Cz process, being a batch process, is inherently time-variant. One may therefore question an analysis based on linearization, due to:*

I. the change in crystal length affecting the heat transfer from the interface

[2] Also complex conjugate RHP zeros, which do not necessarily cause an inverse response, see (Skogestad and Postlethwaite 2007).

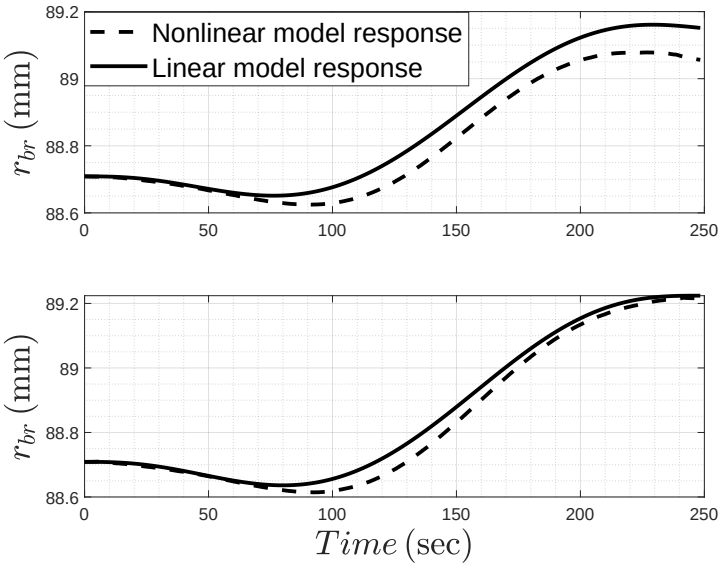

Figure 6.5: Comparison of nonlinear and linear system dynamics for thermal models I (top row) and II (bottom row), when excited by the input profile as shown in Fig. 6.1.

into the crystal.

II. *the crucible position affecting the heat transfer from surroundings to the melt.*

III. *the dropping melt level (to some extent) affecting the heat transfer from the bulk of the melt to the interface.*

However, all these changes are very slow compared to the dynamics of the inverse response (measurement anomaly). Moreover, the effects of these variations are practically minimized by an appropriate temperature feedforward trajectory. Therefore, it is reasonable to use linearization when investigating the inverse response dynamics and when designing a controller for crystal radius control. A brief further discussion is provided in Chap. 8.

6.2 Design of a Parallel Compensator and Feedback Controller

This section presents the design of a parallel compensator and stabilizing controller based on the linear models derived in Sect. 6.1.

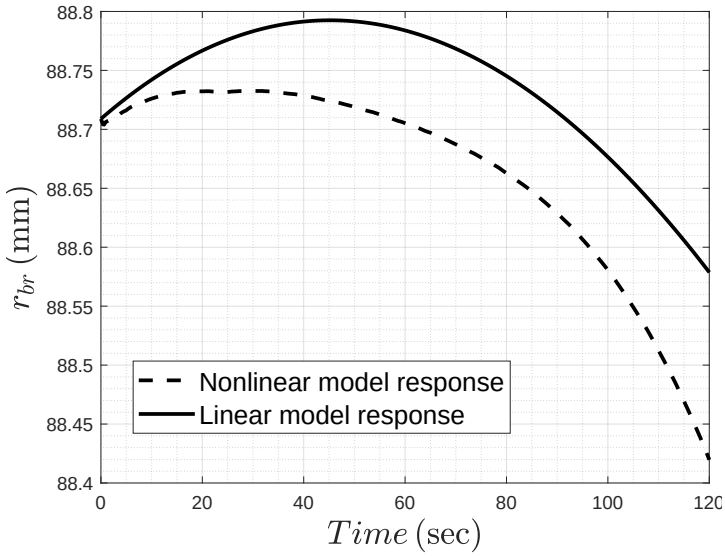

Figure 6.6: Comparison of nonlinear and linear system dynamics for thermal model I, when excited by step perturbation in v_p.

6.2.1 Basic feedback controller design

Feedback control is the most common type of control, illustrated in Fig. 6.7. This basic feedback schematic diagram shows a measurement $Y(s)$ being affected by a disturbance $V(s)$ through the dynamics $G_d(s)$ and by the control input $U(s)$ through the dynamics $G(s)$. The measurement signal $Y(s)$ is *fed back* and compared with its reference/ desired value $R(s)$ such that the difference, alternatively called error $E(s)$, is used as an input to the controller $K(s)$, which in turn calculates the control signal $U(s)$.

Feedback control is a remarkably powerful concept. It can stabilize unstable systems, i.e. moving the unstable system poles to the left half of the complex plane, and provide good performance, for example, a quick response of $Y(s)$ to changes in $R(s)$, no or only limited overshooting of $Y(s)$ and effective disturbance rejection. However, it is not without caveats. In particular, poorly designed feedback control may also cause instability, even for systems $G(s)$ which are stable on their own. Furthermore, and most important for the Cz growth model, system zeros are unaffected by feedback.

A common way to determine suitable parameters of the controller is to utilize the frequency response $L(j\omega) = K(j\omega)G(j\omega)$ of the so-called *open-loop* system plotted in a Bode diagram.

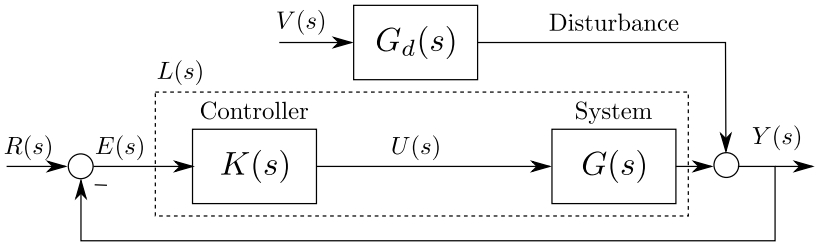

Figure 6.7: Illustration of a simple feedback control system with the transfer function $G(s)$ of the system to be controlled, the transfer function $K(s)$ of the controller and the transfer function of the disturbance model $G_d(s)$.

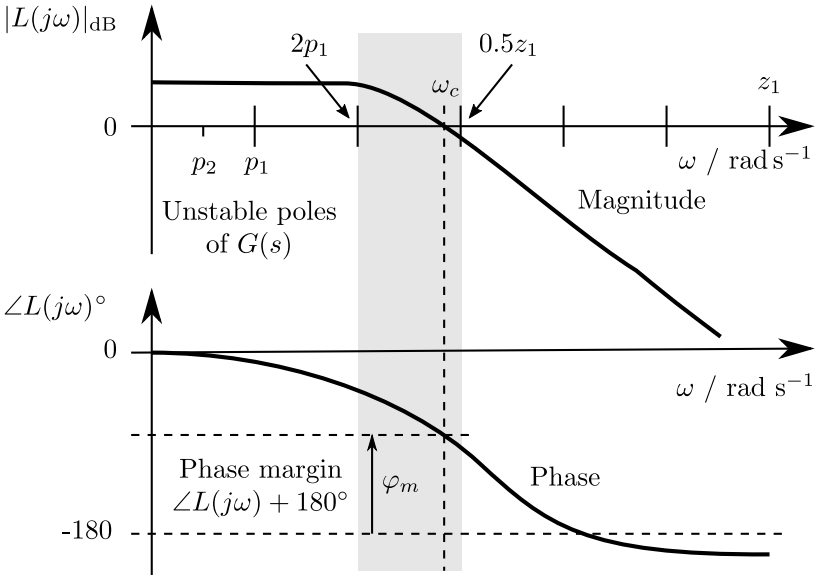

Figure 6.8: Simplified sketch of a Bode diagram illustrating the frequency response of the open-loop system with $L(s) = K(s) \cdot G(s)$ and $s = j\omega$. The frequency axis is drawn in a linear scale for the sake of simplicity. The transfer function $G(s)$ of the system to be controlled is assumed to have two RHP poles denoted by p_1, p_2 (among other stable poles) and one RHP zero denoted by z_1. For a stable closed-loop system showing acceptable performance the crossover frequency ω_c should be roughly within the grey region and the phase margin φ_m must be positive.

An illustrative example of the Bode diagram is shown in Fig. 6.8. The Bode diagram comprises of two plots, the first showing the magnitude $|L(j\omega)|$ of the open-loop system depending on the frequency ω and the second one showing the phase of $L(j\omega)$.

A well-designed feedback control system will have an open-loop frequency re-

sponse with large magnitude at low frequencies, but small magnitude at high frequencies. Let ω_c denote the *crossover frequency*, i.e., the frequency where $|L(j\omega_c)|_{\text{dB}} = 0$. Assume that $|L(j\omega)|_{\text{dB}} > 0 \ \forall\omega < \omega_c$, and $|L(j\omega)|_{\text{dB}} < 0 \ \forall\omega > \omega_c$. Then, the so-called Bode stability criterion states that the *phase margin* $\varphi_m = 180^\circ + \angle L(j\omega_c)$ *must* be positive. Although some sources present the Bode stability criterion only for open-loop stable systems, it can also be applied to open-loop unstable systems – as the Cz system under discussion – provided the number of open-loop unstable poles is known and the steady-state phase is adjusted accordingly. Each RHP pole contributes a phase of -180° at $\omega = 0$. A small phase margin indicates that the system may become unstable for a small error in the system model, and is also an indication of poor performance, e.g., large overshoots and/or severe oscillations. Most control engineers will insist on a phase margin of at least 45°.

Additional criteria can be utilized to improve closed-loop performance: For example, as a rule of thumb, ω_c should be at least twice as large as the *fastest unstable pole* to ensure that any unstable dynamics is properly 'caught'. In the case of non-minimum phase systems – as discussed here – another restriction comes into play: ω_c should be about less than half the *slowest zero* so the controller action is not dominated by any inverse response. Clearly, the last two requirements show that the presence of a RHP zero will introduce a typical conflict of objectives imposing fundamental limitations on achievable performance for feedback control. An extensive exposition of these issues can be found in (Skogestad and Postlethwaite 2007), where further details, more precise statements and theoretical justification can be found.

Coming back to the Cz system, for Model II, the required crossover frequency will be determined mainly by the faster RHP pole (the one furthest from the origin in the complex plane). The faster RHP pole $7.602\text{e}^{-6}\,\text{rad}\,\text{s}^{-1}$ in Model II is similar to the RHP pole $8.78\text{e}^{-6}\,\text{rad}\,\text{s}^{-1}$ of Model I. Therefore, the control limitations of the two models are similar, even though the number of unstable poles is different. Further details can be found in (Bukhari et al. 2019).

6.2.2 Basics of parallel compensator design

Parallel compensation will affect RHP zeros, and can be used to move RHP zeros into the left-half-plane (Skogestad and Postlethwaite 2007). The compensated system (plant + parallel compensator) will then have both the poles of the original system and the poles of the parallel compensator.

***Note**: Following the completion of the design of the parallel compensator, the possibility of shifting the RHP zeros to the left-half-plane by the parallel compensator will be more obvious (cf. the second column of Table 6.2).*

Several authors have proposed combining feedback control with parallel compensation, thereby enabling the latter to remove the limitation in performance for feedback control. Such a schematic, with combined feedback and parallel compensator, is illustrated in Fig. 6.9. Here, a parallel compensator $G_{pc}(s)$ is designed to ensure that the transfer function from the input $U(s)$ to the compensated signal $Z(s) = Y(s) + Y_{pc}(s)$ does not possesses any RHP zero to limit the performance of feedback control.

Unfortunately, in most physical systems with a control configuration such as that depicted in Fig. 6.9, the use of parallel compensation is not of much value. This is because despite achieving good control of $Z(s)$, the physical variable $Y(s)$, of interest, cannot be alleviated of the undesired effects of the RHP zero(s).

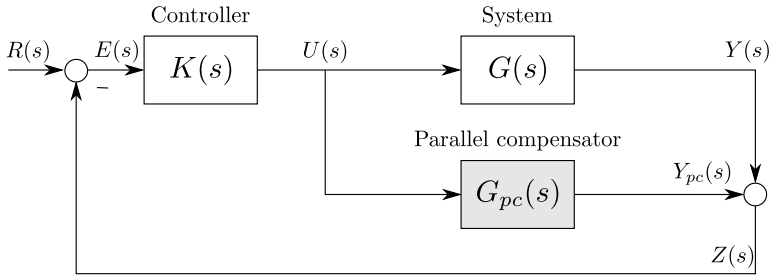

Figure 6.9: Feedback control combined with parallel compensation to remove performance limitations for feedback control caused by RHP zeros.

However, as observed in Figs. 6.2 and 6.3, the inverse response in the Cz process is merely associated with the camera-based *measurement* of the ingot radius, whereas the *actual crystal radius* is independent of inverse behaviour. This opens an opportunity for using parallel compensation to enable improved control of the crystal radius r_c, even though the control of the measurement r_{br} is not improved.

6.2.3 Compensator design

In the following, the design of a parallel compensator specific for the Cz process is described. Instead of using generic time-/ Laplace-domain symbols $r(t)/R(s)$, $u(t)/U(s)$ and $y(t)/Y(s)$ as in Fig. 6.9 the symbols specific to the Cz process will be used henceforth.

Fig. 6.10 shows a complete system block diagram that includes both the compensator and the controller connected respectively in parallel and cascade with the plant.

The controller block marked as $K(s)$ in Fig. 6.10 is the Automatic Diameter Controller (ADC). The parallel compensator used is a stable approximation of the ideal

compensator with transfer function $G_{pc}(s)$ augmented by a high pass filter with transfer function $G_{hpf}(s)$. The need for both, the stable approximation and the high pass filter, will be explained later. The following two design requirements need to be met:

1. It is desired to keep the dynamics of the compensated measurement as close as possible to that of the actual crystal radius, i.e., $\tilde{R}(s) \approx R_c(s)$.
2. The practices in the Cz industry rely on using the camera-based measurement, followed by simply applying a bias to the measurement signal. By this approach, they obtain the true *steady-state* crystal radius from the camera measurement. The compensator design should allow the industry to continue applying the same bias to the compensated measurement $\tilde{R}(s)$. Hence, the compensator obtained in step 1 needs to be modified appropriately.

Under these conditions the compensator – based on model I – can be designed as follows: Ignoring (for now) the high pass filter $G_{hpf}(s)$ in Fig. 6.10, the dependency of $\tilde{R}(s)$ on $V_p(s)$ gives

$$\tilde{R}(s) = \big(G_m(s)G_p(s) + G_{pc}(s)\big)V_p(s) = G_{\tilde{r}}(s)V_p(s). \tag{6.8}$$

Hence, the ideal parallel compensator can be derived as follows:

$$\begin{aligned} G_{\tilde{r}}(s) &\overset{!}{=} G_p(s) \\ G_p(s)G_m(s) + G_{pc}(s) &= G_p(s) \\ \Leftrightarrow \qquad G_{pc}(s) &= G_p(s)\left(1 - G_m(s)\right) \end{aligned} \tag{6.9}$$

It is apparent that the ideal parallel compensator as given in (6.9) would contain the same poles as the plant model $G_p(s)$, including the unstable pole(s)[3]. Any system that consists of two parallel branches, having identical unstable dynamics with common input and output, will not be stabilizable by feedback as it will necessarily possess hidden unstable mode(s) Skogestad and Postlethwaite (2007). It is, therefore, necessary to find a stable approximation to the ideal parallel compensator $G_{pc}(s)$, i.e., an approximation that removes the RHP zero, but does not destabilize the control loop.

Remark 5. *Though the schematic configuration depicted in Fig. 6.10 resembles that of* internal model control *(IMC), however the two are completely different*

[3]This will be illustrated in the summary of the overall design (cf. second column of Table 6.2).

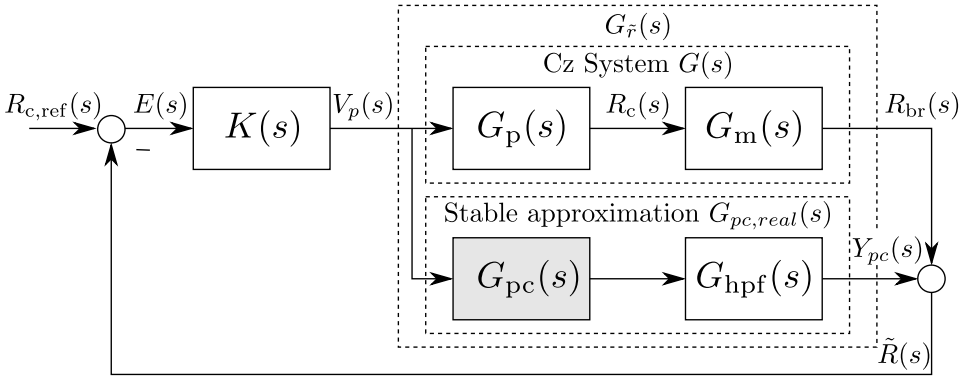

Figure 6.10: Basic block diagram of the feedback controlled Cz system split into the pure plant model $G_p(s)$ and the bright ring measurement model $G_m(s)$ together with a parallel compensator. The ideal parallel compensator $G_{pc}(s)$ is augmented by a high pass filter G_{hpf} according to the procedure described in Sect. 6.2.3. What is implemented in the real system is the stable approximation of $G_{pc}(s)G_{hpf}(s)$.

in essence. The IMC configuration instead places the plant model in parallel with the process and only feeds back the difference between the two (Garcia and Morari 1982, Seborg et al. 2010). The IMC approach is not viable in this case as it would cause unobservable unstable states in the overall (compensated) dynamics, meaning that the closed-loop would not be internally stable.

In this case, the frequency of the RHP zero is higher than the frequencies of the RHP pole(s) (cf. Sect. 6.1). Hence, the main interest is to have a good approximation of the system at high frequencies to remove the effects of the RHP zero. The unstable dynamics are therefore suppressed by augmenting $G_{pc}(s)$ with a high pass filter $G_{hpf}(s)$, designed to cut off frequencies significantly below the frequency corresponding to the RHP zero. With the RHP zero at $\approx 0.021\,\mathrm{rad\,s^{-1}}$ the transfer function $G_{hpf}(s)$ of the high pass filter is chosen as

$$G_{hpf}(s) = \frac{5000\,s}{5000\,s + 1} \tag{6.10}$$

with the cutoff frequency at $2 \times 10^{-4}\,\mathrm{rad\,s^{-1}}$.

Then, a stable/unstable decomposition is performed on the augmented parallel compensator. This means that the transfer function $G_{pc}(s)G_{hpf}(s)$ is split into two transfer functions connected in parallel, one containing the stable dynamics, while the other, the unstable dynamics. Since the unstable dynamics are slow, the augmentation of the high pass filter makes the unstable part smaller compared to

the stable part[4]. Hence, it is reasonable to use only the stable part of this decomposition in the final implementation.

Finally, design requirement 2 has to be met. The stable part of the decomposition is therefore adjusted to have zero steady-state gain such that $\tilde{R} = R_{br}$ in a steady state. One ends up with the following parallel compensator transfer function for model I

$$G_{pc,real}(s) = \frac{Y_{pc}(s)}{V_p(s)} = \frac{-0.22517s}{(s + 1.684 \times 10^{-3})(s + 2 \times 10^{-4})}. \tag{6.11}$$

Remark 6. *Following points are relevant when considering whether to implement the proposed control scheme:*

I. The parallel compensator is the only change from the conventional control structure.

II. The high pass filter means that the low frequency/ slow dynamics of the actual system remain unchanged.

III. The proposed new control is therefore a minor change that should be acceptable for operators.

6.2.4 Controller design

The design of a stabilizing feedback controller follows the compensator design. A PID controller is used in this work because it is easy to implement in the existing industrial control setup. The PID controller, represented by $K(s)$ in a series/interacting form is given by

$$K(s) = \frac{K_p\,(T_i s + 1)\,(T_d s + 1)}{T_i s\left(1 + \frac{T_d s}{N}\right)} \tag{6.12}$$

The tuned parameters for the PID controller and the resulting crossover frequency are given in Table 6.1.

[4]The optimal approximation of an unstable system by a stable system can be found using the so-called Nehari extension (Zhou et al. 1996). However, the Nehari extension approximation would distribute the error over all frequencies.

Table 6.1: Parameters of the PID controller $K(s)$

Proportional gain (K_p)	$0.01\,\mathrm{s}^{-1}$
Integral Time const. (T_i)	$5000\,\mathrm{s}$
Derivative Time const. (T_d)	$650\,\mathrm{s}$
Filter coefficient (N)	100
Crossover frequency (ω_c)	$0.032\,75\,\mathrm{rad\,s}^{-1}$

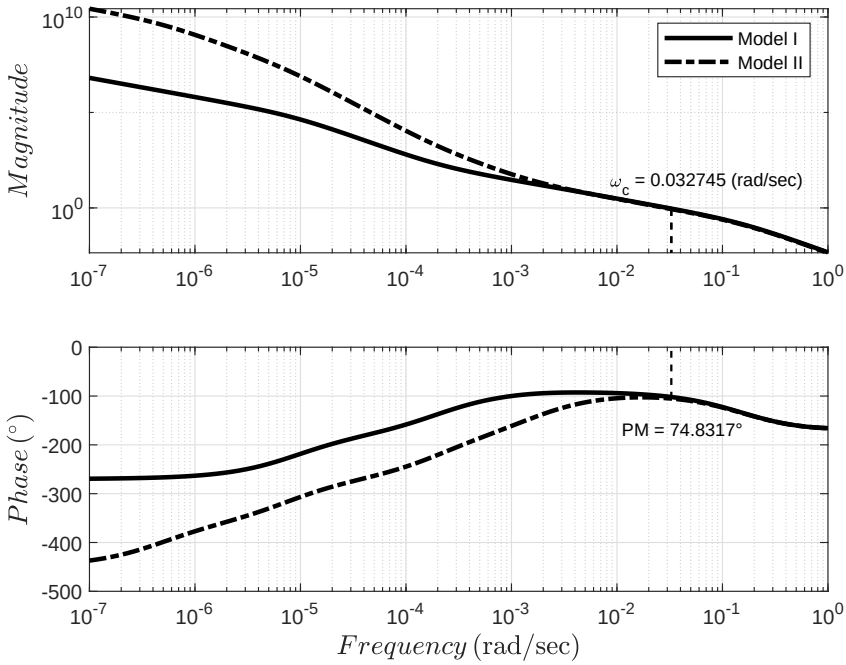

Figure 6.11: Frequency response of the compensated plants (models I and II) with a feedback controller.

The achieved crossover frequency $\omega_c \approx 0.032\,75\,\mathrm{rad\,s}^{-1}$ is much higher than half of the zero at $\approx 0.02\,\mathrm{rad\,s}^{-1}$ which would have been the limiting factor in control design without parallel compensation. So the limitations imposed by the RHP is quite clearly mitigated and a higher system bandwidth is achieved. The frequency response in Fig. 6.11 shows that the proposed PID controller with the compensator stabilizes both models, as the phase margin of the compensated plant is around $74°$ for both models.

***Note**: The location of poles and zeros for the closed-loop system (cf. Table 6.2)*

indicates that both stability and mitigation of the inverse response have been achieved successfully.

Table 6.2: Location of poles and zeros for plant, plant with compensator (compensated dynamics) and closed-loop system

Plant model $G_m(s)G_p(s)$		**Compensated system** $G_{\tilde{r}}(s)$		**Closed-loop system**	
$(\mathrm{rad\,s^{-1}})$		$(\mathrm{rad\,s^{-1}})$		$(\mathrm{rad\,s^{-1}})$	
Zero(s)	Pole(s)	Zero(s)	Pole(s)	Zero(s)	Pole(s)
2.128×10^{-2}	-1.684×10^{-3}	-2.02×10^{-4}	-2×10^{-4}	-10.75	-1.863×10^{-1}
	8.78×10^{-6}	-10.75	-1.684×10^{-3}	-1.999×10^{-3}	-1.334×10^{-2}
			8.78×10^{-6}	-2.02×10^{-4}	-2.067×10^{-3}
				-2.0×10^{-4}	-2.047×10^{-4}
					-2.0×10^{-4}

6.3 Closed-loop Performance

The compensator and the controller are designed on the basis of a linearized Cz growth model, i.e., **Model I**, as presented by $(G_{p,I}(s)\cdot G_{m,I}(s))$ (cf. (6.6a) and (6.6b) in Sect. 6.1). Moreover, the overall performance of the designed compensator and controller is found equally satisfactory when tested in both linear and nonlinear simulation environment for both model assumptions.

The closed-loop testing of nonlinear Cz growth dynamics, in the presence of both parallel compensator and the feedback controller (K), is schematically illustrated in Fig. 6.12.

In Fig. 6.12, $\delta\, v_p$ and $\delta\, r_{br}$ are the deviation variables, whereas v_{po} and r_{br0} are the steady-state values (points at which linearization was performed) such that the input to and the output from the nonlinear Cz dynamics are $v_p = v_{po} + \delta\, v_p$ and $R_{br} = r_{br0} + \delta\, r_{br}$, respectively.

In order to determine the extent to which the nonlinearities in the Cz system may be excited, the responses to two different crystal radius reference trajectories are simulated.

In the first case, referred to as (**case-A**) in Fig. 6.13, the response to a smooth reduction in the crystal radius reference of $2.5\,\mathrm{mm}$ is simulated. In the second case (**case-B**), a scaled version of the same smooth crystal radius reference trajectory is applied, changing the reference by $0.5\,\mathrm{mm}$. In Fig. 6.13, the responses of **case-B** are scaled by a factor of 5 to make them easily comparable to the responses of **case-A**. Fig. 6.13 show that the system

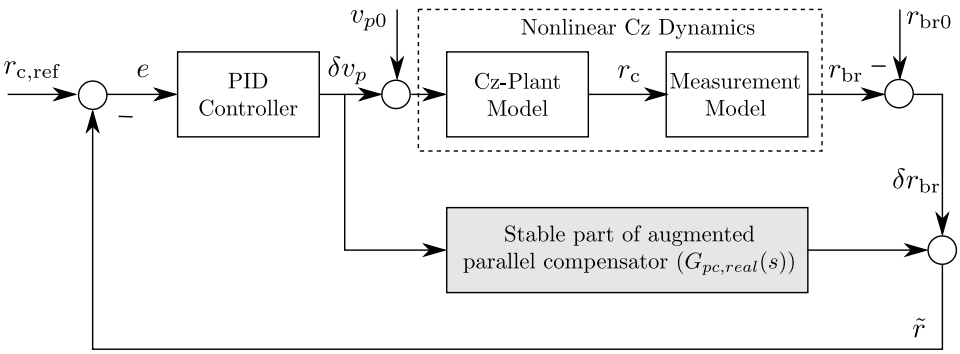

Figure 6.12: Block diagram for the closed-loop testing of nonlinear Cz growth dynamics.

with the proposed control is relatively insensitive to nonlinearities for smooth reference changes of reasonable magnitude.

6.4 Responses to Temperature Disturbances

Hitherto, the simulated growth rate variations did not take temperature dynamics into account. However, temperature variations are a major source of disturbances to the crystal growth rate and thereby also to the crystal radius control. To assess control performance in the presence of growth rate variations caused by temperature disturbances, the overall Cz model (with both growth and temperature dynamics) needs to be used. A qualitative heater model augmented with the crystal growth dynamics has been presented in Sect. 4.2. Thus, in the following, the overall Cz dynamics (both the growth model as well as heater model) are under the combined influence of the two system inputs, i.e., pulling speed v_p and heater input Q_H.

6.4.1 Temperature effects on the overall system performance

During a typical growth cycle in the body stage, a feedforward temperature (target temperature) trajectory is applied to the temperature controller to compensate for the slow temperature dynamics. In an actual process, the temperature feedforward trajectory has an increasing trend (typically in the range of $\approx 0.1\,\mathrm{K\,min^{-1}}$) to compensate for the following phenomena occurring throughout the growth cycle within the Cz growth chamber:

- A gradual uplift of the crucible, therefore progressively reducing the crucible exposure to the heaters.
- With the ongoing crystallization, the crystal continues to protrude into the colder areas above the heat shield, thereby increasing the heat transfer away from the interface.

The perfect temperature feedforward trajectory is hard to establish, due to effects such as aging and continual replacement of components in the hot zone, variations between pullers, etc. An imperfect temperature trajectory will act as a disturbance to the crystal growth rate and hence also affects the crystal radius control. Note that the heater model

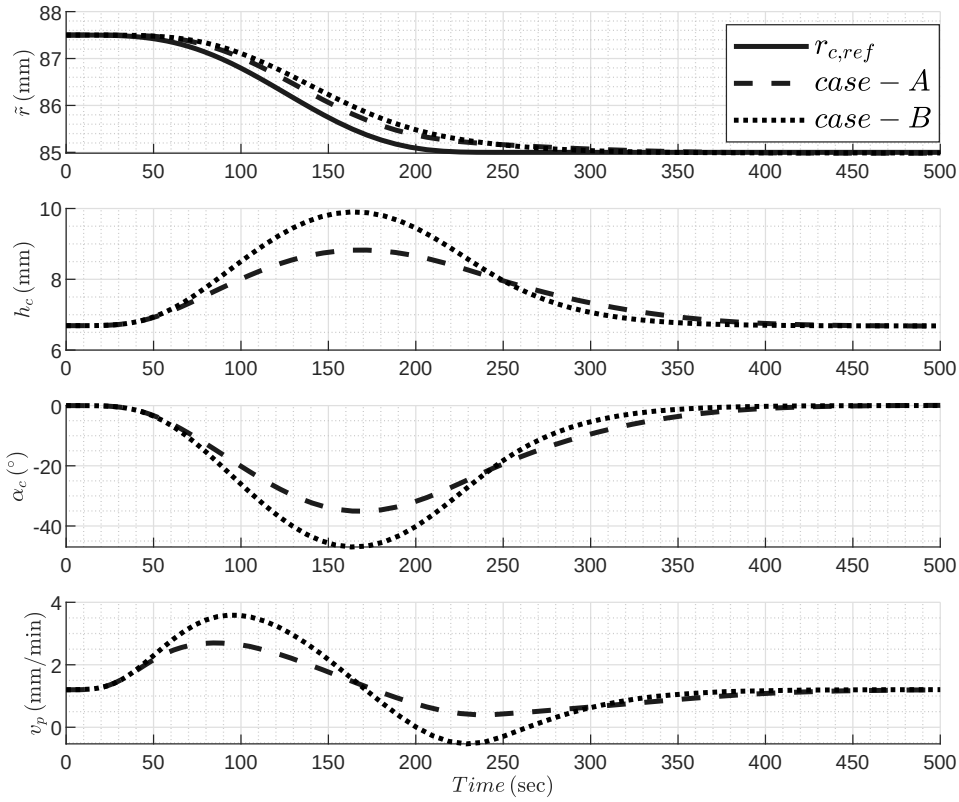

Figure 6.13: Comparison of system responses to $r_{c,ref}$ with large amplitude change (case-A) and small amplitude change (case-B: *responses are scaled up by a factor of 5*). Top row: compensated measurement $\tilde{r}$, second row: meniscus height h_c, third row: cone angle α_c, last row: control input v_p.

in this work is qualitative, and therefore does not include the afore-mentioned phenomena causing a need for an increasing feedforward trajectory under actual growth conditions. However, effects of an imperfect temperature trajectory can be simulated[5], since changes to the temperature controller reference will affect the melt temperature in the model and hence also affect the crystal growth rate. That is, in our simulation on the simplified model, the temperature feedforward trajectory does not represent the actual feedforward trajectory, but rather the error in the feedforward trajectory in an actual plant.

To investigate the effects of temperature disturbances on crystal radius control, the reference for temperature T_1 is increased linearly (at the rate of $0.5\,\mathrm{K\,min^{-1}}$). The linear increase in temperature T_1, sensed by the pyrometer, qualitatively mimics the variation in the target temperature trajectory. Compared to the typical difference between the actual and the ideal feedforward trajectory, the simulated feedforward trajectory must be consid-

[5]High accuracy not claimed here though.

ered to represent a rather strong disturbance. The resultant responses for temperatures in different lumped volumes (cf. Fig. 4.1 in Sect. 4.2) is shown in Fig. 6.14. These temperature changes, in turn, affect the radii responses (r_c, r_{br}, $\tilde{r}$) via variation in growth rate v_g.

For the given change in heater setpoint trajectory as depicted in top pane of Fig. 6.14, the resulting system responses at the crystallization growth interface are shown in Figs. 6.15 and 6.16 for models I and II, respectively.

It is apparent from the radii responses (cf. Figs. 6.15 and 6.16) that the designed controller and parallel compensator have successfully overcome the temperature variations leading to a change in the growth rate, and that the resulting variation in crystal radius is small.

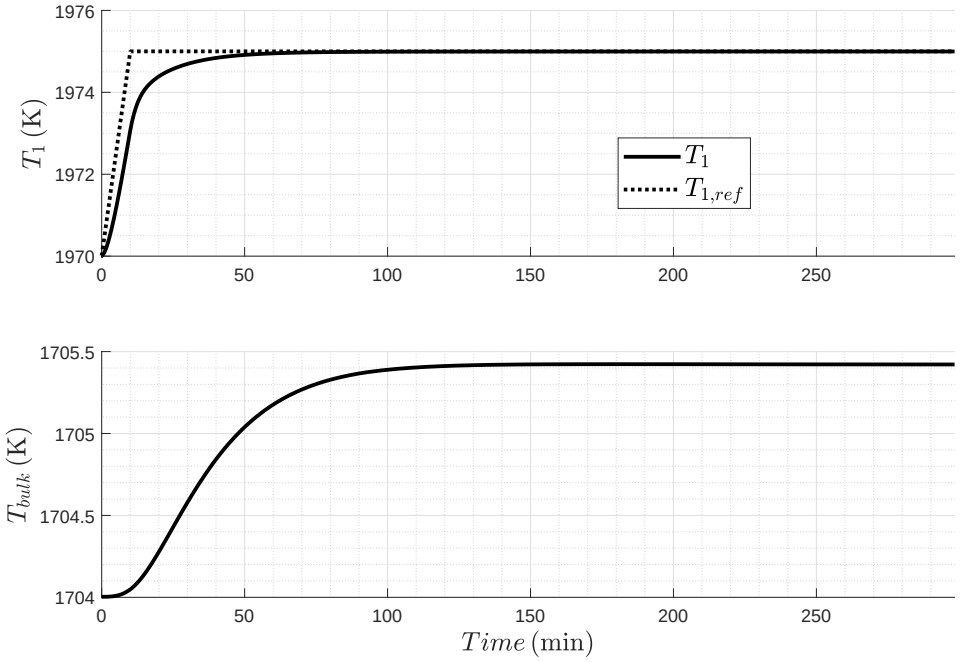

Figure 6.14: Temperature responses for model I. Top pane: temperature sensed by the pyrometer T_1 versus the target temperature trajectory $T_{1,ref}$. Bottom pane: temperature of the bulk T_{bulk} of the melt contained within the crucible.

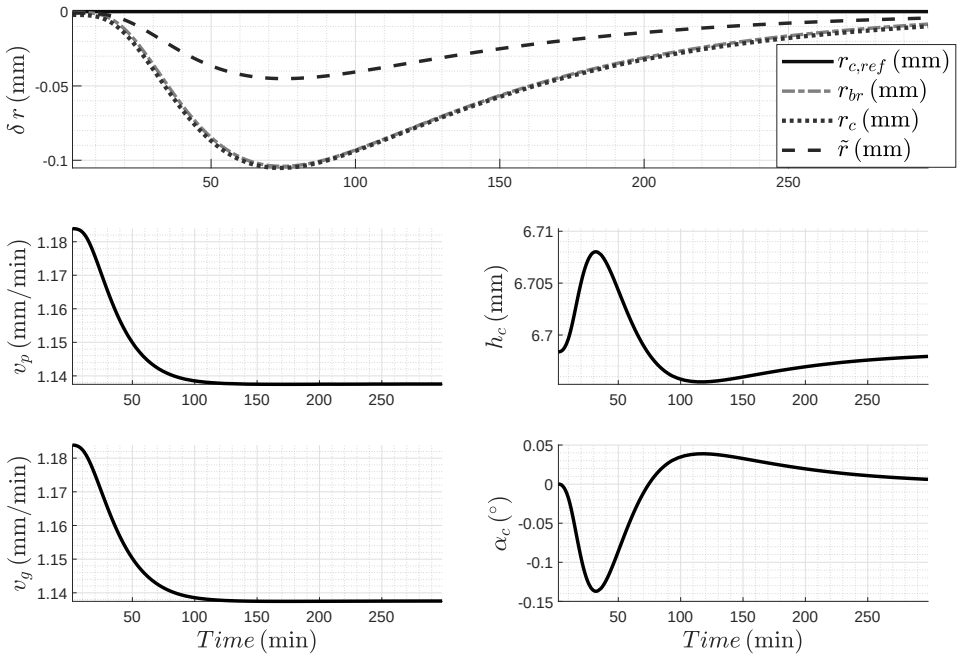

Figure 6.15: Closed-loop responses for model I with a change in temperature setpoint trajectory shown in Fig. 6.14. Top row: crystal radius r_c, compensated measurement $\tilde{r}$ and bright ring radius measurement r_{br} versus constant $r_{c,ref}$. Middle row (left $\rightarrow$ right): control input v_p and meniscus height h_c. Bottom row (left $\rightarrow$ right): growth rate v_g and growth angle α_c.

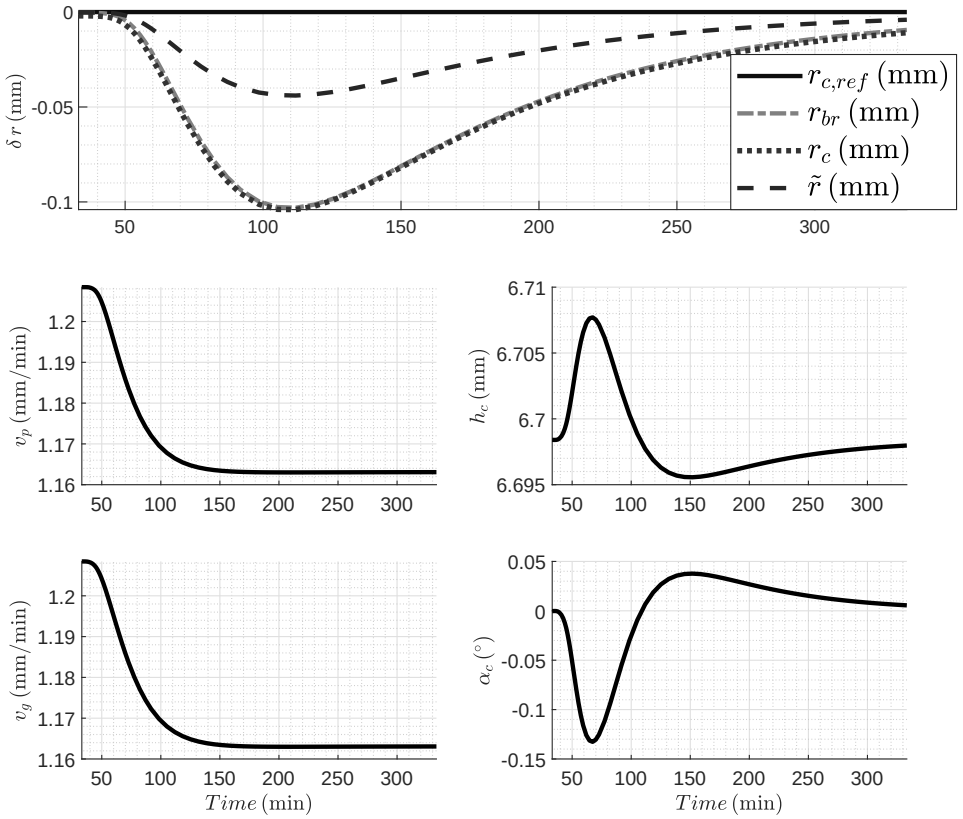

Figure 6.16: Closed-loop responses for model II with a change in temperature setpoint trajectory shown in Fig. 6.14. Top row: crystal radius r_c, compensated measurement $\tilde{r}$ and bright ring radius measurement r_{br} versus constant $r_{c,ref}$. Middle row (left $\rightarrow$ right): control input v_p and meniscus height h_c. Bottom row (left $\rightarrow$ right): growth rate v_g and growth angle α_c.

Chapter 7

Iterative Learning Control for the Czochralski Process

The work presented in this chapter utilizes nonlinear second-order sliding mode (SOSM) combined with an iterative learning control (ILC) scheme for the diameter control of the Czochralski (Cz) process.

This chapter is adapted from the work presented in Bukhari et al. (2017). However, the simulation results have been updated slightly from the published results.

The sliding mode control (SMC), aka variable structure control (VSC), is well suited for systems with bounded and unstructured parametric uncertainties. The SOSM is therefore employed to attain robustness in the control despite unknown system dynamics. On the other hand, iterative learning control is incorporated as an intelligent module of the designed controller to better adapt to repetitive operation even in the presence of unknown parameters and bounded disturbances. Since Cz is a batch process that repeats itself every time a new crystal ingot is produced, repeatability renders learnability to the designed controller.

The actual dynamics of the Cz process are highly complex and nonlinear. Although complex dynamic models attempting to capture these complexities do exist, their use is limited to offline simulation studies, as the lack of online measurements prohibits reliable updating of such models to actual operating conditions. In addition to the above, the parameters of such mathematical models would be subject to wide variations owing to non-uniform and unpredictable thermal conditions, wear and aging of puller equipment, and hot zone parts. This work employs control of interface dynamics that are known accurately for the given crystal and hot zone geometry while assuming steady-state thermal conditions within the melt.

The robust ILC design to compensate for the model errors and the repetitive external dis-

turbances is a hot research topic. To address this, traditional ILC has been integrated with many well-established control techniques like adaptive robust control, backstepping control (Rahmanpour and Hovd 2012), H_∞ control, and sliding mode control.

In a nutshell, the changing system heat fluxes at the melt/crystal interface can be expressed as uncertainties in the system, which directly influence the crystallization process, thereby affecting the crystal diameter. These changing heat fluxes have a strong repetitive component, due to the repetitive nature of puller operation, and their effect on crystal diameter and pulling speed can therefore be learned by an ILC controller. An adaptive control approach based on SOSM and ILC has been designed for diameter tracking in the Cz process. The motivation for adaptive control is to account for batch-related variations in operating conditions as well as to compensate for slowly time-varying system parameters that are susceptible to changes owing to gradual system wear.

7.1 Dynamics Governing the Melt/Crystal Interface

The dynamics at the crystallization interface have been discussed in Sect. 4.1. However, the only difference in the ILC-SOSM scheme is the use of a different second state equation, i.e., $\dot{\alpha_c}$ (cf. (7.1)) instead of $\dot{h_c}$ (cf. 4.1b). The two representations model the same dynamic behaviour, though.

The meniscus is produced as a result of gravitational forces and surface tension. Its upper end is the interface/phase boundary between molten and solid Si, where the crystallization takes place, thereby releasing latent heat of fusion. Since the crystal is pulled upwards into colder regions of the furnace, a temperature gradient is established which leads to heat flow by conduction from the hot interface into the colder crystal. By this mechanism, crystallization is maintained throughout the growing process. The overall hydromechanics at the interface are expressed in terms of system states ($\dot{r_c}$ and $\dot{\alpha_c}$) that are related mathematically through the following expressions (Winkler et al. 2010c):

$$\begin{aligned} \dot{r_c} &= v_g \, \tan(\alpha_c) \\ \dot{\alpha_c} &= \frac{v_p - v_{cru} - C_{\alpha,z}\, v_g}{C_{\alpha,n}} \end{aligned} \tag{7.1}$$

where v_{cru} is the crucible lifting rate, v_g is the crystal growth rate and the factors $C_{\alpha,z}$ and $C_{\alpha,n}$ are defined as:

$$\begin{aligned} C_{\alpha,z}(r_c, \alpha_c) = 1 - \frac{\rho_s r_c^2}{\rho_l R_{cru}^2} + \Bigg[\left(1 - \frac{r_c^2}{R_{cru}^2}\right) \frac{\partial h_c}{\partial r_c} \\ - \frac{2 r_c h_c}{R_{cru}^2} - \frac{a^2}{R_{cru}^2} \cos(\alpha_0 + \alpha_c) \Bigg] \tan(\alpha_c) \end{aligned} \tag{7.2}$$

$$C_{\alpha,n}(r_c, \alpha_c) = \left(1 - \frac{r_c^2}{R_{cru}^2}\right) \frac{\partial h_c}{\partial \alpha_c} + \frac{r_c a^2}{R_{cru}^2} \sin(\alpha_0 + \alpha_c) \tag{7.3}$$

where the growth angle $\alpha = \alpha_0 + \alpha_c$ is the angle between the line tangent to the meniscus surface at the melt-crystal interface and the lateral surface of the growing crystal. The

angle α_c determines the growth direction and thereby the dynamics of the crystal diameter, whereas α_0 is the characteristic wetting angle of a specific material. The manipulating input is $u = v_p$.

Finally, the crystal growth rate v_g is expressed as (Winkler et al. 2010a):

$$\begin{aligned} v_g &= \frac{\mathbf{\Phi}_s - \mathbf{\Phi}_l}{A_i \rho_s \Delta H} = \frac{\phi_s - \phi_l}{\rho_s \Delta H} \\ &= \frac{1}{\rho_s \Delta H} \big(k_s \Delta T_s - k_l \Delta T_l \big) \end{aligned} \tag{7.4}$$

Here ρ_s is the density of the solid at melting point temperature, ΔH is the latent heat of fusion per unit volume, $k_{s,l}$ are thermal conductivities of crystal and melt respectively, A_i is the area of cross-section at the interface, $\mathbf{\Phi}_l = k_l A_i \Delta T_l$ is the heat flow from the melt to the interface while $\mathbf{\Phi}_s = k_s A_i \Delta T_s$ is the heat flow from the interface to the crystal. A necessary condition for growth is that the growth rate is positive, i.e. the heat flux/heat flow is directed from the melt into the crystal, i.e., ϕ_s is greater than ϕ_l. Otherwise, the sign of v_g reverses, thereby rendering the crystallization to stop and remelting the crystal. The two quantities $\phi_{s,l}$ are heat fluxes per unit area expressed in $[W/m^2]$.

7.2 Adaptive Learning Based on SOSM

This work aims to track the desired diameter trajectory in the presence of uncertainties and unstructured uncertainties arising from variations in system parameters and unmodeled system dynamics, respectively. The iterative learning control is widely employed for systems with repetitive operations. The system tracking response is improved iteratively through adaptive learning of variations in plant parameters combined with second-order sliding mode control for robustness against unknown and unstructured uncertainties.

In literature, the combination of SOSM and ILC is referred to as *Learning Variable Structure Control* (LVSC), i.e., VSC and ILC are synthesized as the robust and intelligent parts, respectively (Xu and Cao 2001). This LVSC control paradigm functions in two steps: First, VSC is designed to achieve the equivalent control profile that guarantees perfect tracking and complete disturbance rejection. Secondly, the iterative learning scheme is designed to learn the equivalent control, repetitively based on tracking error signals from previous iterations. The VSC scheme can be viewed as the design of feedback control in parallel to the realization of feedforward control through ILC (Xu and Cao 2001).

The higher-order sliding mode techniques have been extensively investigated for the elimination of chattering effects encountered in traditional SMC. Furthermore, the designed control effort is continuous and more economical in restricting the system trajectory within the region of convergence. Consequently, better robustness is achieved than with the traditional scheme despite the presence of noise and disturbances affecting the system.

7.2.1 Controller design strategy

The control scheme used in this work is based on Ding and Yang (2014). Consider the n^{th}-order SISO nonlinear dynamical system with time-varying and uncertain parameters

expressed in normal form as follows:

$$\begin{aligned} \dot{x}_{j,i} &= x_{j+1,i}, \quad 1 \leq j \leq n-1 \\ \dot{x}_{n,i} &= \boldsymbol{\theta}^T(t)\,\boldsymbol{\xi}(\boldsymbol{x}_i, t) + b(t)u_i(t) + d_i(t) \\ x_i(0) &= x_0, \quad t \in [0, T] \end{aligned} \tag{7.5}$$

where i is the iteration number that denotes the i^{th} repetitive operation of the system. $\boldsymbol{x}_i = [x_{1,i}, x_{2,i}, \ldots, x_{n,i}]^T \in \mathbb{R}^n$ and $u \in \mathbb{R}$ are the state vector and system input, respectively. $\boldsymbol{\theta}(t) \in C(\mathbb{R}^p, [0, T])$ is a vector of continuously differentiable unknown time-varying parameters, representing the parametric uncertainties, $b(t) \in C^1([0, T])$ is the unknown time-varying input gain and $d_i(t)$ denotes unknown bounded disturbance. $\boldsymbol{\xi}(\boldsymbol{x}_i, t) \in \mathbb{R}^p$ is a known vector function. The target trajectory is defined as $x_d(t) = [x_{1,d}(t), x_{2,d}(t), \ldots, x_{n,d}(t)]^T = [y_d(t), \dot{y}_d(t), \ldots, y_d^{(n-1)}(t)]^T$. The output vector is defined as the error signal between desired trajectory and the actual states, i.e., $e_i(t) = x_d(t) - x_i(t)$. The error term can be expanded as:

$$\begin{aligned} e_i(t) &= [e_{1,i}(t), e_{2,i}(t), \ldots, e_{n,i}(t)]^T \\ &= [y_d(t) - x_{1,i}(t), \dot{y}_d(t) - x_{2,i}(t), \ldots, y_d^{(n-1)}(t) - x_{n,i}(t)]^T \end{aligned}$$

The objective is to design a suitable control signal $u_i(t)$ such that the desired reference can be tracked with a small error tolerance ϵ as follows:

$$|x_d(t) - x(t)| \leq \epsilon$$

The following assumptions are imposed on the system for controller design:

Assumption 1: The initial resetting condition is satisfied, i.e., $e_i(0) = \dot{e}_i(0) = \ldots, e_i^{(n)}(0) = 0, \forall i$ and $t \in [0, T]$.

Assumption 2: The unknown disturbance is bounded such that: $|b^{-1}(t)\, d_i(t)| \leq b_m \forall t \in [0, T]$, where b_m is a positive constant.

Assumption 3: The control direction of (7.5) is known, which implies that the sign of $b(t)$ is known for all $t \in [0, T]$.

7.2.2 Design of sliding manifold

The sliding surface dynamics can be expressed in terms of the error signal and its derivatives as follows:

$$\begin{aligned} \sigma_i(t) &= c_1\, e_{1,i}(t) + c_2\, e_{2,i}(t) + \ldots + c_n\, e_{n,i}(t) \\ &= \sum_{j=1}^{n} c_j\, e_{j,i}(t) = \sum_{j=1}^{n} c_j\, e_{1,i}^{(j-1)}(t) \end{aligned} \tag{7.6}$$

where the coefficient $c_n = 1$ and $c_j | j = 1, \ldots, n-1$ are the coefficients of a Hurwitz polynomial.

The derivatives of a sliding variable $\sigma_i(t)$ can be expressed as:

$$\begin{aligned}\dot{\sigma}_i(t) &= c_1\,\dot{e}_{1,i}(t) + c_2\,\dot{e}_{2,i}(t) + \ldots + \dot{e}_{n,i}(t)\\ &= c_1\,e_{2,i}(t) + c_2\,e_{3,i}(t) + \ldots + y_d^{(n)} - \dot{x}_{n,i}\\ &= \sum_{j=1}^{n-1} c_j\,e_{j+1,i}(t) + y_d^{(n)}\\ &- \boldsymbol{\theta}^T(t)\,\boldsymbol{\xi}(\boldsymbol{x}_i,t) - b(t)u_i(t) - d_i(t)\end{aligned} \tag{7.7}$$

Consider a nonnegative Lyapunov function at the i^{th} iteration as:

$$V_i(t) = \frac{\sigma_i^2(t)}{2\,b(t)} \tag{7.8}$$

The derivative of (7.8) is:

$$\begin{aligned}\dot{V}_i &= \frac{\sigma_i\dot{\sigma}_i}{b} - \frac{b^{-2}\dot{b}\sigma_i^2}{2}\\ &= \sigma_i\big[b^{-1}\sum_{j=1}^{n-1} c_j e_{j+1,i} - b^{-1}\boldsymbol{\theta}^T(t)\boldsymbol{\xi}(\boldsymbol{x}_i,t)\\ &+ b^{-1}y_d^{(n)} - u_i(t) - b^{-1}d_i(t) - \frac{1}{2}b^{-2}\dot{b}\sigma_i\big]\\ &= \sigma_i[\boldsymbol{\vartheta}^T\,\boldsymbol{\phi}_i - u_i(t) - b^{-1}d_i(t)]\end{aligned} \tag{7.9}$$

where $\boldsymbol{\vartheta} = [b^{-1}, -b^{-1}\boldsymbol{\theta}^T(t), b^{-2}\dot{b}]^T \in \mathbb{R}^{p+2}$ is the unknown time-varying system uncertainty and $\boldsymbol{\phi}_i = [y_d^{(n)} + \sum_{j=1}^{n-1} c_j\,e_{j+1,i},\ \boldsymbol{\xi}^T,\ -\frac{1}{2}\sigma_i]^T \in \mathbb{R}^{p+2}$ is the known vector function.

Finally, the adaptive ILC based second-order sliding mode at the i^{th} iteration reads as:

$$\begin{aligned}u_i(t) &= k\sigma_i + \hat{\boldsymbol{\vartheta}}_i^T(t)\boldsymbol{\phi}_i - \upsilon_i(t) + \nu|\sigma_i|^{\frac{2}{3}}\mathrm{sgn}(\sigma_i)\\ \dot{\upsilon}_i(t) &= -\beta_1\sigma_i - \beta_2|\sigma_i|^{\frac{1}{3}}\mathrm{sgn}(\sigma_i), \quad \upsilon_i(0) = 0\\ \hat{\boldsymbol{\vartheta}}_i(t) &= \hat{\boldsymbol{\vartheta}}_{i-1}(t) + q\boldsymbol{\phi}_i(\eta|\sigma_i|^{\frac{1}{3}}\mathrm{sgn}(\sigma_i) + \gamma\sigma_i), \quad \hat{\boldsymbol{\vartheta}}_{-1}(t) = 0\end{aligned} \tag{7.10}$$

where k is the feedback gain and q is the learning gain. The controller parameters ν, β_1, β_2, γ and η are positive. The integral term $\upsilon_i(t)$ is used to cancel the effect of the unknown bounded disturbance. The expressions of $u_i(t)$ and $\upsilon_i(t)$ characterize the second-order sliding mode and the expression of $\hat{\boldsymbol{\vartheta}}_i$ is the ILC law. The continuous functions $|\sigma_i|^{\frac{1}{3}}\mathrm{sgn}(\sigma_i)$ and $|\sigma_i|^{\frac{2}{3}}\mathrm{sgn}(\sigma_i)$ are used to reduce the control chattering effect.

Finally, for avid readers, the detailed convergence analysis based on composite energy functions for the adaptive ILC based second-order sliding mode control can be found in (Ding and Yang 2014). Similar analysis can also be found in (Xu and Cao 2001, Chen et al. 2012).

7.3 Transformation to Normal Form, Controller Design and Simulation Results

The Cz dynamics of the interface have the same relative degree as the system-order, i.e., n. Based on input-output linearization, the dynamics of (7.1) are transformed into the normal form by applying the change of variables. The transformation of dynamics given by (7.1) into normal form is given in (7.11). For complete details, the reader may refer to (Slotine et al. 1991, Khalil 1996).

$$\begin{aligned}\dot{\zeta}_1 &= \zeta_2 \\ \dot{\zeta}_2 &= v_g \left[\frac{u - \left(v_{cru} + C_{\alpha,z}\, v_g\right)}{C_{\alpha,n}}\right] \\ & \quad sec^2\left(\tan^{-1}\left(\frac{\zeta_2}{v_g}\right)\right)\end{aligned} \tag{7.11}$$

Table 7.1: Thermophysical properties and controller parameters for the Si crystallization process

Thermophysical properties		**Controller parameters**	
T_{env}	$1262\,\mathrm{K}$	k	0.0125
T_B	$1690\,\mathrm{K}$	c_1	0.1875
T_M	$1685\,\mathrm{K}$	ν	0.0125
ρ_s	$2329\,\mathrm{kg\,m^{-3}}$	β_1	0.0125
ρ_m	$2580\,\mathrm{kg\,m^{-3}}$	β_2	0.0125
k_s	$21.6\,\mathrm{W\,m^{-1}\,K}$	γ	$0.018\,75$
k_l	$67.0\,\mathrm{W\,m^{-1}\,K}$	q	$0.018\,75$
ΔH	$1.8 \times 10^6\,\mathrm{J\,kg^{-1}}$	η	$0.018\,75$
ϵ_c	0.6		
σ_{sb}	$5.67 \times 10^{-8}\,\mathrm{W\,m^{-2}\,K^{-4}}$		
σ_{lv}	$0.7835\,\mathrm{N\,m^{-1}}$		

7.4 Simulation Results

The designed second-order sliding mode control integrated with the ILC has been tested in simulation studies for setpoint changes both in positive and negative directions. The initial conditions for diameter ($d_c = 2r_c$)) and the growth angle α_c are chosen to be $171\,\mathrm{mm}$ and 0° respectively. The thermophysical properties and controller parameters chosen for the simulations are listed in Table 7.1. The peak (maximum) error (e_{max}) and root-mean-squared error (e_{rms}) in each run have been chosen as the performance parameters. The simulation studies also show marked improvement in the transient response with each iteration. The reference trajectory is designed in such a manner that its smoothness up to the first derivative is ensured.

With a $50\,\mathrm{mm}$ increase in the commanded crystal diameter $d_{c,ref}$, the integrated sliding mode and iterative learning control is applied for ten iterations. The top row in Fig. 7.1 shows the crystal diameter d_c response for a $50\,\mathrm{mm}$ change in the commanded crystal diameter $d_{c,ref}$. The bottom row shows the error profile for all the iterations with the blue curve representing the error in the first iteration, while the black profile represents the error in the last iteration. After 10 iterations, the peak and root-mean-square errors (cf. Fig. 7.2) have been reduced by around 86 % and 70 %, respectively as compared to the first iteration. Hence, there is a marked improvement in terms of transient response as well as the tracking performance. For the same change in commanded reference ($50\,\mathrm{mm}$), the responses for meniscus height and growth angle are shown in Fig. 7.3. Both the meniscus height h_c and the crystal growth angle α_c tend to a stable value.

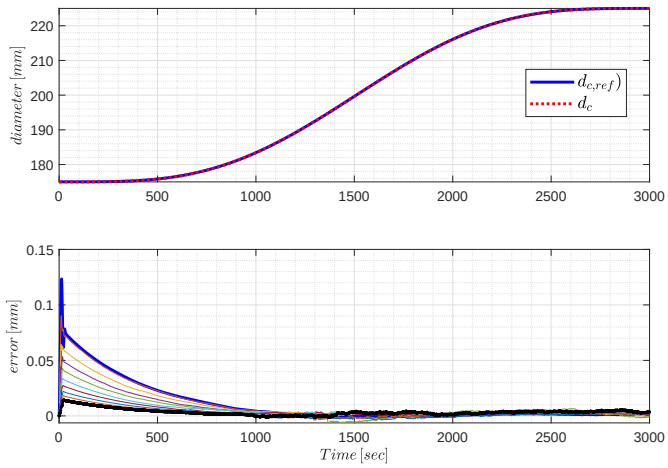

Figure 7.1: Top row: Commanded diameter increase $d_{c,ref}$ by $50\,\mathrm{mm}$ vs the actual crystal diameter trend for the last iteration. Bottom row: Error signal plotted for different iterations. First iteration result ( ), last iteration result ( ).

The results for the negative change in commanded diameter reference are the same as those for the positive change.

The results show that even with the rough tuning of controller parameters, the designed controller can track the commanded diameter quite well. Moreover, with each subsequent iteration, the tracking error reduces thereby, improving the system performance. This work may be taken up further towards its implementation in real-time because the variations in process conditions and wearing out of individual components call for the improvement in each run based on the run history. Moreover, the state estimation needs to be incorporated, such as a nonlinear observer.

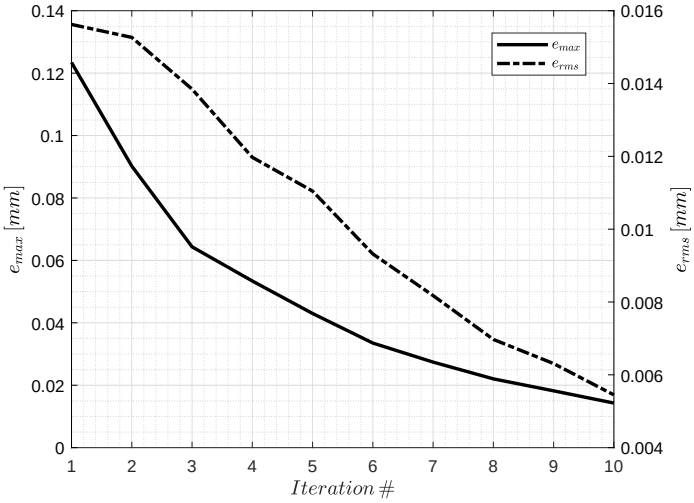

Figure 7.2: Peak and root-mean-squared error in each iteration for positive change in the commanded reference

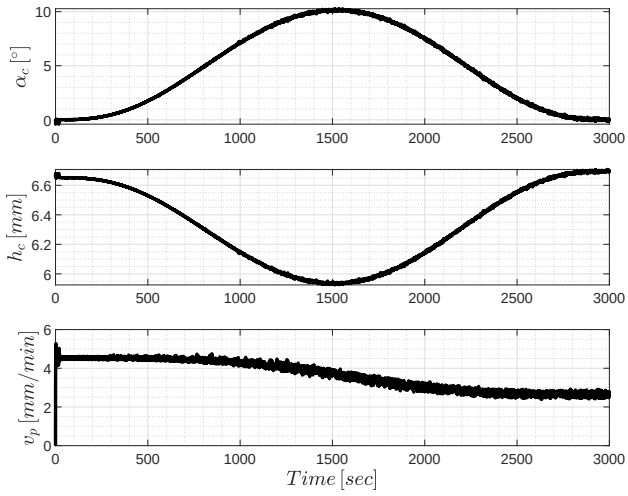

Figure 7.3: Response for +50mm reference change (10^{th} iteration)

Chapter 8

Concluding Remarks and Way Forward

This chapter concludes this dissertation with further guidelines for the practical implementation of the proposed techniques and identifies some prospective areas for future exploration.

The prime focus of this thesis is the model-based control of the Cz crystal pulling process, specifically related to the production of monocrystalline silicon ingots. The thesis is aimed at mitigating the challenges associated with the dynamics of the process itself and the related measurement dynamics.

The thesis mainly deals with the investigation of the non-minimum phase behaviour of the bright ring measurement signal and the strategies to account for this behaviour via model-based control design. The flow of this thesis is streamlined into two core parts, with the first part focusing on the development of the simulation model, via a 3-D ray-tracing method. This model traces the incoming and outgoing rays to simulate the dynamics of the bright ring image. Moreover, the 3D simulation aids in determining that point on the camera image, whose lateral distance from the crystal central axis gives the measurement of the crystal radius. This point should be close to the crystal surface and be identifiable with both consistency and ease on the camera image. It was found that the point of reflection on the meniscus, originating from the outermost edge of the heat-shield, fulfills these criteria simultaneously. Furthermore, the presence of anomalous behaviour in the measurement signal is not only verified but in addition, its dynamics have been quantified, thereby also quantifying the bandwidth limitation imposed by the RHP zero. This information is crucial for determining suitable control to ensure effective crystal radius control.

The second part focuses on developing and testing a control strategy to deal with the undesired behaviour in the measurement signal. First, the nonlinear model presented in the first part is linearized to obtain linear models for control design purpose. These simplified models capture the non-minimum phase characteristics of the plant which do not differ

quite much depending on the mode of heat transfer from melt to the interface. The proposed control strategy involves compensation for the inverse behaviour with the use of a parallel compensator and a conventional PID controller for stabilization and disturbance rejection. This signifies that the controller-related design issues, that were previously limiting the system's achievable bandwidth, have been circumvented successfully. Finally, the performance of the closed-loop system is assessed using nonlinear simulations including temperature disturbances that alter the crystal growth rate. The results show that the designed controller stabilizes the crystal radius and has satisfactory disturbance rejection capability for the disturbances that typically occur in the Cz process. It should be noted that the approach taken is valid because the inverse response is present only in the *bright ring measurement* of the crystal radius, not in the crystal radius itself.

The existence of the measurement anomaly/right-half-plane zero is mainly dependent on the hydrodynamic effects governing the meniscus shape. This part of the model is based on established literature and is based on solid theory, and the *existence* of the measurement anomaly has also been reported previously. There is therefore no reason to question the existence of the measurement anomaly, nor the *conceptual* validity of the design of the parallel compensator to remove the corresponding limitation to feedback control performance. The exact *location* of the RHP zero may be affected by heat transfer around the liquid/solid interface. The strong effect of the crystal radius on the meniscus shape would also lead one to expect that the location of the RHP zero will depend on the crystal radius. Different plants produce crystals of different radii. For actual industrial implementation, it will therefore be prudent to verify the model w.r.t. the location of the RHP zero, using plant measurements.

In contrast, the temperature dynamics are rather qualitative and represent a compromise between accuracy and simplicity. In this work, it is used primarily to provide a (somewhat) realistic illustration of how temperature disturbances will affect the proposed radius control. High accuracy is therefore not critical. The heater temperature control is a relatively simple control loop, due to the position of the measurement close to the manipulated variable (heater power). However, the propagation of heat from the heaters to the melt and the melt/crystal interface is significantly more uncertain. The use of the thermal part of the model in this work to design temperature feedforward trajectories for run-to-run control would therefore require quite an extensive model validation from the actual plant.

Finally, Chap. 7 reports on an early approach focussing on combining learning from the repetitive nature of the process with control. Although interesting results are obtained, this approach requires further study, as discussed in the next section.

8.1 Way Forward

The present work has proposed certain ways to investigate and mitigate the non-minimum phase behaviour of the Cz process. The future tasks that can help to enhance the potential and effectiveness of this work may broadly be categorized as follows:

I.) To implement the proposed control strategy in the Cz industry, a prudent approach would be to perform the following analysis:

i.) Develop models at several crystal lengths along the body phase and validate these models against actual plant/ingot measurements. The validated models should subsequently be used to check the performance and robustness of control combining parallel compensation and feedback control.

ii.) If such an analysis shows that a single controller and a single parallel compensator do not provide acceptable performance throughout the entire body stage, then modify the control design with pertinent modifications such as *gain-scheduling*. The slow crystal growth means that the gain scheduling approach to changing the controller can be applied. Clearly, the final design will also need to be subject to validation experiments.

II.) An interesting approach that may be explored to deal with the presence of RHP zeros in crystal radius measurement is to set up two measurement systems (i.e., based on *differential weight* (Satunkin and Leonov 1990) and *bright ring* estimates) simultaneously. This yields a non-square (2×1) system matrix with single input $\begin{bmatrix} v_p \end{bmatrix}$ and two outputs $\begin{bmatrix} r_{br} & \dot{W}_c \end{bmatrix}$. Although the presence of RHP zeros for each measurement is related to the meniscus dynamics, it is not obvious that these two zeros are in the same location of the complex plane. If the RHP zeros have different locations in the RHP, it is possible that the (2×1) system has no RHP zero (Skogestad and Postlethwaite 2007), and hence that a (1×2) feedback controller can be designed for which there would be no limitation on the achievable bandwidth. This warrants further study.

III.) Investigating the effects of crucible and crystal rotation, (imparting centrifugal effect) on the meniscus shape, can also be considered as a potential research challenge in future work.

IV.) Since Cz is a batch process that repeats itself every time a new crystal ingot is produced, it may have the potential to make use of iterative learning control technique to cater for unknown disturbances and uncertain parameters. Chap. 7 reports on an early attempt in this direction. A clear shortcoming of the approach is that it assumes the crystal radius to be measured directly. In light of the insight gained later in this Ph.D. project, reported in chapters 4, 5 & 6, it is clear that further study would be required on the use of the ILC-SOSM approach with the bright ring radius measurement.

Bibliography

Abdelkader, M., Al-Salaymeh, A., Al-Hamamre, Z., Sharaf, F., 2010. A Comparative Analysis of the Performance of Monocrystalline and Multiycrystalline PV Cells in Semi Arid Climate Conditions: the Case of Jordan. Jordan Journal of Mechanical & Industrial Engineering 4.

Abdollahi, J., Izadi, M., Dubljevic, S., 2014. Model predictive temperature tracking in crystal growth processes. Computers & Chemical Engineering 71, 323–330.

Anttila, O., 2015. Chapter 2 - Czochralski growth of silicon crystals, in: Handbook of Silicon Based MEMS Materials and Technologies (Second Edition). William Andrew Publishing, Boston. Micro and Nano Technologies, pp. 18–55.

Atherton, L., Derby, J., Brown, R., 1987. Radiative heat exchange in Czochralski crystal growth. Journal of Crystal Growth 84, 57–78.

Bandoh, K., Okumura, T., Morimoto, S., Nagata, T., Yokota, S., 2008. Sliding-Mode Control with Nonlinear State Predictor for Nonlinear Processes with Large Time Delay and Its application. Transactions of the Japan Society of Mechanical Engineers Series C 74, 2001–2008.

Bardsley, W., Cockayne, B., Green, G., Hurle, D., Joyce, G., Roslington, J., Tufton, P., Webber, H., Healey, M., 1974a. Developments in the weighing method of automatic crystal pulling. Journal of Crystal Growth 24, 369–373.

Bardsley, W., Frank, F., Green, G., Hurle, D., 1974b. The meniscus in Czochralski growth. Journal of Crystal Growth 23, 341–344.

Bardsley, W., Green, G., Holliday, C., Hurle, D., 1972. Automatic control of Czochralski crystal growth. Journal of Crystal Growth 16, 277–279.

Bardsley, W., Hurle, D., Joyce, G., 1977a. The weighing method of automatic Czochralski crystal growth: I. basic theory. Journal of Crystal Growth 40, 13–20.

Bardsley, W., Hurle, D., Joyce, G., Wilson, G., 1977b. The weighing method of automatic Czochralski crystal growth: II. control equipment. Journal of Crystal Growth 40, 21–28.

Bliss, D.F., 2010. 7 - Indium Phosphide: Crystal Growth and Defect Control by Applying Steady Magnetic Fields, in: Springer Handbook of Crystal Growth. Springer, pp. 205–229.

Van den Bogaert, N., Dupret, F., 1997. Dynamic global simulation of the Czochralski process I. Principles of the method. Journal of Crystal Growth 171, 65–76.

Bornside, D.E., Kinney, T.A., Brown, R.A., Kim, G., 1990. Finite element/Newton method for the analysis of Czochralski crystal growth with diffuse-grey radiative heat transfer. International Journal for Numerical Methods in Engineering 30, 133–154.

Boucher, E.A., Jones, T.G.J., 1980. Capillary phenomena. part II.-Approximate treatment of the shape and properties of fluid interfaces of infinite extent meeting solids in a gravitational field. J. Chem. Soc., Faraday Trans. 1 76, 1419–1432.

Braescu, L., Epure, S., Duffar, T., 2010. Chapter 8 - Mathematical and Numerical Analysis of Capillarity Problems and Processes, in: Crystal Growth Processes Based on Capillarity: Czochralski, Floating Zone, Shaping and Crucible Techniques. John Wiley & Sons, Ltd Chichester, UK, pp. 465–524.

Braga, A., Moreira, S., Zampieri, P., Bacchin, J., Mei, P., 2008. New processes for the production of solar-grade polycrystalline silicon: A review. Solar Energy Materials and Solar Cells 92, 418–424.

Brice, J., 1973. The Growth of Crystals from Liquids. North-Holland/American Elsevier, Amsterdam/New York.

Bukhari, H.Z., Aftab, M.F., Winkler, J., Hovd, M., 2017. Adaptive Nonlinear Control of the Czochralski Process via Integration of Second Order Sliding Mode and Iterative Learning Control, in: 2017 11th Asian Control Conference (ASCC), IEEE. pp. 2732–2737.

Bukhari, H.Z., Hovd, M., Aftab, M.F., Winkler, J., 2020. Design of parallel compensator and stabilizing controller to mitigate non-minimum phase behaviour of the Czochralski Process. IFAC-PapersOnLine 53, 11710–11715.

Bukhari, H.Z., Hovd, M., Winkler, J., 2019. Limitations on control performance in the Czochralski crystal growth process using bright ring measurement as a controlled variable. IFAC-PapersOnLine 52, 129–134.

Bukhari, H.Z., Hovd, M., Winkler, J., 2021a. Inverse response behaviour in the bright ring radius measurement of the Czochralski process I: Investigation. Journal of Crystal Growth 568, 126039.

Bukhari, H.Z., Hovd, M., Winkler, J., 2021b. Inverse response behaviour in the bright ring radius measurement of the Czochralski process II: Mitigation by control. Journal of Crystal Growth 568, 126013.

Bukowski, A., 2013. Czochralski-grown silicon crystals for microelectronics. Acta Physica Polonica, A. 124.

Carter, C.B., Norton, M.G., 2007. Growing Single Crystals. Springer, New York, NY. pp. 507–526.

Chen, W., Chen, Y.Q., Yeh, C.P., 2012. Robust iterative learning control via continuous sliding-mode technique with validation on an SRV02 rotary plant. Mechatronics 22, 588–593.

Chunduri, S.K., Schmela, M., 2019. Surprising developments leading to significantly higher power ratings of solar modules. URL: http://taiyangnews.info/reports/advanced-module-technologies-2019/.

Cowern, N., 2012. 1 - Silicon-based photovoltaic solar cells, in: Kilner, J.A., Skinner, S.J., Irvine, S.J., Edwards, P.P. (Eds.), Functional Materials for Sustainable Energy Applications. Woodhead Publishing. Woodhead Publishing Series in Energy, pp. 3–22.

Dabkowska, H.A., Dabkowski, A.B., 2010. 12 - Crystal Growth of Oxides by Optical Floating Zone Technique, in: Springer Handbook of Crystal Growth. Springer, pp. 367–391.

Dash, W.C., 1958. Silicon Crystals Free of Dislocations. Journal of Applied Physics 29, 736–737.

Dash, W.C., 1959. Growth of Silicon Crystals Free from Dislocations. Journal of Applied Physics 30, 459–474.

Delannoy, Y., 2012. Purification of silicon for photovoltaic applications. Journal of Crystal Growth 360, 61–67. 5th International Workshop on Crystal Growth Technology.

Derby, J., Brown, R., 1986a. Thermal-capillary analysis of Czochralski and liquid encapsulated Czochralski crystal growth: I. Simulation. Journal of Crystal Growth 74, 605–624.

Derby, J., Brown, R., 1986b. Thermal-capillary analysis of Czochralski and liquid encapsulated Czochralski crystal growth: II. Processing strategies. Journal of Crystal Growth 75, 227–240.

Derby, J., Brown, R., 1987. On the dynamics of Czochralski crystal growth. Journal of Crystal Growth 83, 137–151.

Derby, J., Brown, R., Geyling, F., Jordan, A., Nikolakopoulou, G., 1985. Finite Element Analysis of a Thermal-Capillary Model for Liquid Encapsulated Czochralski growth. Journal of the Electrochemical Society 132, 470–482.

Dessauer, R.G., Patzner, E.J., Poponiak, M.R., 1970. Radiation sensitive control system for crystal growing apparatus. US Patent 3,493,770.

Dhanaraj, G., Byrappa, K., Prasad, V., Dudley, M., 2010a. Springer Handbook of Crystal Growth. Springer Science & Business Media.

Dhanaraj, G., Byrappa, K., Prasad, V.V., Dudley, M., 2010b. 1 - Crystal Growth Techniques and Characterization: An Overview, in: Springer Handbook of Crystal Growth. Springer, pp. 3–16.

Digges, T., Hopkins, R., Seidensticker, R., 1975. The basis of automatic diameter control utilizing "bright ring" meniscus reflections. Journal of Crystal Growth 29, 326–328.

Ding, J., Yang, H., 2014. Adaptive iterative learning control for a class of uncertain nonlinear systems with second-order sliding mode technique. Circuits, Systems, and Signal Processing 33, 1783–1797.

Dold, P., 2015. Chapter One - Silicon Crystallization Technologies, in: Advances in Photovoltaics: Part 4. Elsevier. volume 92 of *Semiconductors and Semimetals*, pp. 1–61.

Domey, K., 1971. Computer Controlled Growth of Single Crystal Ingots. Solid State Technology 14, 41–45.

Dornberger, E., Tomzig, E., Seidl, A., Schmitt, S., Leister, H.J., Schmitt, C., Müller, G., 1997. Thermal simulation of the Czochralski silicon growth process by three different models and comparison with experimental results. Journal of Crystal Growth 180, 461–467. Modelling in Crystal Growth.

Dreyer, W., Druet, P.É., Klein, O., Sprekels, J., 2012. Mathematical modeling of Czochralski type growth processes for semiconductor bulk single crystals. Milan Journal of Mathematics 80, 311–332.

Duanmu, N., 2006. Modeling, Dynamics and Control of the Czochralski Crystal Growth Processes. Ph.D. thesis. Boston University.

Duffar, T., 2010. Crystal Growth Processes Based on Capillarity: Czochralski, Floating Zone, Shaping and Crucible Techniques. John Wiley & Sons.

Duffar, T., Sylla, L., 2010. Chapter 6 - Vertical Bridgman Technique and Dewetting, in: Crystal Growth Processes Based on Capillarity: Czochralski, Floating Zone, Shaping and Crucible Techniques. John Wiley & Sons, Ltd, pp. 355–411.

Dupret, F., Van den Bogaert, N., 1994. Modelling Bridgman and Czochralski growth. Handbook of Crystal Growth 2, 875–1010.

Dupret, F., Nicodème, P., Ryckmans, Y., Wouters, P., Crochet, M., 1990. Global modelling of heat transfer in crystal growth furnaces. International Journal of Heat and Mass Transfer 33, 1849–1871.

Dupret, F., Ryckmans, Y., Wouters, P., Crochet, M., 1986. Numerical calculation of the global heat transfer in a Czochralski furnace. Journal of Crystal Growth 79, 84–91.

Dutta, P.S., 2010. 10 - Bulk Crystal Growth of Ternary III–V Semiconductors, in: Springer Handbook of Crystal Growth. Springer, pp. 281–325.

Europen Union, 2020. 2050-Long-term strategy. https://ec.europa.eu/clima/policies/strategies/2050_en/.

eurostate newsrelease, 17/2020 - 23 January 2020, 2020. Renewable energy in the EU in 2018. https://ec.europa.eu/eurostat/documents/2995521/10335438/8-23012020-AP-EN.pdf.

Falster, R., Voronkov, V., 2000. Intrinsic point defects and their control in silicon crystal growth and wafer processing. MRS bulletin 25, 28–32.

Fornari, R. (Ed.), 2018. Single Crystals of Electronic Materials: Growth and Properties. 1 ed., Woodhead Publishing.

Friedrich, J., 2016. Methods for Bulk Growth of Inorganic Crystals: Crystal Growth, in: Reference Module in Materials Science and Materials Engineering. Elsevier.

Friedrich, J., von Ammon, W., Müller, G., 2015. Chapter 2 - Czochralski growth of silicon crystals, in: Rudolph, P. (Ed.), Handbook of Crystal Growth (Second Edition). Elsevier, Boston. Handbook of Crystal Growth, pp. 45–104.

Garcia, C.E., Morari, M., 1982. Internal model control. A unifying review and some new results. Industrial & Engineering Chemistry Process Design and Development 21, 308–323.

Gevelber, M., Wilson, D., Duanmu, N., 2001. Modelling requirements for development of an advanced Czochralski control system. Journal of Crystal growth 230, 217–223.

Gevelber, M.A., 1994a. Dynamics and control of the Czochralski process III. interface dynamics and control requirements. Journal of Crystal Growth 139, 271–285.

Gevelber, M.A., 1994b. Dynamics and control of the Czochralski process IV. control structure design for interface shape control and performance evaluation. Journal of Crystal Growth 139, 286–301.

Gevelber, M.A., Stephanopoulos, G., 1987. Dynamics and control of the Czochralski process: I. modelling and dynamic characterization. Journal of Crystal Growth 84, 647–668.

Gevelber, M.A., Stephanopoulos, G., Wargo, M.J., 1988. Dynamics and control of the Czochralski process II. Objectives and control structure design. Journal of Crystal Growth 91, 199–217.

Gevelber, M.A., Wargo, M.J., Stephanopoulos, G., 1987. Advanced control design considerations for the Czochralski process. Journal of Crystal Growth 85, 256–263.

Gribov, B., Zinov'ev, K., 2003. Preparation of high-purity silicon for solar cells. Inorganic materials 39, 653–662.

Gross, U., Kersten, R., 1972. Automatic crystal pulling with optical diameter control using a laser beam. Journal of Crystal Growth 15, 85–88.

Hosseinpour, A., Tafaghodi Khajavi, L., 2018. Slag refining of silicon and silicon alloys: a review. Mineral Processing and Extractive Metallurgy Review 39, 308–318.

Huang, X., Taishi, T., Wang, T., Hoshikawa, K., 2001. Measurement of temperature gradient in Czochralski silicon crystal growth. Journal of Crystal Growth 229, 6–10. 1st Asian Conf. on Crystal Growth and Crystal Technology.

Huh, C., Scriven, L., 1969. Shapes of axisymmetric fluid interfaces of unbounded extent. Journal of Colloid and Interface Science 30, 323–337.

Hurle, D., 1977. Control of diameter in Czochralski and related crystal growth techniques. Journal of Crystal Growth 42, 473–482.

Hurle, D., 1983. Analytical representation of the shape of the meniscus in Czochralski growth. Journal of Crystal Growth 63, 13–17.

Hurle, D., Joyce, G., Ghassempoory, M., Crowley, A., Stern, E., 1990. The Dynamics of Czochralski Growth. Journal of Crystal Growth 100, 11–25.

Hurle, D., Joyce, G., Wilson, G., Ghassempoory, M., Morgan, C., 1986. A technique for experimentally determining the transfer function of a Czochralski pulling process. Journal of Crystal Growth 74, 480–490.

Hurle, D., Rudolph, P., 2004. A brief history of defect formation, segregation, faceting, and twinning in melt-grown semiconductors. Journal of Crystal Growth 264, 550–564. Proceedings of the Symposium - Progress in Crystal Growth.

Irizarry-Rivera, R., Seider, W.D., 1997a. Model-predictive control of the Czochralski crystallization process. part I. conduction-dominated melt. Journal of Crystal Growth 178, 593–611.

Irizarry-Rivera, R., Seider, W.D., 1997b. Model-predictive control of the Czochralski crystallization process. part II. reduced-order convection model. Journal of Crystal Growth 178, 612–633.

Itaka, K., Ogasawara, T., Boucetta, A., Benioub, R., Sumiya, M., Hashimoto, T., Koinuma, H., Furuya, Y., 2015. Direct carbothermic silica reduction from purified silica to solar-grade silicon, in: Journal of Physics: Conference Series, IOP Publishing.

Javidi, M., 2003. Controlled crown growth process for Czochralski single crystal silicon. US Patent App. 10/215,113.

Johansen, T.H., 1992. The weight gain signal in Czochralski crystal growth. Journal of Crystal Growth 118, 353–359.

Johansen, T.H., 1994. An improved analytical expression for the meniscus height in Czochralski growth. Journal of Crystal Growth 141, 484–486.

Jurisch, M., Eichler, S., Bruder, M., 2015. 9 - Vertical Bridgman Growth of Binary Compound Semiconductors, in: Rudolph, P. (Ed.), Handbook of Crystal Growth. second edition ed.. Elsevier, Boston, pp. 331–372.

Kearns, J.K., 2019. 2 - Silicon Single Crystals, in: Fornari, R. (Ed.), Single Crystals of Electronic Materials. Woodhead Publishing. Woodhead Publishing Series in Electronic and Optical Materials, pp. 5–56.

Khalil, H.K., 1996. Nonlinear Systems. Prentice-Hall, New Jersey.

Kimbel, S.L., O'Sullivan, J.A., 2001. Shape estimation for online diameter calibration in Czochralski silicon crystal growth, in: Process Imaging for Automatic Control, International Society for Optics and Photonics. pp. 45–57.

Klapper, H., Rudolph, P., 2015. Defect generation and interaction during crystal growth, in: Handbook of Crystal Growth. Elsevier, pp. 1093–1141.

Komperød, M., Bones, J.A., Lie, B., 2011. A Sensor Fusion Algorithm for Filtering Pyrometer Measurement Noise in the Czochralski Crystallization Process. Modeling, Identification and Control 32, 17.

Krause, M., Friedrich, J., Müller, G., 2002. Systematic study of the influence of the Czochralski hot zone design on the point defect distribution with respect to a "perfect" crystal. Materials Science in Semiconductor Processing 5, 361–367.

Kuroda, E., 1983. Temperature oscillation at the growth interface in silicon crystals. Journal of Crystal Growth 61, 173–176.

Kuroda, E., Kozuka, H., 1983. Influence of growth conditions on melt interface temperature oscillations in silicon Czochralski growth. Journal of Crystal Growth 63, 276–284.

Kuroda, E., Kozuka, H., Takano, Y., 1984. The effect of temperature oscillations at the growth interface on crystal perfection. Journal of Crystal Growth 68, 613–623.

Lan, C.W., 2010. 36 - Convection and Control in Melt Growth of Bulk Crystals, in: Springer Handbook of Crystal Growth. Springer, pp. 1215–1242.

Lane, R., 1981. Development of advanced Czochralski growth process to produce low cost 150 kg silicon ingots from a single crucible for technology readiness. Quarterly Progress Report .

Lüdge, A., Riemann, H., Wünscher, M., Behr, G., Löser, W., Muiznieks, A., Cröll, A., 2010. Chapter 4 - Floating Zone Crystal Growth, in: Crystal Growth Processes Based on Capillarity: Czochralski, Floating Zone, Shaping and Crucible Techniques. John Wiley & Sons, Ltd, pp. 203–275.

Lee, K., Lee, D., Park, J., Lee, M., 2005. MPC based feedforward trajectory for pulling speed tracking control in the commercial Czochralski crystallization process. International Journal of Control, Automation, and Systems 3, 252–257.

Levinson, J., 1959. Temperature control for crystal pulling. US Patent 2,908,004.

Liu, D., Zhang, N., Jiang, L., Zhao, X., Duan, W., 2020. Nonlinear Generalized Predictive Control of the Crystal Diameter in Cz-Si Crystal Growth Process Based on Stacked Sparse Autoencoder. IEEE Transactions on Control Systems Technology 28, 1132–1139.

Lorenzini, R., Nuff, F., Blair, D., 1974. An overview of silicon crystal growth processes. Solid State Technology 2, 33.

Maurits, J., 2014. Chapter 2.6 - silicon production, in: Seetharaman, S. (Ed.), Treatise on Process Metallurgy. Elsevier, Boston, pp. 919–948.

Mika, K., Uelhoff, W., 1975. Shape and stability of menisci in Czochralski growth and comparison with analytical approximations. Journal of Crystal Growth 30, 9–20.

Müller, A., Ghosh, M., Sonnenschein, R., Woditsch, P., 2006. Silicon for photovoltaic applications. Materials Science and Engineering: B 134, 257–262. EMRS 2006, Symposium V; Advanced Silicon for the 21st Century.

Müller, G., Rudolph, P., 2001. Crystal Growth from the Melt, in: Buschow, K.J., Cahn, R.W., Flemings, M.C., Ilschner, B., Kramer, E.J., Mahajan, S., Veyssière, P. (Eds.), Encyclopedia of Materials: Science and Technology. Elsevier, Oxford, pp. 1866–1872.

Muiznieks, A., Virbulis, J., Lüdge, A., Riemann, H., Werner, N., 2015. 7 - Floating Zone Growth of Silicon, in: Rudolph, P. (Ed.), Handbook of Crystal Growth. second ed.. Elsevier, Boston, pp. 241–279.

Narayanan, M., Ciszek, T., 2010. 51 - Silicon Solar Cells: Materials, Devices, and Manufacturing, in: Springer Handbook of Crystal Growth. Springer, pp. 1701–1718.

Neubert, M., Winkler, J., 2012. Nonlinear model-based control of the Czochralski process III: Proper choice of manipulated variables and controller parameter scheduling. Journal of Crystal Growth 360, 3–11.

Neubert, M., Winkler, J., 2014. Nonlinear model-based control of the Czochralski process IV: Feedforward control and its interpretation from the crystal growerś view. Journal of Crystal Growth 404, 210–222.

Newman, R., 1982. Defects in silicon. Reports on Progress in Physics 45, 1163.

Ng, J., Dubljevic, S., Aksikas, I., 2011. Model predictive control of Czochralski crystal growth process, in: Control & Automation (MED), 2011 19th Mediterranean Conference on, IEEE. pp. 825–831.

Noghabi, O.A., M'Hamdi, M., Jomâa, M., 2011. Effect of crystal and crucible rotations on the interface shape of Czochralski grown silicon single crystals. Journal of Cystal Growth 318, 173–177.

Park, J.S., Seo, M., Oh, H.J., Jung, J.H., 2008. Silicon ingot diameter modeling in Czochralski process and its dynamic simulation. Korean Journal of Chemical Engineering 25, 623–630.

Patzner, E., Dessauer, R., Poponiak, M., 1967. Automatic diameter control of Czochralski crystals. Semiconductor Products and Solid State Technology 10, 25.

Phuc, L.T.H., Jeon, H., Truong, N.T.N., Hak, J.J., et al., 2019. Improving the dipping step in Czochraski process using Haar-Cascade algorithm. Electronics 8, 646.

Princen, H., Mason, S., 1965a. Shape of a fluid drop at a fluid-liquid interface. I. Extension and test of two-phase theory. Journal of Colloid Science 20, 156–172.

Princen, H., Mason, S., 1965b. Shape of a fluid drop at a fluid-liquid interface. II. Theory for three-phase systems. Journal of Colloid Science 20, 246–266.

Rahmanpour, P., 2017. Model-based Control of the Czochralski Silicon Crystal Pulling Process. Ph.D. thesis. Department of Engineering Cybernetics, NTNU.

Rahmanpour, P., Hovd, M., 2012. Numerical Backstepping for Diameter Control of Silicon Ingots in the Czochralski Process, in: Decision and Control (CDC), 2012 IEEE 51st Annual Conference on, IEEE. pp. 7013–7017.

Rahmanpour, P., Sælid, S., Hovd, M., 2017. Run-To-Run Control of the Czochralski Process. Computers & Chemical Engineering 104, 353–365.

Raufeisen, A., Breuer, M., Botsch, T., Delgado, A., 2009. Transient 3D simulation of Czochralski crystal growth considering diameter variations. Journal of Crystal Growth 311, 695–697.

Raufeisen, A., Breuer, M., Botsch, T., Delgado, A., 2010. Prediction of the three-phase boundary movement in Czochralski crystal growth. Journal of Crystal Growth 312, 2297–2299.

Raufeisen, A., Breuer, M., Botsch, T., Delgado, A., 2011. Time-Dependent Three-Dimensional Simulation of the Turbulent Flow and Heat Transfer in Czochralski Crystal Growth Including the Three-Phase Boundary Movement, in: High Performance Computing in Science and Engineering'10. Springer, pp. 353–367.

Rea, S.N., 1979. LSA large area silicon sheet task continuous Czochralski process development. Final report. Technical Report. Texas Instruments, Inc., Dallas (USA).

Rein, S., 2006. Lifetime spectroscopy: A method of defect characterization in silicon for photovoltaic applications. volume 85. Springer Science & Business Media.

Rummel, T., 1966. Apparatus for pulling rod-shaped crystals of semiconductor material from a melt in a crucible. US Patent 3,259,467.

Sabanskis, A., Bergfelds, K., Muiznieks, A., Schröck, T., Krauze, A., 2013. Crystal shape 2D modeling for transient CZ silicon crystal growth. Journal of Crystal Growth 377, 9–16.

Safarian, J., Tangstad, M., 2012. Vacuum Refining of Molten Silicon. Metallurgical and Materials Transactions B 43, 1427–1445.

Safarian, J., Tranell, G., Tangstad, M., 2012. Processes for Upgrading Metallurgical Grade Silicon to Solar Grade Silicon. Energy Procedia 20, 88–97.

Safarian, J., Tranell, G., Tangstad, M., 2013. Thermodynamic and Kinetic Behavior of B and Na Through the Contact of B-Doped Silicon with $Na_2O - SiO_2$ Slags. Metallurgical and Materials Transactions B 44, 571–583.

Satunkin, G., 1995. Mathematical modelling and control system design of Czochralski and Liquid Encapsulated Czochralski processes: the basic low order mathematical model. Journal of Crystal Growth 154, 172–188.

Satunkin, G., 2010. Modelling the dynamics and control design for Czochralski, liquid encapsulated Czochralski and Floating Zone processes. Progress in Crystal Growth and Characterization of Materials 56, 1–121.

Satunkin, G., Leonov, A., 1990. Weighing control of the automatic crystallization process from the melt. Journal of Crystal Growth 102, 592–608.

Schroder, D.K., 2015. Semiconductor Material and Device Characterization. John Wiley & Sons.

Seborg, D.E., Mellichamp, D.A., Edgar, T.F., Doyle III, F.J., 2010. Process Dynamics and Control. John Wiley & Sons.

Shimura, F., 2017. 13 - Single-Crystal Silicon: Growth and Properties, in: Springer Handbook of Electronic and Photonic Materials. Springer, pp. 255–269.

Sinno, T., Dornberger, E., Von Ammon, W., Brown, R., Dupret, F., 2000. Defect engineering of Czochralski single-crystal silicon. Materials Science and Engineering: R: Reports 28, 149–198.

Skogestad, S., Postlethwaite, I., 2007. Multivariable Feedback Control: Analysis and Design. volume 2. John Wiley & Sons, New York.

Slotine, J.J.E., Li, W., et al., 1991. Applied Nonlinear Control. volume 199. Prentice-Hall Englewood Cliffs, NJ.

SolarPower Europe, 2019. EU Market Outlook for Solar Power 2019-2023. https://www.solarpowereurope.org/.

Srinivasan, B., Bonvin, D., 2007. Controllability and stability of repetitive batch processes. Journal of Process Control 17, 285–295.

Srinivasan, B., Bonvin, D., Visser, E., Palanki, S., 2003. Dynamic optimization of batch processes: II. Role of measurements in handling uncertainty. Computers & Chemical Engineering 27, 27–44.

Steel, G., Hill, M., 1975. Analysis of the transfer function governing crystal growth in the Czochralski process. Journal of Crystal Growth 30, 45–53.

Su, W., Zuo, R., Mazaev, K., Kalaev, V., 2010. Optimization of crystal growth by changes of flow guide, radiation shield and sidewall insulation in Cz Si furnace. Journal of Crystal Growth 312, 495–501.

Tatarchenko, V., 1993. Shaped Crystal Growth. volume 20. Springer Science & Business Media.

Tatartchenko, V., 2010. Chapter 2 - The Possibility of Shape Stability in Capillary Crystal Growth and Practical Realization of Shaped Crystals, in: Crystal Growth Processes Based on Capillarity: Czochralski, Floating Zone, Shaping and Crucible Techniques. John Wiley & Sons, Ltd, pp. 51–114.

Tsivinskii, S., 1962. Application of the theory of capillary phenomena to obtain pieces of a desired shape from the flux by Stepanov's method. Inzh. Fiz. Zh. Akad. Nauk. Bellorussk 5.

United Nations, 2018. Sustainable Development Goals. https://www.un.org/sustainabledevelopment/sustainable-development-goals/.

USGS, 2020. Mineral Commodities Summaries. Technical Report. USGS.

Von Ammon, W., Dornberger, E., Hansson, P., 1999. Bulk properties of very large diameter silicon single crystals. Journal of Crystal Growth 198, 390–398.

Voronkov, V., 1982. The mechanism of swirl defects formation in silicon. Journal of Crystal Growth 59, 625–643.

Voronkov, V., 2008. Grown-in defects in silicon produced by agglomeration of vacancies and self-interstitials. Journal of Crystal Growth 310, 1307–1314.

Wang, J.H., Yoo, H.D., et al., 1999. Two-dimensional analysis of axial segregation in batchwise and continuous Czochralski process. Journal of Crystal Growth 198, 120–124.

Wei, Y., Li, H., Li, X., 2015. Online Trimming of Feed Forward Trajectory by System Identification and Model Predictive Control, in: Intelligent Human-Machine Systems and Cybernetics (IHMSC), 2015 7th International Conference on, IEEE. pp. 105–108.

Winkler, J., Neubert, M., 2015. Automation of crystal growth from melt, in: Hurle, D.T.J. (Ed.), Handbook of Crystal Growth (Second Edition). Elsevier. chapter 28, pp. 1143–1184.

Winkler, J., Neubert, M., Rudolph, J., 2010a. Nonlinear model-based control of the Czochralski process I: Motivation, modeling and feedback controller design. Journal of Crystal Growth 312, 1005–1018.

Winkler, J., Neubert, M., Rudolph, J., 2010b. Nonlinear model-based control of the Czochralski process II: Reconstruction of crystal radius and growth rate from the weighing signal. Journal of Crystal Growth 312, 1019–1028.

Winkler, J., Neubert, M., Rudolph, J., 2013. A review of the automation of the Czochralski crystal growth process. Acta Physica Polonica A 124, 181–192.

Winkler, J., Neubert, M., Rudolph, J., Duanmu, N., Gevelber, M., 2010c. Chapter 3 - Czochralski Process Dynamics and Control Design, in: Crystal Growth Processes Based on Capillarity: Czochralski, Floating Zone, Shaping and Crucible Techniques. John Wiley & Sons, Ltd, pp. 115–202.

Xu, J.X., Cao, W.J., 2001. Learning variable structure control approaches for repeatable tracking control tasks. Automatica 37, 997–1006.

Zhang, J., YaNi, P., Ding, L., 2019. Numerical Simulation of Thermal Field in Czochralski Monocrystalline Silicon Shoulder, in: 2019 12th Asian Control Conference (ASCC), IEEE. pp. 838–843.

Zharikov, E.V., 2012. Problems and recent advances in melt crystal growth technology. Journal of Crystal Growth 360, 146–154.

Zhou, K., Doyle, J.C., Glover, K., 1996. Robust and Optimal Control. volume 40. Prentice-Hall, Upper Saddle River, NJ, USA.

Zulehner, W., Huber, D., 1982. Czochralski-grown silicon, in: Silicon Chemical Etching. Springer, pp. 1–143.